Study of Hyperpolarised ^{3}He MRI Diffusion on Asthma and Cystic Fibrosis, and Development of Hyperpolarised ^{129}Xe MRI Lung Imaging

By

Steven M. Hardy, MPhys (Hons)

Thesis submitted to The University of Nottingham for the degree of Doctor of Philosophy

June 2016

Abstract

Hyperpolarised gas Magnetic Resonance Imaging (MRI) is a non-invasive method developed to provide images of the void spaces of the lungs, and evaluate the distal airways via diffusion weighted techniques. The work in this thesis covers the use of both hyperpolarised ^{3}He and hyperpolarised ^{129}Xe gas MRI, for both diffusion measurement studies and ventilation imaging, on healthy, asthmatic and cystic fibrosis volunteers.

The first study covered in this thesis aimed to determine the nature of the acinar airway involvement in asthma sufferers via the use of Computed Tomography densitometry and hyperpolarised ^{3}He diffusion MRI at multiple timescales alongside standard lung function tests such as spirometry and multiple breath washout (MBW). It was hypothesised that Asthma patients with an elevated MBW parameter 'S_{acin}' would manifest altered long-range diffusion, as suggestive of intra-acinar airway disease. It was found that there appeared to be an association between the MBW S_{acin} parameter and subtle alterations in diffusion within the acinar airways for participants with asthma, suggesting a structural abnormality in the pulmonary acinus. However, further longitudinal studies are required before the long-term prognostic significance of acinar airway disease in asthma can be determined.

The second study aimed to determine if a relationship exists between measurements from standard lung function test, spirometry and body plethysmography, and the measurements of hyperpolarised ^{3}He diffusion MRI. 18 Cystic Fibrosis patients were recruited, alongside 27 age-matched healthy subjects. It was found that the short timescale diffusion values were lower in patients with Cystic Fibrosis, although not substantial enough to use an indicator to distinguish between a healthy volunteer and a Cystic Fibrosis patient. No strong correlations were found between the lung function measurements and the hyperpolarised ^{3}He diffusion MRI measurements.

The final section of this thesis looks at the preliminary results of a pilot study to develop scan sequences, protocols and gas delivery of hyperpolarised ^{129}Xe MRI, in preparation for future clinical studies at the University of Nottingham. The main focus was on the development of in vivo ventilation images of the human lungs, to a high standard of quality and repeatability. Good progress was demonstrated, with lung images achieved down to 2.5cm thick slices, with initial images of both dynamic ventilation and dissolved-phase ^{129}Xe lung images. However the pilot study was not yet complete, and more development on the techniques discussed was still required.

Publications

Characterization of acinar airspace involvement in asthmatic patients by using inert gas washout and hyperpolarized 3 helium magnetic resonance, Sherif Gonem, **Steven Hardy**, Niels Buhl, Ruth Hartley, Marcia Soares, Richard Kay, Rino Costanza, Per Gustafsson, Christopher Brightling, John Owers-Bradley and Salman Siddiqui. Journal of Allergy and Clinical Immunology, 2015, **137**, Vol. 2, pg 417-425.

Acknowledgements

There are many people I would like to thank for they help both professionally and personally over the course of my PhD. My first thanks go to my supervisor John Owers-Bradley, for giving me the opportunity to perform this research and giving me the support I needed through-out it. I would also like to thank my colleagues in the MIU, Michael Barlow and Brett Haywood for all their invaluable help.

Thanks must also go to my wonderful wife, Jessica, who stuck by my side through-out the good and the bad. Thanks also go to my family, who shaped me into the man I am today, and were always there with a supporting hand if I ever needed it.

My final thanks goes to all my friends at University of Nottingham: David Peat, Richard Cousins, James Thorpe, Bo Zhang, Sarah Heywood, Duncan Parkes, Stuart Bowe, Vicky Hills, Caroline Poyser, Kyle Baldwin, Ryan Beardsley, Josh Whale, Liang Liao to name just a few. Thanks to all your help and company, whether that was around the physics department, down the pub or at the climbing wall.

Contents

List of Figures

List of Tables

Glossary

Term/Abbreviation	Meaning
ACLQ	Asthma Quality of Life Questionnaire.
ACQ	Asthma Control Questionnaire.
ADC	Apparent Diffusion Coefficient.
Body plethysmography	A common pulmonary function test, consisting of the simultaneous measuring of the pressure fluctuations of a sealed box in which the subject resides, and of the pressure and flow rate of inhalation and exhalation through more conventional equipment.
COPD	Chronic Obstructive Pulmonary Disease.
CPMG	Carr-Purcell-Meiboom-Gill.
CT	Computed Tomography.
FEV1	Forced Expiratory Volume in 1 second.
FFT	Fast Fourier Transform.
FGRE	Fast Gradient Echo.
FID	Free-Induction decay .
FRC	Functional Residual Capacity.
FVC	Forced Vital Capacity.
GE	General Electric.
Kco	The rate of disappearance of CO from alveolar gas during breath-holding.
LCI	Lung Clearance Index.

Continued on next page...

Term/Abbreviation	Meaning
MBW	Multiple Breath inert gas Washout.
MLD E/I	Ratio of expiratory Mean Lung Density to inspiratory Mean Lung Density.
MRI	Magnetic Resonance Imaging.
NMR	Nuclear Magnetic Resonance.
RF	Radio-Frequency.
RV	Residual Volume.
P_{15}	Fifteenth lower percentile of the inspiratory lung attenuation curve, as measured by quantitative lung CT.
Spirometry	A common pulmonary function test, consisting of the measuring of lung function via the volume and/or speed of airflow during inhalation and exhalation.
SSFSE	Single Shot Fast Spin Echo.
SAR	Specific Absorption Rate.
S_{cond}	A parameter provided by MBW, associated with the conductive airways.
S_{acin}	A parameter provided by MBW, associated with the acinar airways.
TLC	Total Lung Capacity.
Z Score	Statistical value often used in Spirometry results. It is equal to: (measured value - predicted value) / standard deviation.

1 Introduction

The motivation behind both hyperpolarised ^{3}He magnetic resonance diffusion measurements and hyperpolarised ^{129}Xe magnetic resonance imaging is two-fold. Firstly, to improve upon the currently available methods to diagnose lung disease and monitor disease progression, and secondly, to add to the current understanding of the physiology and development of lung diseases in patients via a non-intrusive method.

One of the most common methods for investigating ventilation and perfusion in the lungs, Computed Tomography (CT), can provide good anatomical images. However, this comes at a high cost due to the dose of ionising radiation required by the technique. A typical CT chest scan may have a dose of 8 mSv, which is approximately equivalent to 3.6 years of background radiation and a lifetime additional risk of fatal cancer of 1 in 2500 per examination [37].

Other clinical measurements (such as spirometry) are less-invasive, but assess the lungs as a single global entity. This can be a problem, as the non-homogeneity of health and disease function across the lung space is well known.

Magnetic Resonance Imaging (MRI) provides a non-invasive method to image the body. However traditional MRI uses the hydrogen atoms present in water, fats and other molecules within the body to provide its signal for imaging, and as the lungs are essentially mostly air little signal is available to provide detailed images. There has been efforts to improve upon the useful

information extracted via traditional MRI, such as Oxygen-enhanced MRI [63], however the use of other non-traditional MRI methods can potentially yield greater results, such as hyperpolarised gas MRI.

This thesis outlines the theory and sequences used in hyperpolarised ^{3}He and ^{129}Xe MR diffusion measurements and imaging. The diffusion measurement techniques detailed are then used to investigate and provide information on asthma and cystic fibrosis, and the results discussed. The development of ^{129}Xe lung magnetic resonance imaging at the University of Nottingham, including ventilation and dissolved-phase imaging, is also discussed, accompanied by preliminary pilot study results.

1.1 Thesis Outline

Chapter 2 introduces the basic anatomy and mechanics of the human respiratory system. This chapter also gives a brief description of the pathology of the diseases included in the studies discussed in Chapters 5 and 6.

Chapter 3 provides an overview of the basic principles of nuclear magnetic resonance and magnetic resonance imaging, from the underlying quantum mechanics, through signal generation and manipulation, to spatial encoding in MRI. This chapter also provides a brief explanation of diffusion measurements and optical pumping methods.

Chapter 4 gives an introduction the MRI pulse sequences used in the later discussed studies, as well as the methods to calculate meaningful results as applicable. This chapter also gives an overview of the image reconstruction techniques used by RECON, a GUI program for reconstructing images from the raw data outputted by MRI scanners.

Chapter 5 applies some of the diffusion measurement sequences discussed in Chapter 4, alongside Computed Tomography (CT) densitometry and spirometry, to help provide information on the nature of the acinar airway involvement in patients with asthma. This work led to one publication: S. Gonem et al. [33].

Chapter 6 investigates potential relationships between the measurements of spirometry and body plethysmography and the measurements taken using some of the ^{3}He MRI sequences discussed in Chapter 4, on both healthy volunteers and patients with Cystic Fibrosis.

Chapter 7 looks at the development of ^{129}Xe lung MRI at the University of Nottingham. It shows early results recovered from the pilot study, included ventilation imaging and dissolved-phase imaging. It ends with a brief discussion of the future work required on this project.

2 The Respiratory System

2.1 Introduction

This section covers the basics of the structure and function of the human lungs, and a brief overview of the common respiratory diseases encountered in the studies conducted. For further reading, see [101], [58] or [20].

2.2 Lung Anatomy and Physiology

2.2.1 The Respiratory System

The respiratory system can be divided into two sections: the upper respiratory, comprising the nasal and oral cavities, pharynx, larynx and trachea; and the lower respiratory tract, consisting of the main bronchi and lungs.

The upper respiratory tract is responsible for filtering, warming and moisturising the air, such that it is in a suitable condition for optimum gas exchange in the distal parts of the lower respiratory tract. For this purpose, it has a large surface area with a rich blood supply, and its epithelium (the tissue lining the cavities and surfaces) is covered by a mucous secretion, with the nasal hairs acting as a filter.

The lower respiratory tract is responsible for gas exchange, connecting to the upper respiratory tract by the two primary bronchi and trachea. The two bronchi then divide inside the lungs into smaller and smaller airways, until the final respiratory airways (acinar airways) are reached. These acinar airways are where the gas exchange takes place.

2.2.2 Lung Development

The lungs first begin to develop approximately 4 weeks after conception, initially consisting of a longitudinal groove on the side of the primitive foregut. This then develops into a bud before bifurcating repeatedly. After about 16 weeks the main conductive airway branching is complete. During weeks 17-28, the basic structure of the acinus develops, as the airways continue to bifurcate, and the acinar blood vessels begin to develop. In the following weeks (29-35), further air spaces appear, known as saccules, which develop epithelium cells similar to that of adult alveoli. True aveoli do not develop until after 36 weeks, and continue to develop well into the first years of childhood. At birth, there are only about 24 million terminal sacs and alveoli, much less than the average adult figure of 300 million alveoli. The first year of life sees a five-fold increase of alveoli, with slower increases maintained after, well up to the 8th year, and perhaps into adolescence [84]. In the first year of life the airways are also remodelled, with an increase length of all airway generations, and further branching of alveolar ducts into further generations. This suggests a risk that events in infancy and childhood can lead to lung impairments later in life. In fact, it has been observed that adults with chronic airflow obstruction had an increased frequency of respiratory infections during childhood [14, 46, 77].

2.2.3 Structure of the Conducting Airways

The conductive airways start at the trachea, and bifurcate down through the generations, getting shorter and narrower as they divide. Table 1 shows the complete airway tree. The conductive airways include all the Bronchi and Membrane Bronchioles, and finish at the Terminal Bronchioles. The Respiratory Bronchioles and Alveolar ducts make up the acinus.

The conductive airways do not contain alveoli in their walls, and so do not participate in gas exchange. Instead they are primarily involved in conducting the air to the more distal airways. The conductive airways are lined with cilia, long slender cells up to $6\mu m$ in length, and mucous cells. These act as the first line of defence against potentially harmful agents that get past the nasal hair filtering.

As the conducting airways do not participate in gas exchange, they constitute the anatomic dead space, with a volume of about 150 ml.

2.2.4 Structure of the Distal Airways

Alveoli first appear occasionally in the airway walls of the Respiratory Bronchioles, and increase in number and density in each subsequent generation until the alveolar duct generations, which are completely lined with alveoli. These airways are where gas exchange occurs, and are collectively known as the acinus.

Table 1: The Weibel Model of the Bronchial Tree

Generation	Name	Number of branches	Diameter (mm)	Length (mm)
0	Trachea	1	18.0	120.0
1	Bronchi	2	12.2	47.6
2	Bronchi	4	8.3	19.0
3	Bronchi	8	5.6	7.6
4	Bronchi	16	4.5	12.7
5	Bronchi	32	3.5	10.7
6	Bronchi	64	2.8	9.0
7	Bronchi	128	2.3	7.6
8	Bronchi	256	1.86	6.4
9	Membr. Bronchioles	512	1.54	5.4
10	Membr. Bronchioles	1024	1.30	4.6
11	Membr. Bronchioles	2048	1.09	3.9
12	Membr. Bronchioles	4096	0.95	3.3
13	Membr. Bronchioles	8192	0.82	2.7
14	Membr. Bronchioles	16,384	0.74	2.3
15	Membr. Bronchioles	32,768	0.66	2.0
16	Term. Bronchioles	65,536	0.60	1.65
17	Resp. Bronchioles	131,072	0.54	1.41
18	Resp. Bronchioles	262,144	0.50	1.17
19	Resp. Bronchioles	524,288	0.47	0.99
20	Alveolar Ducts	1,048,576	0.45	0.83
21	Alveolar Ducts	2,097,152	0.43	0.70
22	Alveolar Ducts	4,194,304	0.41	0.59
23	Alveolar Ducts	8,388,608	0.41	0.50

Source: [102].
These data are based on a combination of morphometry and assumption.

The length of each acinus, from the terminal bronchioles to its most distal alveolus is typically only a few millimetres. Diffusion is the chief source of the movement of gases through this region. This region makes up the majority of the lung, with a volume around 2.5-3 L.

The acinar airways comprise the majority of the airway surface area in the lung [100]. The acinar airways begin at around the 15th branching generation, and consist of the respiratory bronchioles, alveolar ducts and alveolar sacks (with alveoli incorporated into the airway walls). Figure 1 shows a diagram of some of the acinar airways, from generation 17 onwards.

Figure 1: Diagram of the Acinar Airways (from generation 17+).

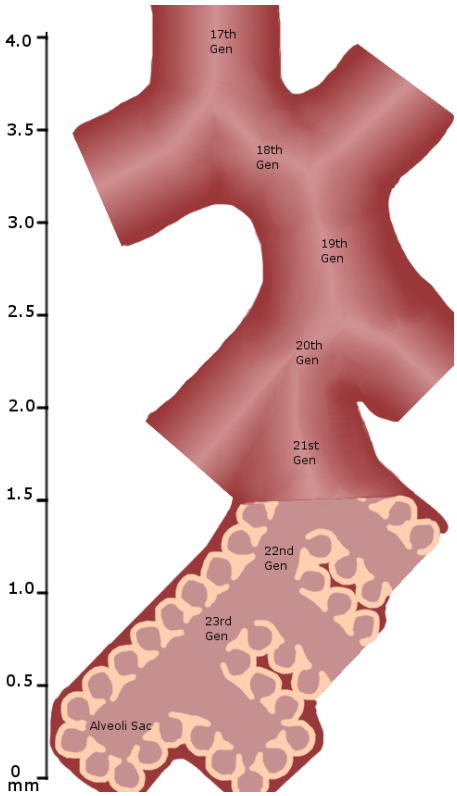

2.2.5 Lung Ventilation Mechanics

The movement of air in and out of the respiratory system is known as ventilation. Ventilation can be determined and controlled by the respiratory rate (number of breaths per minute, typically 12-20) and the tidal volume (the amount of air that enters the lung with each breath).

When the lung volume is changed (i.e. the expansion or contraction of the chest) a pressure differential is formed between the inside of the lungs and the surrounding atmosphere, causing air to move in or out of the lungs towards the lower pressure area.

The main muscle involved in inspiration is the diaphragm. The diaphragm is a dome-shaped muscle upon which the lungs sits, and upon contraction flattens out. Aiding this are the external intercostal muscles, which raise the rib cage. The result is an increase in the volume of the chest (intra-thoracic volume), lowering the air pressure inside, and hence driving air flow into the lungs.

In comparison, expiration is largely the result of the elastic recoil of the lung tissue upon relaxation of the intercostal muscles and diaphragm. However, expiration can be forced (such as during coughing), in which the internal intercostal muscles are used to lower the rib cage, and the abdominal muscles are used to increase the intra-abdominal pressure, forcing the abdomen against the diaphragm.

2.2.6 Gas Exchange Mechanics

The walls of the alveoli contain pulmonary capillaries, with approximately half its surface area having only a 0.2-0.3μm barrier between the blood and the gas. This provides an ideal location for gas diffusion in and out of the blood. However, the thin barriers increase the risk that if the capillary pressure rises to abnormally high levels, or the tension of alveolar wall is greatly increased (i.e. from inflating the lungs to very high volumes), the barriers can be damaged.

Simple diffusion drives the movement of gas through the barrier, according to the partial pressure differences between the gas area and the blood. This process can be described by Fick's law:

$$\frac{dV_{gas}}{dt} = \frac{AD}{T}(P_1 - P_2), \tag{1}$$

where $\frac{dV_{gas}}{dt}$ is the change in the Volume of gas over time, A is the surface area available for diffusion, T is the barrier thickness, D is a diffusion constant (which depends on the properties of the tissue and gas selected), and P_1 and P_2 are the partial pressures on either side of the barrier. The partial pressure of a specific gas can be calculated by multiplying its concentration by the total pressure. The diffusion constant D is inversely proportional to the gas's molecular weight, and proportional to the gas's solubility. This leads to CO_2 diffusing 20 times more rapidly than O_2 through the blood-gas barrier, due to its high solubility.

2.2.7 Lung Cleaning Mechanics

The lungs have a variety of defences and methods to keep them clean. The nasal hairs help to filter out the larger particles, preventing them from entering the lungs. Smaller particles are captured by the mucus that lines the conductive airways, secreted by the epithelial cells there. Once captured the mucus (and captured particles) are expelled via two methods. The first, and fastest, method is to cough. During a cough high air velocities are reached in the conductive airways, which is sufficient to remove mucus and particles from the smaller airways. The second method is much slower, where the small finger-like protrusions known as cilia which line the conductive airways continually waft, gradually carrying the mucus and particles up towards the oesophagus to be swallowed. The final lung cleaning mechanism deals with the very smallest particles, that make it all the way to the alveoli. Once there they are deposited on the alveoli lining, and are engulfed by large cells known as macrophages. The particles are then removed via the circulatory or lymphatic system.

2.3 Lung Pathology

2.3.1 Asthma

Bronchial asthma (aetiologically distinct from cardiac asthma) is a condition in which breathing is intermittently difficult, due to narrowing of the bronchi. Bronchial asthma (hereafter referred to as just asthma) is characterised by episodic 'attacks', consisting of wheezing, tightness of the chest, shortness of breath and coughing. During exhalation the effect of an asthma 'attack' is more noticeable, as this is the respiration phase where the

airways normally collapse, and because the muscles involved in expiration are weaker than the muscles involved in inspiration.

There are two types of asthma, extrinsic and intrinsic. Extrinsic asthma is associate with an exposure to a wide range of allergens, such as fur, feathers, pollens, or house dust mites. It is the most common of the two asthma types, and usually begins in childhood, and tends to become less severe with age, though some continue to have symptoms in adult life. Intrinsic asthma is not associated with an external stimuli, and is most often onset in adult life. It is chronic, tending to worsen with age.

The narrowing of the airways has been seen to be caused primarily by three processes: increased amounts of mucus, inflammatory oedema (inflammation due to fluid build-up in the cells) and muscular hypertrophy (the increase in size of muscle cells). These three processes are found to occur mainly in the bronchi, but can also be found in the smaller airways, including the bronchioles. The alveoli may also be involved [52].

There are many trigger factors for both extrinsic and intrinsic asthma, via either an inflammatory or neurological mechanism. Asthmatics are usually over-responsive to irritant dusts, respiratory infection and large volumes of cold dry air (such as experienced during outdoor exercise, or during winter). Emotional stress can also be a triggering factor in asthma.

Asthma can be managed quite effectively by avoidance of the identified triggers, with the use of bronchodilator drugs and corticosteroids as required. Breathing exercises and desensitisation to specific allergens are often supplemented alongside. Recently other treatments have been developed, including leukotriene and leukotriene receptor antagonists, antibodies directed against IgE, and the identification of several genes relating to asthma, suggesting that a gene therapy treatment may be developed at a future date.

2.3.2 Cystic Fibrosis

Cystic Fibrosis is a genetically inherited condition characterised by abnormal secretions. Only as little as 50 years ago a cystic fibrosis patient was not expected to live past the first year of life, whereas now most can be expect to survive until the fourth decade of life. It is reported across all racial groups, although it is more common in Caucasian people (in the UK 1 in 2500 are born affected, with 1 in 25 carrying the the responsible recessive gene).

The genetic abnormality affects a protein known as Cystic Fibrosis Transmembrane Conductance Regulator (CFTR), which helps control ion, and hence water, movement across the cell membrane. This results in excessive re absorption of water, leading to the hyper-viscosity of mucus and hyper-salinity of sweat and mucosal secretions.

The hyper-salinity impairs the antibacterial action of constituents such as lactoferrin and lysozyme in the airways, and when combined with the difficulty in clearing the hyper-viscous mucus leads to permanent infections and inflammation of the respiratory tract. The hyper-salinity and hyper-viscosity resulting from the defective CFTR gene can also affect the Cystic Fibrosis sufferer in other areas of the body, such as the reproductive system and pancreas.

Repeated pulmonary infection remains the major clinical problem in Cystic Fibrosis, despite improvements in patient care, with the cause of death in adults usually being bronchopulmonary infection, respiratory failure and cor pulmonale (abnormal enlargement of the right side of the heart).

3 NMR, MRI and Polarisation

3.1 Nuclear Magnetic Resonance

3.1.1 Introduction

This section provides a concise overview of the theory behind Nuclear Magnetic Resonance (NMR), but is in no means a complete review. A complete explanation of all the basic principles already exists in many texts elsewhere [51] [53] [31].

NMR is based on the magnetic properties of the atomic nucleus, due to its proton and neutron components. The Hydrogen nucleus (also referred to as proton or ^{1}H) is the most common target of NMR, due to its relatively high thermal polarisation at room temperature, and its abundance in the human body (63% by atomic count [22]).

3.1.2 Nuclear Spin and Angular Momentum

Nuclei lie at the heart of NMR, and consist of two particles, protons and neutrons. These particles have many properties, but the most significant, at least to NMR, is their intrinsic spin and electric charge.

Intrinsic spin is quantum mechanical in nature, but can be visualised as the rotation of the particles as it is a form of angular momentum. The total spin angular momentum of a particle with spin takes the form of $[S(S+1)]^{1/2}\hbar$, where S is the spin quantum number. Protons and neutrons, being fermions, have half-integer spins, or more specifically, have spin=$1/2$.

The total spin angular momentum of a system comprising more than one particle, such as a nucleus, is given by $[S_n(S_n+1)]^{1/2}\hbar$, where S_n can take one of multiple forms, arising from the addition or subtraction of the individual particle's spin. For example, in a two-particle system, S_n can take one of the following possible values:

$$S_n = \begin{cases} |S_1 - S_2| \\ |S_1 + S_2| \end{cases} \tag{2}$$

In the case of two particles with half-integer spin, i.e. $S_1 = S_2 = 1/2$, there are only two possibilities for the total spin angular momentum, either $S_n = 0$ or $S_n = 1$. This often expressed as "opposing spins" where the spins cancel out to make $S_n = 0$, or "parallel spins" where the spins add to make $S_n = 1$. The different states that S_n are dependant on the energy of the system. The lowest energy is often referred to as the Ground state.

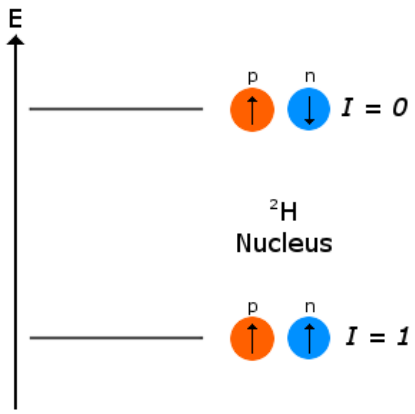

Figure 2: Diagram representing the total spin energy levels of a ^{2}H nucleus.

In the case of nuclei, the combination of the spins of the protons and neutrons is known as Nuclear Spin, and is conventionally denoted I. For example, in the case of the nucleus of ^{1}H, which consists of just one proton, has only $I = 1/2$, whereas the nucleus of ^{2}H, consisting of a proton and a neutron, can have either $I = 0$ or $I = 1$. The energy difference between the two spin states is $10^{11} kJmol^{-1}$, which is vastly surpasses the energies available in standard chemical reactions, electromagnetic fields, or thermal energy at room temperature, hence the higher state ($S_n = 0$) is only ever seen in exotic circumstances. Again, the value of I of the lowest energy is called the ground state nuclear spin. There is generally no simple rule for determining which of the states is the ground state.

3.1.3 Zeeman Splitting

A spin I nuclear state is degenerate, by $(2I + 1)$, and this degeneracy is broken if a magnetic field is applied. This splitting is known as nuclear Zeeman splitting. It is these nuclear Zeeman sub-levels that provide the NMR spectroscopy.

3.1.4 Magnetic Moment and Larmor Frequency

The nuclear magnetic moment, like spin, is an intrinsic quantum mechanical property. The magnetic moment and spin angular momentum are closely linked, and are proportional to each other:

$$\boldsymbol{\mu} = \gamma \boldsymbol{S} \tag{3}$$

where $\boldsymbol{\mu}$ is the magnetic moment, and γ is the gyromagnetic ratio. This is usually specified in units of $rads^{-1}T^{-1}$, and can be either positive or negative, where a negative value means that the direction of the magnetic moment is in the opposite direction of the spin angular momentum. As with spin, the magnetic moment of a nucleus is derived from its particles. The gyromagnetic ratio of common atomic nuclei can be seen in Table 2.

Table 2: Selection of Nuclear Isotopes for NMR.

Isotopes	Ground-State Nuclear Spin	Natural Abundance (%)	γ $(10^6 rads^{-1}T^{-1})$
^{1}H	1/2	99.99	267.513
^{2}H	1	0.012	41.065
^{3}He	1/2	*	203.789
^{7}Li	3/2	92.41	103.962
^{13}C	1/2	1.07	67.262
^{17}O	5/2	0.038	36.264
^{31}P	1/2	100	108.291
^{129}Xe	1/2	26.44	73.997

*: ^{3}He obtained from tritium decay.
Sources: [8, 99, 104].

Just as classical angular momentum is a vector, so is the angular momentum of a particle with spin. Hence it can point in any direction in space, and its direction is often referred to as the spin polarization axis. Generally, particles with spin have their axes pointing in all possible directions. The magnetic moment of a particle is also a vector, and can either point in the same direction as the spin polarization axis or against it, depending on its γ value.

When a magnetic field is applied, it would be expected that the particles rotate to align the magnetic moment with the field, and reduce the magnetic energy. However, the spin vector actually moves around the field, on a cone, with a constant angle between the magnetic moment and the field (see 3). This is known as spin precession. This behaviour is due to the fact that the particles have angular momentum as well as a magnetic moment. The frequency of the precession (ω_0) is given by:

$$\omega_0 = -\gamma B_0 \tag{4}$$

where B_0 is the applied magnetic field and γ is the gyromagnetic ratio as before. In the case of nuclei, the frequency of precession is known as nuclear Larmor frequency. It is usually expressed as an angular frequency with units of $rads^{-1}$. As γ can be either positive or negative, so can the Larmor frequency. Its sign represents its direction of rotation, with a negative value representing a precession in the anti-clockwise direction, when seen looking up along the direction of the magnetic field.

3.1.5 Spin-Lattice Relaxation and Net Magnetisation

As mentioned before, in the absence of a magnetic field the spin directions of nuclei are uniformly distributed in space, and when the the magnetic field is applied, they begin to precess around it, at uniformly distributed angles from their initial starting positions. At this point, the net magnetic moment of the particles is close to zero, as the contributions from individual spins approximately cancel each other out.

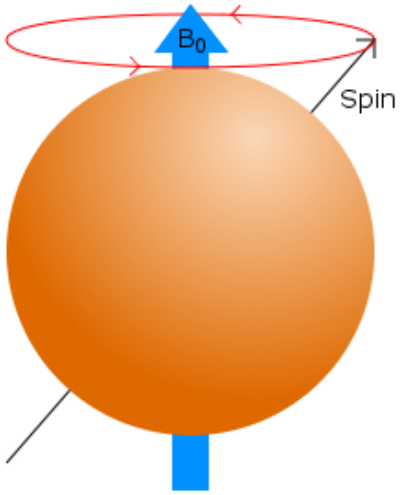

Figure 3: Diagram of Spin Precession

However in the case of the ^{1}H nucleus, for example in a typical sample consisting of water molecules, it is not that simple. The molecule is full of magnetic particles, such as electrons and the neighbouring nuclei. These are all sources of very small local magnetic fields that are fluctuating in both magnitude and direction, due to thermal agitation. So the spin precession of a single nucleus at any given moment may vary slightly in both frequency and direction to that of its neighbouring nuclei.

Over time this leads to the spin polarization to have a 'wandering' motion. The time-scale for this is often in seconds. However this wandering motion is not entirely isotropic, as the finite temperature of the environment means that there is a slightly higher probability that the wandering motion will move towards alignment with the applied field, rather than against it. This bias eventually leads to a thermal equilibrium, with a stable distribution of nuclear spin polarization favouring the field alignment. This distribution is stable on a macroscopic scale, as the individual nuclei have

still got wandering spin polarizations. This net distribution of spin polarization orientations, and therefore magnetic moments, leads to a small net magnetic moment across the sample in the direction of the field, known as the total magnetisation. The process of magnetisation growth is known as longitudinal relaxation, or Spin-Lattice relaxation, where longitudinal term indicates that it is occurring along the applied field axis. The lattice term is derived from the early days of NMR and refers to all the constituents of the sample surrounding the spin, and the term relaxation is used to describe the re-establishment of a thermal equilibrium.

When a field is first applied, the net magnetisation is zero. The gradual build up of the magnetisation due to this spin-lattice relaxation is approximately exponential, and has the form:

$$M_z(t) = M_{eq}(1 - e^{-t/T_1}) \tag{5}$$

where M_z is the net magnetisation in the z-direction (along the applied magnetic field) at time t, M_{eq} is the net magnetisation in the z-direction at thermal equilibrium, and T_1 is a time constant known as either spin-lattice relaxation time constant or longitudinal relaxation time constant.

3.1.6 Rotating and Detecting the Magnetisation

When the magnetisation is aligned with the applied magnetic field, it is almost undetectable, as it is around four orders of magnitude less than the diamagnetism of the sample, originating from its electrons. So the magnetisation perpendicular to the applied field is measured.

As described in the previous section, a sample comes to thermal equilibrium and has a net magnetisation in the z-direction (along the applied magnetic field). However it still has a random distribution of magnetisation in the x and y directions, leading to a zero net transverse magnetisation. However a radio frequency pulse (r.f. pulse) can be applied along another axis to rotate the magnetisation into the transverse plane.

A coil that is wound around the x-axis and has r.f. power supplied to it produces an oscillating magnetic field along the x-axis. This field is represented by the symbol B_1, and has a frequency of ω_{tx}, where the tx signifies that it is transmitted along the x-axis.

When the spin system is looked at in a rotating frame around the z-axis, instead of the laboratory frame, the effective magnetic field of both the static and oscillating field changes. Taking a rotating frame frequency ω_{rot}, and the Larmor frequency of the spin precession ω_0, we have a frequency offset Ω, of:

$$\Omega = \omega_0 - \omega_{rot} \tag{6}$$

If we place this and rearrange the equation for the frequency of precession around a magnetic field (equation 4), we find that we get an expression for the apparent, or reduced, field ΔB:

$$\Delta B = -\frac{\Omega}{\gamma} \tag{7}$$

It can be seen from this that as the frequency of the rotational frame approaches the Larmor frequency, the reduced field goes to zero.

As for the oscillating field, if the frequency of the oscillating field matches that of the rotating frame, then it appears as a constant field in the x-axis. Hence in a rotating frame of frequency $\omega_{rot} = \omega_{tx}$ we have the reduced field in the z-direction and the B_1 along the x-axis, which add vectorially to give an effective field B_{eff}, of magnitude:

$$B_{eff} = \sqrt{B_1^2 + (\Delta B)^2} \tag{8}$$

Just as there is a precession around the B_0 field in the Laboratory frame, there is a precession around the B_{eff} field in the rotating frame. As usual, the frequency ω_{eff} of this precession is given by:

$$\omega_{eff} = |\gamma| B_{eff} \tag{9}$$

In this case we take the absolute value of γ such that ω_{eff} is always positive. If the offset Ω is small, the B_{eff} will lie close to the x-axis, and so the magnetisation will be rotated out of the z-axis. For the case of an on-resonance pulse (i.e $\omega_{rot} = \omega_{tx} = \omega_0$), we see the reduced field will go to 0, so B_{eff} will be equal to B_1, and so we define the precession frequency as $\omega_1 = |\gamma| B_1$. So if an on-resonance pulse is applied, for time t_p, the magnetisation is rotated by an angle of β radians:

$$\beta = \omega_1 t_p \tag{10}$$

where β is known as the flip angle of the pulse. So if the pulse length is set such that $\beta = \frac{\pi}{2}$, then the net magnetisation will now be along the y-axis (of the rotating frame). Hence in the Laboratory frame, the net magnetisation is now rotating in the transverse plane at the Larmor frequency, and can be detected by the placing of a 'receive' coil near the sample, where it induces an oscillating emf which can be amplified and detected.

After an rf pulse has been applied, and the magnetisation rotated into the x-y plane, it will begin to decay back towards the z-axis due to spin-lattice relaxation, as described earlier.

3.1.7 Transverse Relaxation

After a rf pulse is applied, and the spins rotated into the x-y plane, a signal can be detected in the receive coil. However this signal will soon begin to decay, over a shorter time then expected for spin-lattice relaxation. This is due to transverse relaxation.

Immediately following the B_1 rf pulse the spins are in phase, adding up to a net rotating magnetisation. As discussed in the previous section, the microscopic field is always slightly fluctuating, meaning that each spin is precessing at a slightly different rate. This leads to a dephasing of the spins, reducing the macroscopic magnetisation along the x-y axes. Eventually the spins will dephase enough such that they are all randomly distributed, producing a net transverse magnetisation of zero.

The macroscopic field (split into components x and y), at time t after a 90°pulse is given by:

$$M_x(t) = M_{eq} sin(\omega_0 t) e^{-t/T_2} \tag{11a}$$

$$M_y(t) = -M_{eq} cos(\omega_0 t) e^{-t/T_2} \tag{11b}$$

where M_{eq} is the magnetisation in the z direction at thermal equilibrium before the pulse, and T_2 is the transverse relaxation time constant.

Often in practice the applied field is not perfectly homogeneous, or there may be localised magnetic material in or near the sample which gives rise to a non-homogeneous field across the sample. This will cause transverse relaxation to occur faster, due to a smaller time constant. In this case, the time constant of the decay is denoted as T_2^*, to represent that it is a combination of both the microscopic field fluctuations, which leads to an irreversible decay, and macroscopic field inhomogeneity, whose effect can be reversed with a spin echo (see next section).

The oscillating signal and subsequent decay of signal in the receive coil after a pulse is referred to as a an NMR signal, or free-induction decay (FID).

3.1.8 The Spin Echo

The spin echo sequence is one of the basic types of pulse sequences, where a FID signal is generated by applying a rf pulse (usually $\frac{\pi}{2}$), allowed to dissipate due to T_2^* decay or forced to dissipate due to applied field gradients, and some of the decay reversed by the application of a 180° pulse.

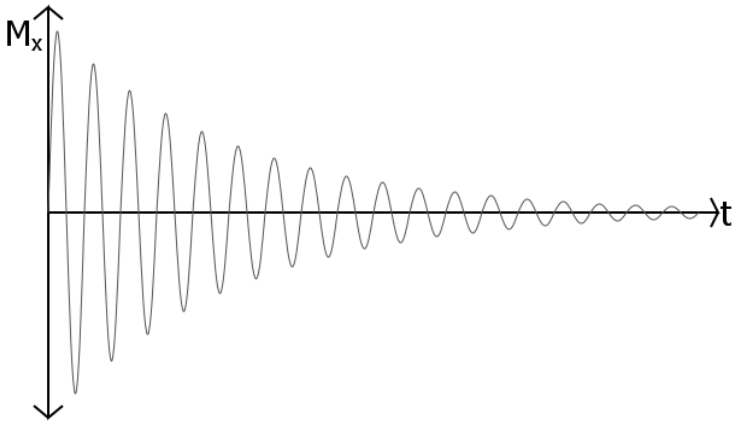

Figure 4: Decay of the NMR signal over time due to Transverse Relaxation

Fig 10 illustrates the effect that a 180° pulse has on the transverse magnetisation. As can be seen, the signal is generated by the first application of a pulse (in this case 90°), and then is lost as the spins go out of phase due to inhomogeneities in both the local and applied fields. Then when the 180° pulse is applied along the x-direction, the spins are rotated 180° around the x-axis. The process that originally de-phased them then returns them back into phase, and a signal is seen (known as a spin echo).

The amplitude of the echo seen is lower than the original FID, due to T_2 decay that has occurred during the time taken to create the echo. A shorter time period between the original production of the signal and the creation of the echo (know as the echo time, T_e) results in a larger echo signal. By varying the echo time, the spin echo can be used to measure T_2.

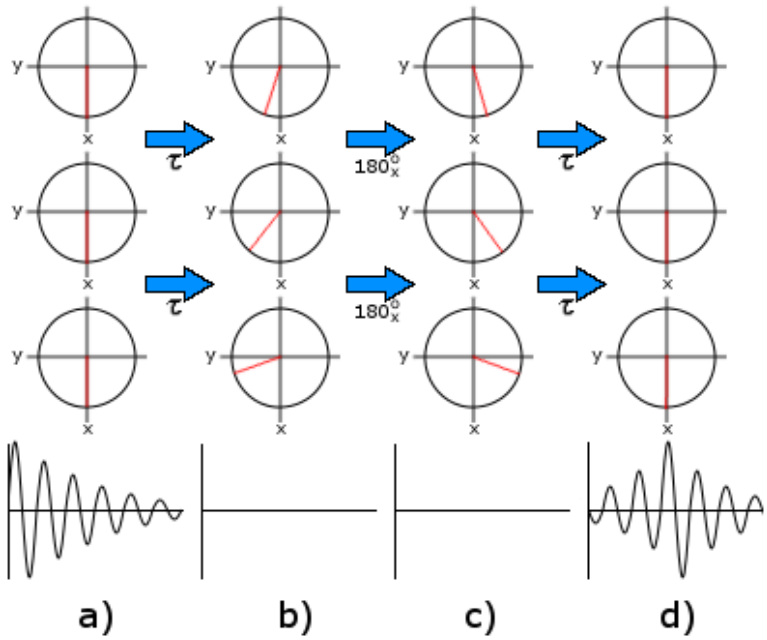

Figure 5: Illustration of the Spin Echo Process

a) Following an rf pulse the spins are initially in phase with each other, producing an FID. b) After time τ, the spins have precessed at different rates, and are no longer in phase, so there is no signal. c) After a 180° pulse, the spins are flipped around the x-axis. d) The spins precess at the same rate as before, causing the signal to return after time τ.

3.2 Magnetic Resonance Imaging

3.2.1 Introduction

This section explains how useful information and/or images can be extracted from the NMR signal as described in the previous section. This is an overview, as more details can be found in texts elsewhere [59] [53] [51].

3.2.2 The Magnetic Gradient

The magnetic field gradient is another important part of both NMR and MRI sequences, alongside the main applied magnetic field B_0, and the rf pulse B_1. As its name suggests, the gradient alters the B_0 field, such that it increases across one dimension, usually with the original B_0 field strength in the centre of the magnet.

As equation 4 describes, the spin precession is dependant on the B_0 field strength, and so when a gradient is applied across a certain dimension, the Larmor frequency of the spins varies across the same dimension. Figure 7 shows the relationship between the magnetic field (with gradient applied across the x-dimension), and the frequency of the precession of the spins across the x-dimension. This effect means that gradients can be a useful tool for manipulating the spins, and hence the NMR signal. A prime example of this is the gradient echo.

3.2.3 The Gradient Echo

The gradient echo is one of the basic types of pulse sequences, where an NMR FID signal is generated via an r.f. pulse, then a gradient is applied to dephase the spins, followed by an equal but inverted gradient is applied to re-phase the spins, generating an echo.

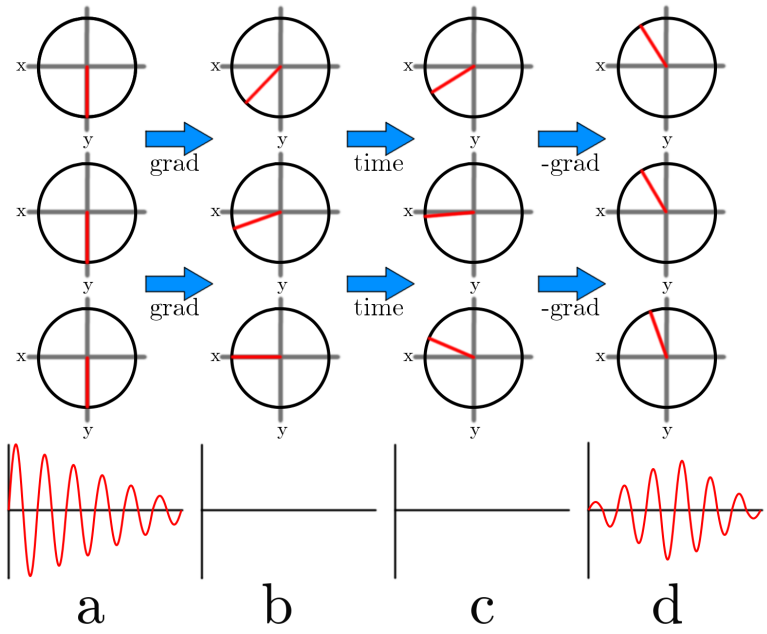

Figure 6: Illustration of the Gradient Echo Process
a) Following an rf pulse the spins are initially in phase with each other, producing an FID. b) With the application of a gradient, the spins precess at different rates, and are no longer in phase, so there is no signal. c) With time, inhomogeneities in the local and external fields have caused the spins to go out of phase further. d) After the application of a second, inverted gradient, the spins precess at different rates and return into phase, causing the signal to return (though slightly lessened due to the de-phasing caused by the inhomogeneities.

Fig 6 illustrates the effect that the two gradients have on the transverse magnetisation. As can be seen, the signal is generated by the first application of a pulse (in this case 90°), and then is lost as the spins go out of phase due to the first applied gradient. Then when an inverted but equal strength gradient is applied the process that originally de-phased the spins returns them back into phase, and a signal is seen (known as a gradient echo).

As for spin echo, the amplitude of the echo seen is lower than the original FID, due to T_2 decay that has occurred during the time taken to create the echo. However, unlike for spin echo, the gradient echo is also reduced due to de-phasing by the inhomogeneities in the field. The combination of this with T_2 leads to a faster decay constant, known as T_2^*. As for spin echo, a shorter time period between the original production of the signal and the creation of the echo (known as the echo time, T_e) results in a larger echo signal. By varying the echo time, the gradient echo can be used to measure T_2^*.

3.2.4 Fourier Transform and Frequency Encoding

As was discussed in the previous section, when a gradient is applied, the spins precess at various speeds. If the gradient is applied during the signal acquisition, the data acquired will consist of a combination of the various frequencies and their relevant intensities. This technique is known as frequency encoding.

Fourier transformation can be used to convert the time-domain data into the frequency-domain. The time-domain data is known as k-space data, as the intensity at various points does not directly correspond to a physical dimension, whereas the frequency-domain data does. Due to the applied gradient the spin precession frequency varies across a single dimension. The physical offsets can be calculated from the frequency offset (as long as the gradient strength is known) from manipulating equation 4.

$$\omega_0 + \delta_\omega = \gamma(B_0 + G_x\delta_x) \tag{12}$$

$$\omega_0 + \delta_\omega = \gamma B_0 + \gamma G_x\delta_x \tag{13}$$

$$\delta_x = \frac{\delta_\omega}{\gamma G_x} \tag{14}$$

where δ_ω is the frequency offset from the pulse frequency ω_0, G_x is the applied gradient strength across the x-dimension, and δ_x is the physical offset of the sample from the centre point of the applied gradient.

3.2.5 Phase Encoding

Frequency encoding, as discussed in the previous section, provides a way to gather spatial information in a single dimension. To acquire information for two dimensions requires an extra set of gradients, that provide phase encoding, across multiple acquisitions.

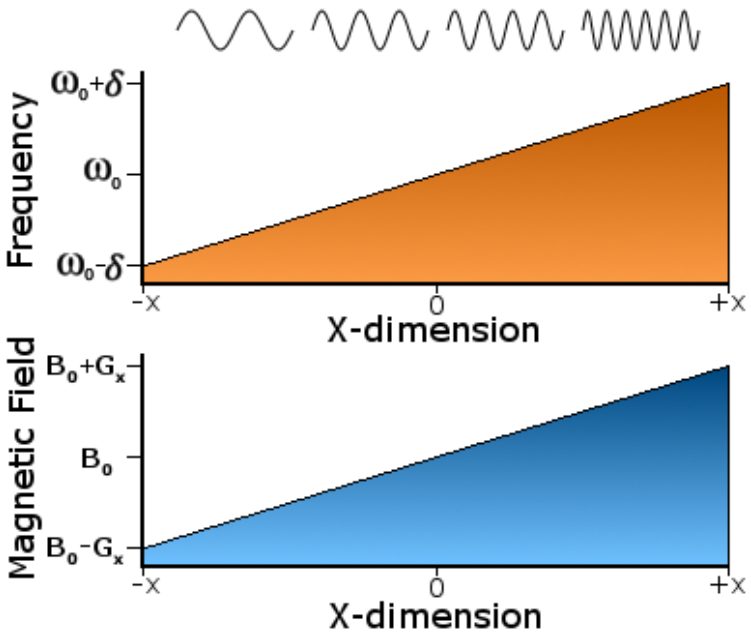

Figure 7: Illustration of the gradient magnetic field and spin precession relationship.

For phase encoding a gradient is applied just before each acquisition, with a different strength each time. This gradient is applied in a perpendicular direction to the frequency encoding gradient, and the effect is to cause the spins to go out-of-phase with each other, along that one direction. By varying the strength of the gradient, the phase shift changes each time. At the end, a 2-dimensional Fourier Transformation can be applied to the resulting 2-dimensional k-space data, recovering both the frequency and phase information, which corresponds to 2-dimensional real space.

3.2.6 Slice Selection

Using the Frequency encoding and Phase encoding, it is possible to get a 2-dimensional image of the sample. However, this 2-dimensional image is a conglomeration of the entire sample in the remaining direction. To limit the "thickness" of the remaining dimension that contributes to the image, known as a slice, a technique known as slice selection is used.

Slice selection works in a similar way to frequency encoding, except the gradient is applied during the initial rf pulse. A gradient, applied in the remaining dimension not used by either frequency or phase encoding gradients, is applied for the duration of the rf pulse. As the Larmor frequency of the spins is dependent on the magnetic field strength, only those spins that are within the bandwidth of the rf pulse are excited. Hence by controlling the gradient strength, rf pulse frequency and RF pulse bandwidth, a single 'slice' of the sample, at a specific thickness and at a specific position can be selected. Once done only this 'slice' will have been rotated into the transverse plane, and hence only this slice will contribute to the NMR signal.

3.3 Diffusion Measurements

3.3.1 Gas Diffusion

The net movement of molecules (or atoms) from a high concentration area to a low concentration area is known as diffusion. Diffusion is considered the result of a 'random walk' of the diffusing particles.

The 'random walk' is the seemingly random motion of an individual atom, ion or molecule through space. However the molecule is not truly moving randomly, but instead its motion is the result of 'collisions' with other atoms, ions or molecules, and only appears to be moving randomly when viewed in isolation. 'Random walk' is governed by the kinetic energy within the system, and is affected by changes in concentration, pressure and temperature. The random motion of particles in a fluid (liquid or gas) due their collisions is also known as Brownian motion.

For an unrestricted sample (where molecules are able to move freely), then the displacement of particles in one direction is the equal to the displacement of particles in all other directions. When considering only a single dimension, the mean squared displacement ($\bar{x^2}$) for a given particle in a sample after a time t is given by:

$$\bar{x^2} = 2Dt \tag{15}$$

where D is the diffusion coefficient of the sample in question. This means that if displacement of particles in a sample can be measured, the diffusion coefficient of the sample can be calculated.

However if the sample is in restricted space, such as for gas in the airways of the lungs, the mean displacement of a particle is reduced, and hence the measure diffusion coefficient is lower than that for the unrestricted space. This lowered diffusion coefficient is sometimes known as Apparent Diffusion Coefficient (ADC). The more restrictive the space, the lower the measured ADC will be compared to the sample unrestricted diffusion coefficient.

3.3.2 Measuring Diffusion in MRI

The diffusion of liquids and gases in a sample is sometimes of interest to researchers, and can be probed using MRI.

To probe the diffusion of a liquid or gas, a pair of diffusion weighting gradients are used. The diffusion gradients consist of one gradient to dephase the spins, and another of equal area but opposite direction to rephase the spins. A prime example of this is the Pulsed Gradient Spin Echo sequence, shown in Figure 8 Any spin that moves (due to diffusion) during that time will not experience the correct re-phasing magnetisation, and so will not contribute to the final NMR signal, reducing the overall signal.

The effect on the signal intensity by diffusion weighting (ignoring other effects such as relaxation) can be described by:

$$S = S_0 e^{-bD} \tag{16}$$

where S is the signal seen, S_0 is the signal intensity without diffusion weighting gradients, D is the diffusion coefficient of the sample, and b is the b-value, a term expressing the amount of diffusion sensitivity applied by the gradi-

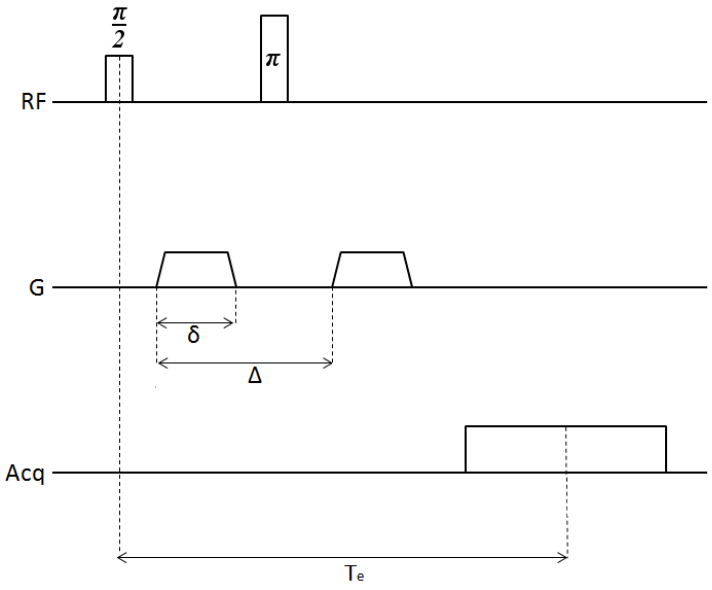

Figure 8: Illustration of the pulsed gradient spin echo (PGSE) sequence.

ents. The b-value is expressed as:

$$b = \gamma^2 G^2 \delta^2 (\Delta - \frac{\delta}{3}) \tag{17}$$

where γ is the gyromagnetic ratio, G is the strength of the applied gradient fields, δ is the length of the time each gradient lasts, and Δ is the time between the de-phase and re-phase diffusion weighting gradients.

Graph 9 shows the theoretical signal strength of two Spin Echo sequences, one without any diffusion weighting gradients, where the decrease in signal strength over time is due to T_2 decay alone, and the other with diffusion weighting gradients, where the decrease in signal strength over time is due to both T_2 decay and diffusion.

Figure 9: Signal Decay due to T_2 and Diffusion.

Graph showing signal decay due to T_2 compared to signal decay due to T_2 and diffusion.

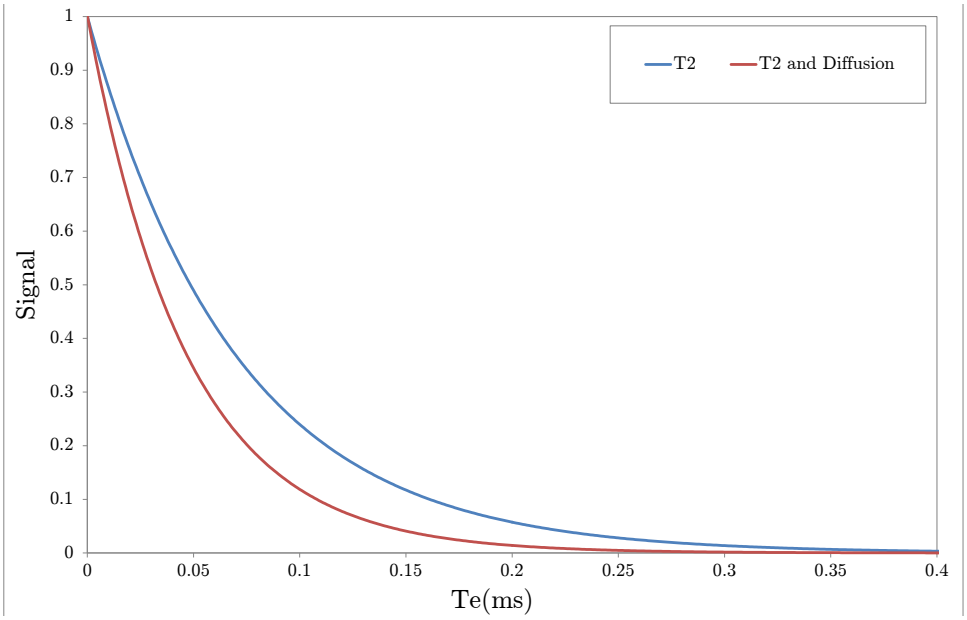

3.3.3 The Yablonskiy Model Approach

In 2008, Yablonskiyy et al. introduced a model-based method to provide quantitative valujes of physiological parameters from a single hyperpolarised ^{3}He MRI scan [109]. The approach is based on a model of lung gemoetric structure, where lung acinar airways are treated as a network of cylindrical passages. Each of these passages are covered with alveolar sleeves. The main geometric parameters characterising these airways are the internal acinar airway radius r, the sleeve width h, the outer acinar radius R (where $R = r + h$), and the effective alveolar diameter L. In the model adopted by Yablonskiiy et al., each alveolus occupies one-eighth of the annular ring, and hence L is related to R by $L = 2R\,sin(\pi/8)$.

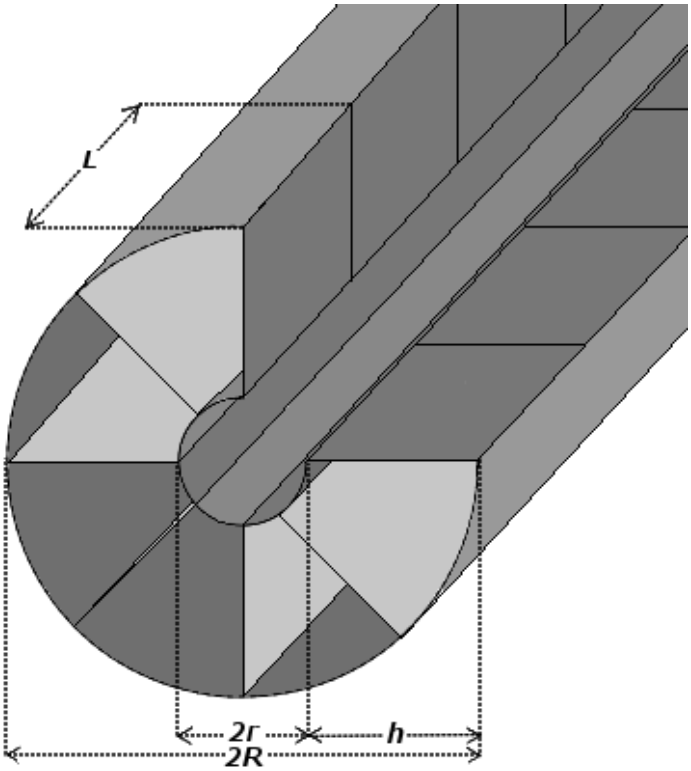

Figure 10: Schematic of an Acinar Airway for the 8-Alveolar Cylindrical Lung Model

Equation 16 for signal attentuation assumed that the Diffusion coefficient was constant regardless of the direction study. However as the alveolar walls, alveoli wells, and other branches of the airway tree each serve as obstacles to diffusing atoms, the restrictions are substantially less along the airway axis than perpendicular to it. Therefore, the measured diffusion coefficient (from here on known as the Apparent Diffusion Coefficient, ADC) depends on the angle between the airway's principle axis and the direction of the diffusion-sensitising gradient (α):

$$S = S_0 e^{-b\,ADC(\alpha)}, \tag{18}$$

which, due to the cylindrical symmetry of the airways in the model, can be split into longitudinal and transverse diffusion coefficients (D_L and D_T):

$$ADC(\alpha) = D_L\,cos^2(\alpha) + D_T\,sin^2(\alpha) \tag{19}$$

The lung consists of a large number of acinar airways, all in different orientations. Even in each voxel of an MRI scan, there a large number of airways, such that the orientation distribution function can be taken as uniform. This means that the signal attenuation for each b-value can be written as [108]:

$$S(b) = S_0 e^{-b\,D_T} \frac{\pi}{4b\,D_{AN}}^{1/2} \Phi[(b\,D_{AN})^{1/2}], \tag{20}$$

where $D_{AN} = D_L - D_T$ and $\Phi(x)$ is the error function. The validity of this equation was confirmed in vivo by experimental measurements in humans [107, 109], canines [81], mice [65, 95] and rats [45, 106] using hyperpolarised

^{3}He gas MRI.

To infer lung micro-structure physiology from the measured diffusion coefficients D_L and D_T, their dependencies on the geometric parameters R and h must be found. These were achieved by means of computer Monte-Carlo simulations [81]. The results were summarised as:

$$
\begin{aligned}
D_L &= D_{L0}\,(1 - \beta_L\, b\, D_{L0}) \\
D_T &= D_{T0}\,(1 + \beta_T\, b\, D_{T0}) \\
\frac{D_{L0}}{D_0} &= e^{-2.89(h/R)^{1.78}} \\
\beta_L &= 35.6(R/L_1)^{1.5} e^{\frac{-4}{\sqrt{h/R}}} \\
\frac{D_{T0}}{D_0} &= e^{-0.73(L_2/R)^{1.4}}(1 + e^{-A(h/R)^2}(e^{-5(h/R)^2} + 5(h/R^2) - 1)) \\
A &= 1.3 + 0.25e^{14(R/L_2)^2}
\end{aligned}
$$

3.4 Polarisation of Noble gases

3.4.1 Introduction

There are many other nuclear isotopes other than ^{1}H that have a non-zero Nuclear Spin ground-state, and therefore will produce an NMR signal (see Table 2). Of particular interest are those that are non-toxic and in gaseous form, as they can be used to fill the normally 'empty' region of the lungs for MRI scans. However before they can be used, they must have a high enough magnetisation in order to get a good NMR signal. The magnetisation (M_0) produced by a sample of any of these isotopes is given by [36]:

$$M_0 = \frac{1}{2} N_S \gamma \hbar P, \tag{21}$$

where N_s is the number of nuclear spins, and P is the polarisation, i.e. the proportion of the nuclear spins in a sample that occupy the same state at thermal equilibrium. The polarisation is dependant on temperature (T) and the applied magnetic field (B_0) [36]:

$$P = tanh(\frac{\gamma \hbar B_0}{2kT}), \tag{22}$$

where k is Boltzmann's constant. Due to the relative weakness of nuclear magnetic moments, it is generally true that $\gamma \hbar B_0 / kT \ll 1$, which yields:

$$P \approx \frac{\gamma \hbar B_0}{2kT}. \tag{23}$$

For example, a sample of protons at room temperature in a field of 1.5 T have $P \approx 5.23 \times 10^{-6}\%$. A sample of ^{129}Xenon nuclei would only have a little less, $P \approx 1.45 \times 10^{-6}\%$. However, Xenon is a gas at room temperature, so its spin density is vastly lower, so a sample of the same volume would be several orders of magnitude less. This presents a problem, as from equations 21-23 it can be seen that to increase the magnitude at thermal equilibrium, one would have to either increase B_0, which becomes increasingly more expensive and difficult, or by decreasing T drastically, which would be inappropriate for various samples, such as those involving living organisms.

Instead, a sample can achieve higher nuclear polarisation by raising it to a non-equilibrium state. The sample would then succumb to spin-lattice (T_1) relaxation, but provided that any useful experiments are performed faster than this relaxation, a stronger NMR signal can be detected for the duration of the experiment/s.

Optical pumping is one such method for attaining high non-equilibrium nuclear spin polarisations, and can provide an increase of magnetisation by four of five orders of magnitude. Kastler [13, 49] first showed that circularly polarised light could be used to polarise the electronic spin states of gaseous metal vapours, and via hyperfine coupling polarise the nuclei states as postulated by Overhauser [66]. Bouchiat [9] and Grover [38] then showed that via collision and spin exchange the nuclear spin-polarised alkali atoms the polarisation of the nuclear spins of noble gases could be greatly enhanced. Later a second method called metastability exchange optical pumping was developed [7, 18, 27, 80], for pumping helium directly without the presence of

alkali metal atoms.

The following sub-sections contain a brief summary of the two methods for optically pumping noble gases, as used on ^{129}Xe and ^{3}He.

3.4.2 Spin Exchange Optical Pumping

In 1950 Kastler [49] first showed that circularly polarised light could be used to polarise the electronic spin states of gaseous metal vapours, and soon after it was found that hyperfine coupling [66] will lead to a polarisation of the nuclear spin states as well [23, 30]. It was not until 1960 that the technique of nuclear polarisation of the noble gas ^{3}He via spin exchange with optical pumped rubidium was developed [9], and then refined over time to include all the stable noble gas isotopes [38]. The process involved is described below, using the example of polarising the nucleus of ^{129}Xe with Rubidium as the alkali metal.

First circularly polarised resonant light, focussing on the D_1 absorption line, is used to excite the $^{85/87}$Rb $5^2S_{1/2}$ electronic ground state to the $5^2P_{1/2}$ first excited state, according to the selection rule $\Delta m = +1$ (see Figure 11). Hence, electrons in $F = 2, m = -2$ ground state can only be excited to $F = 2, m = 1$ of the excited state, and similarly electrons in $F = 2, m = -1, 0, 1$ can only be excited to $F = 2, m = 0, 1, 2$ respectively. From the excited state, the electrons decay to all ground states with equal probability. The net result is depletion of ground state $^{85/87}$Rb atoms in the lower magnetic quantum numbers, and an increase of ground state $^{85/87}$Rb atoms in the highest magnetic quantum number.

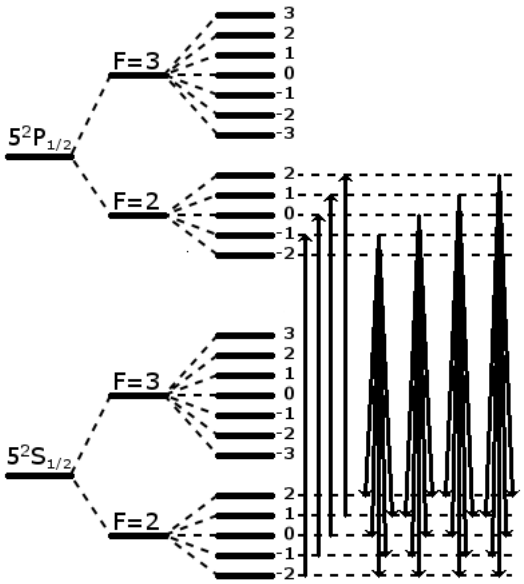

Figure 11: Representation of the rubidium electronic energy levels, and the transitions involved in spin exchange optical pumping.

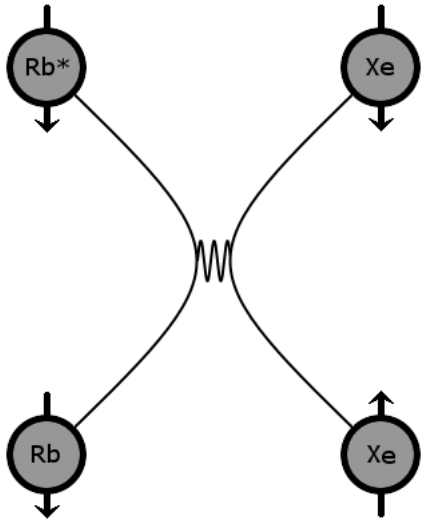

Figure 12: Diagram of the Rb-Xe spin exchange collision.
Electronic polarisation is donated by a *, and nuclear spin state is represented by an arrow.

Spin-exchange optical pumping is most often performed at high pressures, to increase the number of collisions between the $^{85/87}$Rb and the ^{129}Xe and N buffer gasses. Some of these collisions are undesirable, due to spin destruction, but others are useful as they provide the transfer of polarisation from the $^{85/87}$Rb electrons to the ^{129}Xe nuclei. This transfer of angular momentum is a consequence of the Fermi contact hyperfine interaction. See Figure 12 for an illustration of the interaction.

In ideal conditions, with perfect polarisation transfer and minimum spin destruction collisions, the ^{129}Xe nuclei polarisation will tend towards the level of polarisation of the $^{85/87}$Rb electrons.

3.4.3 Metastable Optical Pumping

In 1960 a new technique for the optical pumping of the metastable state of ^{4}He was developed [17]. Then in 1962, the technique was applied to ^{3}He, and was found to also polarise the nuclei of the ground state ^{3}He [18].

The energy levels and excitations involved for the optical pumping of the metastable states of ^{4}He and ^{3}He can be seen in Figure 13. When a low-pressure sample has a rf discharge placed across it, a small fraction of the atoms are excited from the 1^1S_0 electronic ground state to the long-lived 2^3S_1 electronic metastable state (label 1). Circularly polarised light can then be used to excite from the 2^3S_1 to the 2^3P_0 electronic states, according to the selection rule $\Delta m = +1$ (label 2). So the circularly polarised light only excites atoms from the metastable $m = -3/2$ and $m = -1/2$ sub-levels to the $m = -1/2$ and $m = 1/2$ sub-levels respectively. Then the excited atoms decay back to the 2^3S_1 with equal probability (label 3). The net result

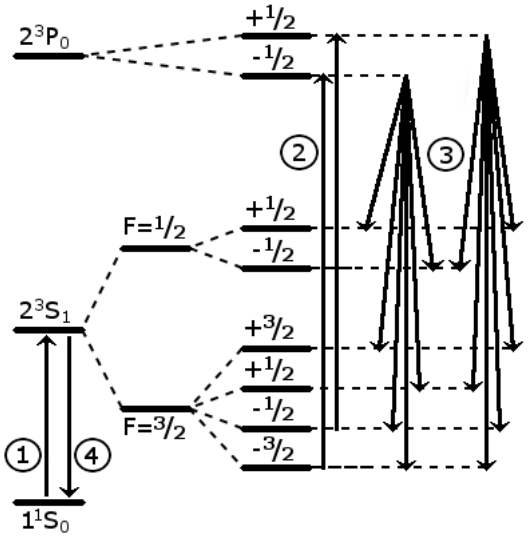

Figure 13: Representation of the helium electronic energy levels, and the transitions involved in metastable optical pumping.

is a depletion of metastable atoms with low magnetic quantum numbers ($m = -3/2, -1/2$) and an increase of metastable atoms with high magnetic quantum numbers ($m = 1/2, 3/2$). In this way the helium metastable states are polarised by the pumping light.

^{3}He has an efficient coupling between its nucleus and its electrons (known as the hyperfine interaction), meaning there is an entanglement of electronic and nuclear spin states. Therefore optical pumping of the electronic angular momentum simultaneously induces nuclear orientation as well [6].

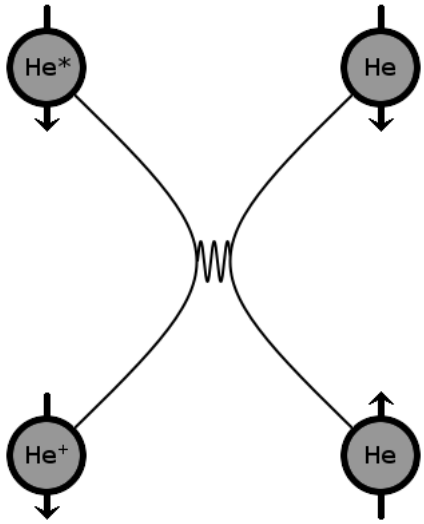

Figure 14: Diagram of the ^{3}He metastable exchange collision.
^{3}He ground-state atoms are denoted He, metastable atoms are denoted He^+, excited metastable atoms are denoted He*, and the nuclei spin state is represented by the arrow.

The metastable electronic state and ground-level states are coupled via metastability exchange collisions (label 4). Figure 14 shows a representation of the metastability exchange collision. The result of the hyperfine interaction and the metastability exchange collisions in ^{3}He atoms is that the emerging ground-state atom has a polarised nucleus. It was found that the metastability exchange collision dominates the ground-state ^{3}He nuclear magnetic relaxation rate (T_1). This leads to the polarisation of the ground-state ^{3}He nuclei matching the degree of polarisation of the electronic spins of the metastable atoms.

4 MRI Pulse Sequences

4.1 Sequences for MRSolutions 0.15T Scanner

This section describes each sequence used on the 0.15T MRI scanner during the studies, and how the data collected from them are analysed. All of the sequences used in studies on the 0.15T MRI scanner were created to measure the diffusion constant of the ^{3}He gas, when inhaled by a volunteer, at different time scales. There are sequences written for the 0.15 T scanner that take images, but none were used in these studies, so will not be discussed here.

4.1.1 CPMG Sequence

The Carr-Purcell-Meiboom-Gill (CPMG) sequence, initially developed by Carr and Purcell, then added on to by Meiboom and Gill, is commonly employed to enhance the Signal to Noise ratio of a NMR spectrum. As seen in Fig.15, CPMG is a one-shot spin echo sequence, consisting of a non-selective 90° RF pulse, followed by an echo train, induced by successive non-selective 180° pulses. To suppress any effects of imperfections in the 180° pulses, the phase is switched by 180° for each successive 180° pulse. For diffusion weighting, gradients are added between each pulse (during acquisition), as shown in Figure 15.

Figure 15: Diagram of the CPMG sequence.

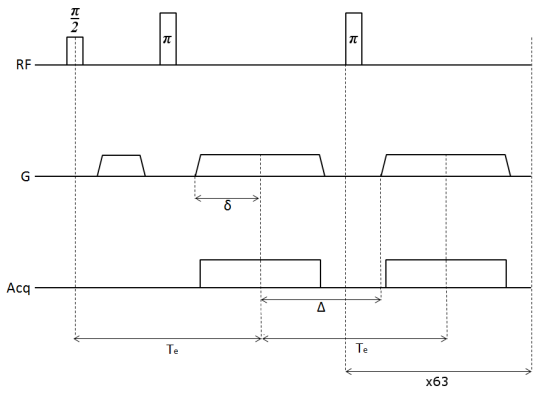

The signal intensity of the echo measured at each successive acquisition is attenuated by both diffusion of the target particles (denoted by D, the diffusion constant), and by the ratio of the Echo Time, T_E, and the T_2 time, according to:

$$\frac{S_n}{S_0} = e^{-n\,b\,D}\, e^{\frac{T_E}{T_2}} \tag{24}$$

where S_n is the signal intensity of the n^{th} echo, while S_0 is the signal intensity if there was no attenuation. The b represents the "b-value", a term expressing the amount of diffusion sensitivity applied by the gradients. The b-value is expressed as:

$$b = \gamma^2 G^2 \delta^2 (\Delta - \tfrac{\delta}{3}) \tag{25}$$

where γ is the gyromagnetic ratio, G is the strength of the applied gradient fields, δ is the length of the gradient lobe, and Δ is the time between the two lobes.

In all studies, this sequence was implement with the same settings: 64 echoes, 64 sampling points at 30 μs sample period, a T_E of 14 ms, a T_R of 4000 ms, a δ of 1 ms, a Δ of 13 ms, and a gradient strength of 2.23x10^{-5} T cm^{-1} such that the gradients corresponding to a total b-value of 0.29 s cm^2.

The T_2 relaxation of ^{3}He in the lung at 0.15T has been previously measured [97], and found to be 5 seconds. This means that the loss of signal due to diffusion is therefore much greater (by an order of magnitude) than that of the loss due to T_2 decay, such that the T_2 term in equation 24 can be ignored. So the equation becomes:

$$\frac{S_n}{S_0} = e^{-n\ b\ ADC} \tag{26}$$

where D has been replaced by ADC, the Apparent Diffusion Constant. By plotting the log of the normalised signal decay against acquisition number n, where the gradient is equal to $-bADC$, the ADC of ^{3}He in the subject's lung can be calculated. Fig.16 shows this analysis for 3 CPMG scans performed on the same volunteer.

As there was a gradient on during the acquisition of each echo, the data has been frequency encoded, meaning 1-dimensional information can be recovered, and hence the ADC at each x-axis point can be calculated. Fig. 17 shows an example of the 1D signal intensity profile gained from the first echo of a CPMG scan.

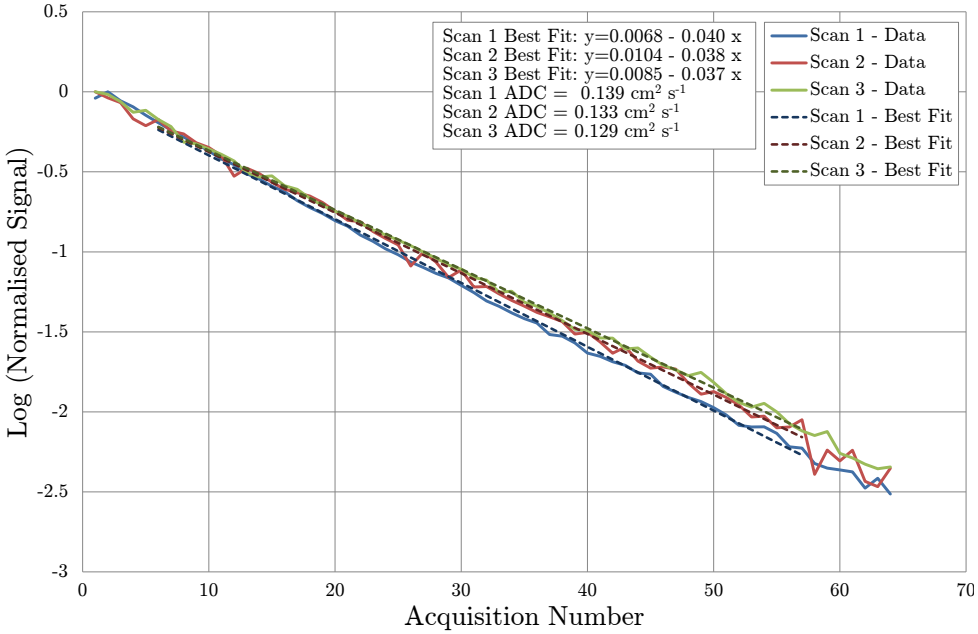

Figure 16: Analysis of 3 CPMG Scans Performed on an Asthmatic Volunteer

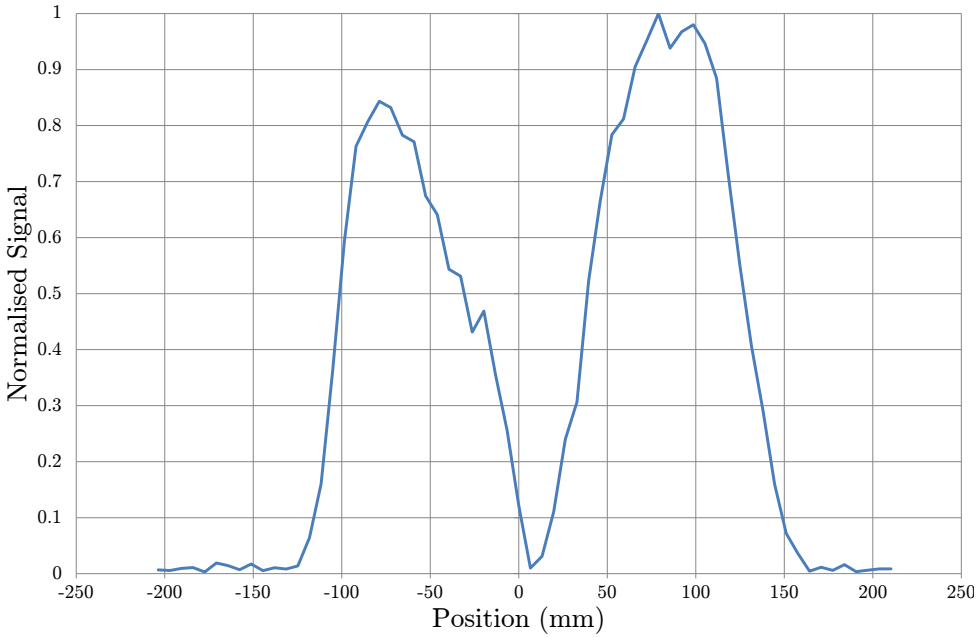

Figure 17: 1-Dimensional Profile of the Lungs

The data from each echo are transformed in this way, and the signal intensity decay at each point is used to calculate an ADC value (in the same manner as for the global value discussed before). Fig. 18 shows an example of the ADC profile this method produces.

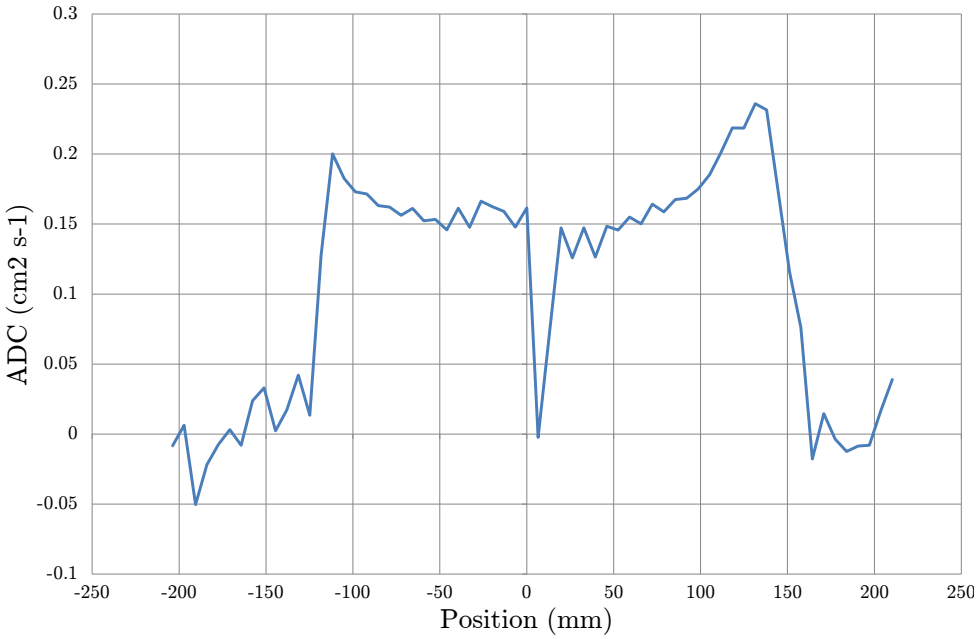

Figure 18: 1-Dimensional ADC Profile of the Lungs

From this, the ADC values are placed in a histogram, from which the mean ADC value can be calculated. To remove the ADC values that are not from the lungs, a second histogram is created which has the ADC values "weighted" by the original signal intensity at that 1D voxel. Fig. 19 shows a typical histogram produced from this technique.

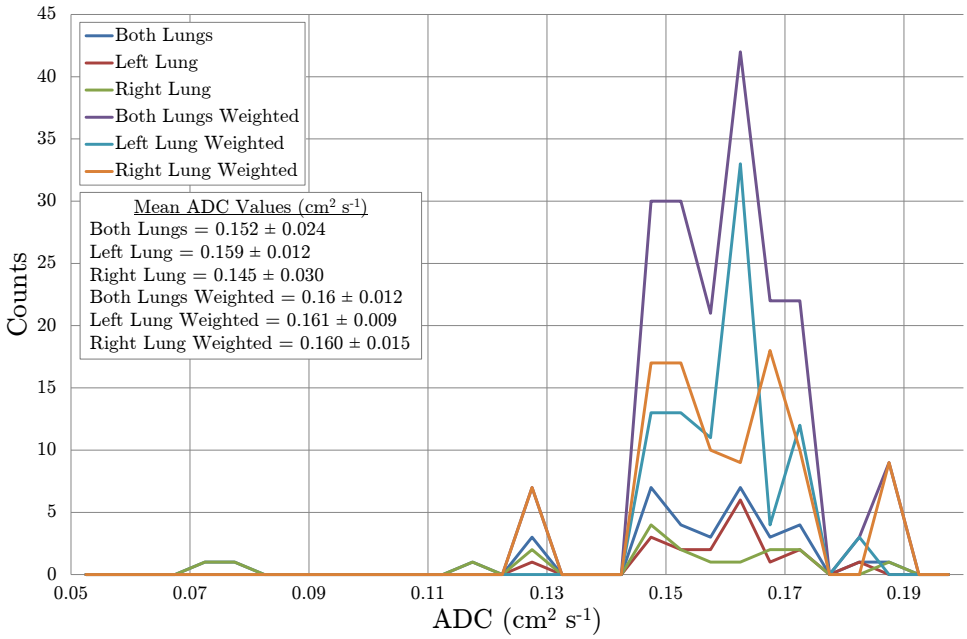

Figure 19: ADC Histogram, Showing Both Normal and Weighted Histograms

It has already been reported [98] that ADC at short-time scales has a strong positive correlation with the degree of lung inflation, such that a volume-correction must be applied to the ADC values calculated. Using the correction equation developed by Ball [4], we have that:

$$ADC = ADC_v + 0.36 * ADC_v * (\frac{V_B}{V_{FRC}}) \tag{27}$$

where ADC_v is the ADC before volume-correction, V_B is the volume of the bolus of ^{3}He/^{4}He inhaled by the subject, and V_{FRC} is the Functional Residual Capacity (volume of air remaining in the lungs at the end of a normal exhalation) volume of the subject. While performing this scan, the subject inhales in the bolus at FRC.

4.1.2 gADC Sequence

The global Apparent Diffusion Constant (gADC) sequence, as seen in Fig. 20, is a simple gradient echo sequence, using a low flip-angle (α) non-selective pulse, that is repeated 50 times. Out of the 50 acquisitions taken, 40 have diffusion weighting gradients applied, for the same duration, but with varying strengths. The other ten have no gradients applied, though still have the same T_E time.

Figure 20: Diagram of the gADC sequence.

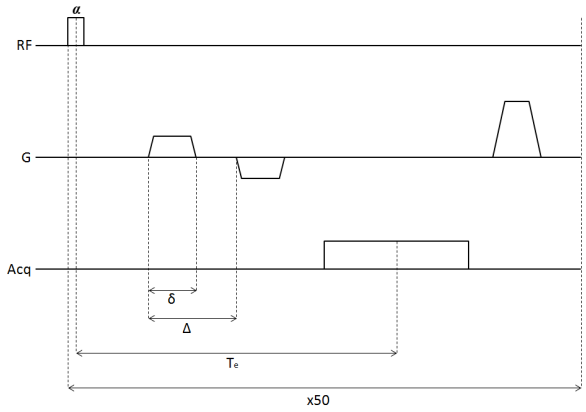

The 10 gradient free acquisitions occurred as every 5^{th} acquisition, to allow for correction against T_1 decay and RF depletion. The signal attenuation for the diffusion weighted acquisitions can be approximated as:

$$S_n = S_0 \, e^{\frac{-n\,T_R}{T_1}} \; e^{-b_n \, ADC} \; cos^n(\alpha) \tag{28}$$

where S_n is the signal intensity for acquisition number n (starting at n=0), S_0 is the signal intensity of the n=0 acquisition, T_R is the repetition time, α is the flip angle of the RF pulse, ADC is the Apparent Diffusion Constant,

and b_n represents the "b-value", a term expressing the amount of diffusion sensitivity applied by the gradients for the n^{th} acquisition. The b_n-value for this sequence is expressed as:

$$b_n = \gamma^2 G_n^2 \left[\delta^2 \left(\Delta - \tfrac{\delta}{3} \right) + \tau \left(\delta^2 - 2\Delta\delta + \Delta\tau - \tfrac{7}{6}\delta\tau + \tfrac{8}{15}\tau^2 \right) \right] \qquad (29)$$

(from [108]), where γ is the gyromagnetic ratio, G is the strength of the applied gradient fields, δ is the length of the gradient lobe, and Δ is the time between the two lobes, and τ is the ramp time of the diffusion weighting gradients. This equation differs from that of equation 25, as it contains an extra term to correct for trapezoidal shaped gradients.

In the Leicester Royal Infirmary Cystic Fibrosis study, this sequence was implemented with the following settings: 50 repetitions, 2048 sampling points at 80 μs sample period, a T_E of 11 ms, a T_R of 200 ms, a δ of 4.4 ms, excluding the ramp time of 150 μs on each side of the gradient, and a Δ of 5.2 ms. The b_n-value for each acquisition varies due to the different gradient strengths, with a maximum value of b= $\sim$56 s cm^2.

As the typical T_R for this sequence was 200 ms, and the T_1 was assumed to be $\sim$25 s, so the T_1 term can be ignored, simplifying equation 28 to:

$$S_n = S_0 \, e^{-b \, ADC} cos^n(\alpha), \qquad (30)$$

and when the b_n-value equals 0, i.e. for the 10 acquisitions that lack gradients, equation 28 simplifies to:

$$S_n = S_0 cos^n \alpha. \qquad (31)$$

If the line $y = mc^{x-1}$ is fitted to the 10 "calibration" acquisitions, the equation $S = S/c^{(x-1)}$ can be used to correct the diffusion weighted decay data, leaving only the attenuation due to diffusion. Fig. 21 shows the diffusion decay of a typical scan, alongside the 'calibration' decay, and the best-fit line $y = mc^{x-1}$.

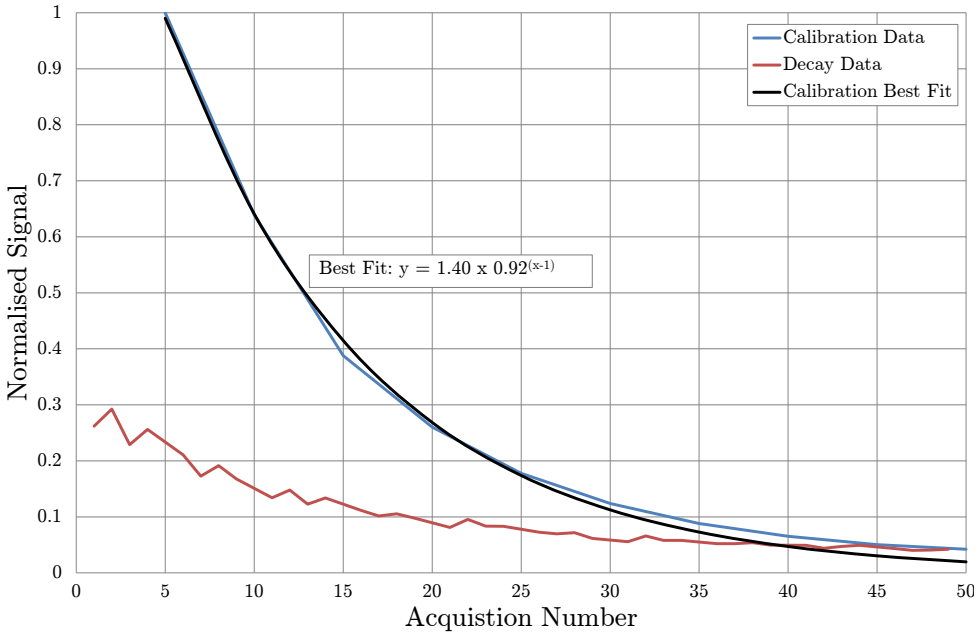

Figure 21: gADC Signal Decay Plot

Once corrected, the signal intensity is plotted against its corresponding b_n-value. To this the Yablonskiy Model [109] can be fitted, which returns the parameters R (the radius of the alveoli duct) and h (the width of the alveoli sac). Fig. 22 shows a typical b-space plot, along with a Yablonskiy fitting.

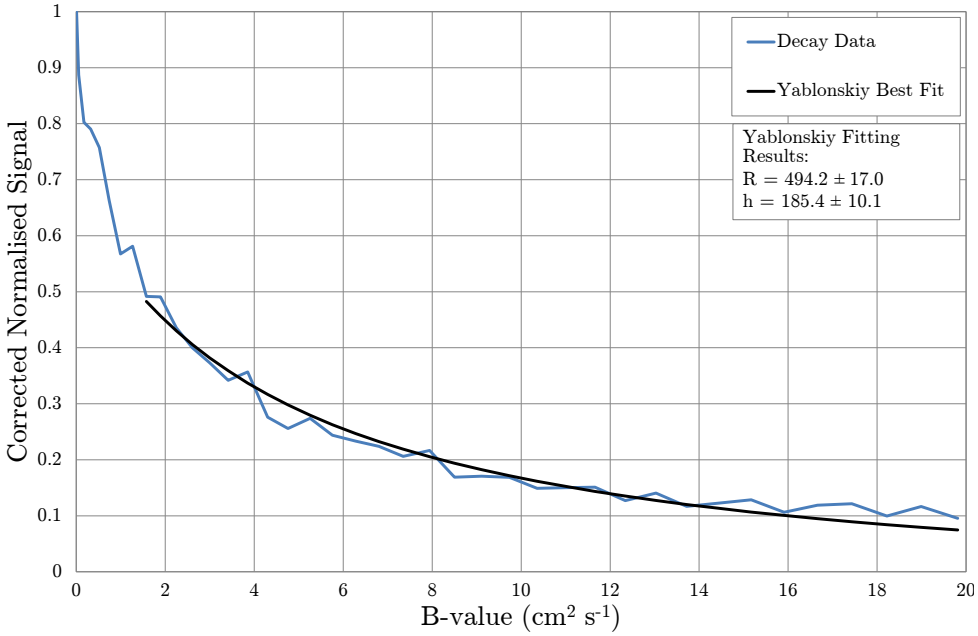

Figure 22: B-Space Plot with Yablonskiy Model Fitting

4.1.3 STE Sequence

The STimulated Echo (STE) sequence, as seen in Fig. 23, consists of 5 non-selective small flip angle (α) pulses and acquisitions (known as the calibration stage). This is then followed by the set-up stage, consisting of a non-selective 90° pulse, a diffusion weighting gradient, another non-selective 90° pulse, and then a crusher gradient. This is followed by the read out stage, which consists of 45 non-selective α pulses followed by acquisitions with refocus diffusion weighting gradients and then crusher gradients. This sequence is similar to the global STE sequence described by Wang et al [94].

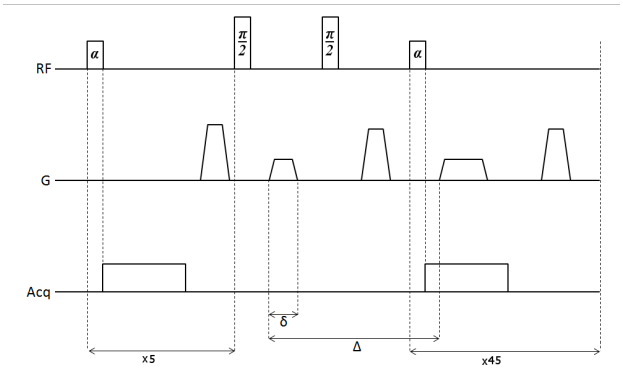

Figure 23: Diagram of the STE sequence.

The calibration stage is a simple pulse and FID acquisition, with the flip angle of the pulse, and the repetition time T_R, matching that of the read out stage. The signal intensity of the calibration stage is attenuated according to:

$$S_n = S_0 \, sin(\alpha) \, [\, cos(\alpha) \, e^{\frac{-T_R}{T_1}} \,]^{n-1} \tag{32}$$

where α is the flip angle of the RF pulse, S_n is the signal intensity of the n^{th} acquisition, and S_0 is the original signal intensity if no attenuation was present.

In all studies, this sequence was implement with the same settings: A low flip angle α of 5°, 1024 sampling points at 20 μs sample period, a δ of 2.2 ms, and a gradient strength of 3.708x10^{-6} T cm^{-1}. Each calibration and read out section lasted 150ms each, with the time between the two $\pi/2$ pulse as 12ms and the time between the last $\pi/2$ pulse and the start of the first read out section 18ms.

As the typical T_R for this sequence was 150 ms, and the T_1 is assumed to be ∼25 s, meaning the T_1 term can be ignored, such that equation 32 can be simplified to:

$$S_n = S_0 \, sin\alpha \, cos^{n-1}(\alpha) \tag{33}$$

The set-up block consists of two 90° pulses, between which is a single diffusion weighting gradient. The read block consists of a small pulse (matching that of the calibration stage), followed by an acquisition with a diffusion sensitising gradient, during which an echo is formed. The signal intensity of the echo formed in the read out block attenuates according to:

$$S_n = \tfrac{1}{2} \, S_0 \, sin^2(90) \, sin(\alpha) \left[\, cos(\alpha) \, e^{\frac{-T_R}{T_1}} \, \right]^{N_C} \left[\, cos(\alpha) \, e^{\frac{-T_R}{T_1}} \right]^{n-1} e^{-b_n \, ADC_n} \tag{34}$$

where N_C is the number of repetitions in the calibration stage, S_0 is the original signal intensity if no attenuation was present, S_n is the signal intensity of the n^{th} read out block acquisition, and ADC_n is the Apparent Diffusion

Constant for the n^{th} acquisition, for the time-scale as measured between the dephasing gradient following the first 90° rf pulse in the set-up stage and the rephasing gradient of the n^{th} read out acquisition. As for equation 32, this can be simplified to:

$$S_n = \frac{1}{2}\, S_0\, sin^2(90)\, sin(\alpha)\, cos(\alpha)^{N_C+n-1}\, e^{-b_n\, ADC_n} \tag{35}$$

So from fitting the equation $y = m\ cos(c)^{x-1}$ to the calibration stage FIDs, and then using the result to apply the equation $S_n = \dfrac{2S_0}{sin^2(90)\ m\ cos^{N_c+n-1}(c)}$ to the read out stage echoes, meaning that all that is left is the attenuation due to diffusion at each acquisition point ($S_n = e^{-b_n\ ADC_n}$). Fig. 24 shows the attenuation of the calibration FIDs, and read out echoes, along with the fitted line and "corrected" values.

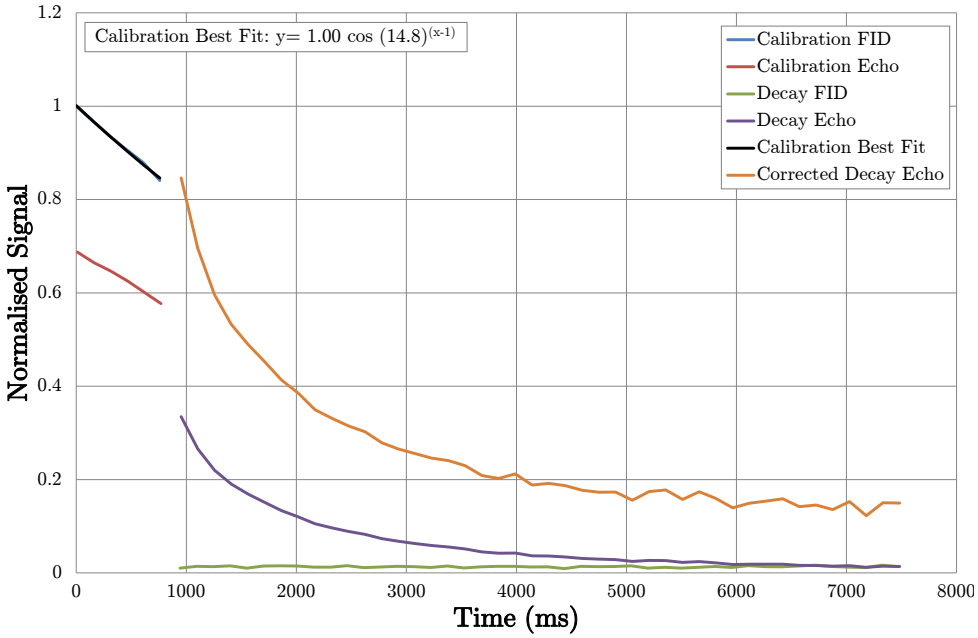

Figure 24: Signal Intensity of the STE Acquisitions Against Time

From this the Apparent Diffusion Constant (ADC) at each read out acquisition can be calculated using:

$$ADC_n = \frac{-ln(S_n)}{b_n} \tag{36}$$

where b_n represents the 'b_n-value', a term expressing the amount of diffusion sensitivity applied by the gradients, depending on the gradient strength and period. b_n is expressed as:

$$b = \gamma^2 G^2 \delta^2 \left[\left(\Delta_n - \tfrac{\delta}{3} \right) + \tau \left(\delta^2 - 2\Delta_n \delta + \Delta_n \tau - \tfrac{7}{6}\delta\tau + \tfrac{8}{15}\tau^2 \right) \right] \tag{37}$$

where γ is the gyromagnetic ratio, G is the strength of the applied gradient fields, τ is the ramp time of the diffusion weighting gradients, δ is the length of the diffusion sensitising gradient in the set up stage, and Δ_n is the time between the diffusion sensitising gradient in the set up stage and the diffusion sensitising gradient in the n^th read out acquisition.

This means that the ADC for various diffusion time lengths can be recovered from a single scan. Fig. 25 shows a typical result from a single scan on a volunteer.

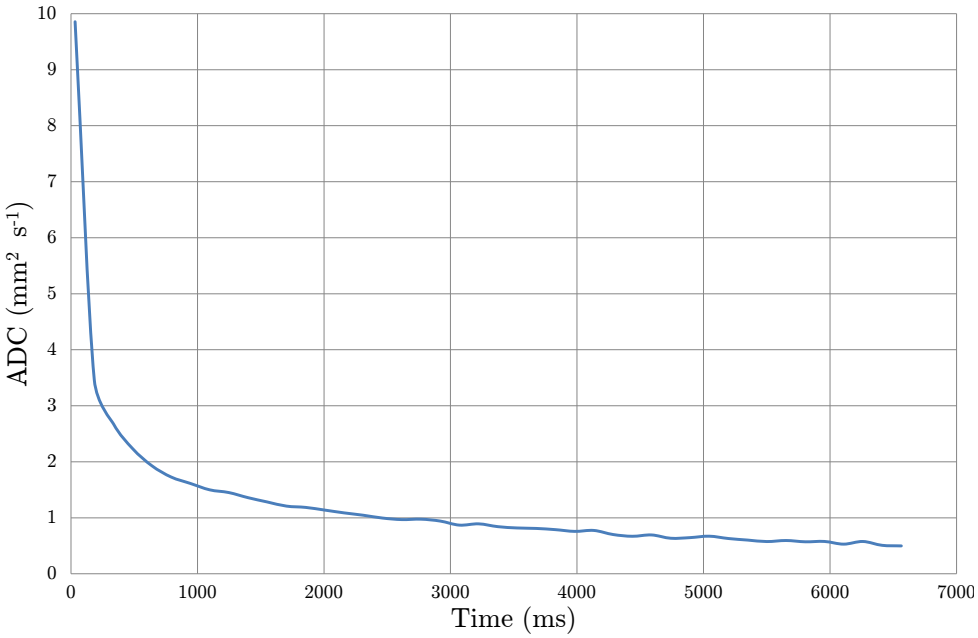

Figure 25: A Typical Plot of the Measured ADC Against Time

4.2 Sequences for GE 1.5T Scanner

This section describes each sequence used on the 1.5T GE MRI scanner during this study. There are many GE certified proton sequences available on the 1.5T scanner, but for use with ^{129}Xe, broad-banded non-GE sequences are required as well (known as 'site' sequences). Both the GE proton sequences and the broad-banded ^{129}Xe site sequences are discussed, with a final discussion on the safety of the sequences.

4.2.1 GE Sequence: 3-Plane Localiser

The 3-Plane localiser is a GE certified clinical sequence by GE, primarily used to locate the target for following scans, so that they can be correctly positioned.

The 3-Plane localiser sequence is a T_E optimised gradient echo sequence (as seen in Fig. 26) with a selective RF pulse (whose flip angle (α) can be set per scan), that is repeated (at the same phase encoding step) for each slice (in one direction) inside a single T_R, before repeating as needed for phase encoding. 5-6 slices are taken, in all 3 directions (Axial, Sagittal and Coronal). When being used for co-registration for Xenon (meaning that the RAPID coil is inside the scanner) a low SAR version is used, where the T_R time is increased, and the pulse flip angle reduced such that there is no risk of damage to the RAPID coil.

Figure 26: Diagram of the 3-Plane Localiser sequence.

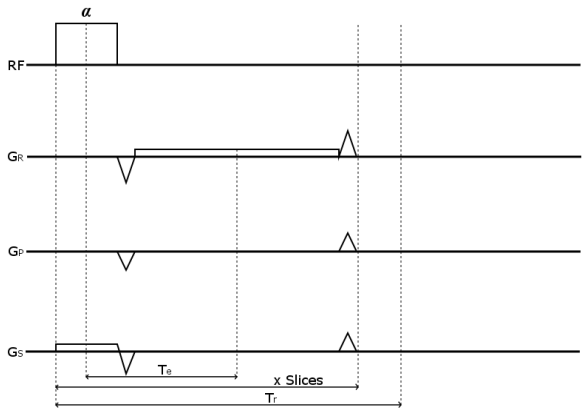

The data can then be reconstructed into an image, by either the on-board GE reconstruction engine, or elsewhere using the program 'RECON' (see Section 4.3).

4.2.2 GE Sequence: T_2 Prepared SSFSE

The T_2 prepared SSFSE sequence is a certified clinical sequence by GE. It consists of a single shot spin echo routine with selective pulses (the initial α pulse flip angle can be set before each scan), executed at the fastest speed (i.e. shortest T_e) that the system can perform. To give T_2 weighting, a number of echoes are ignored at the beginning to simulate a long initial T_e time (known as T_e effective).

By performing multiple scans, with varying T_e effective times, the T_2 of the sample can be calculated at each pixel. The signal intensity for scan is described by:

$$S_n = S_0 e^{-\frac{T_e}{T_2}} \tag{38}$$

Figure 27: Diagram of the T_2 Prepared SSFSE sequence.

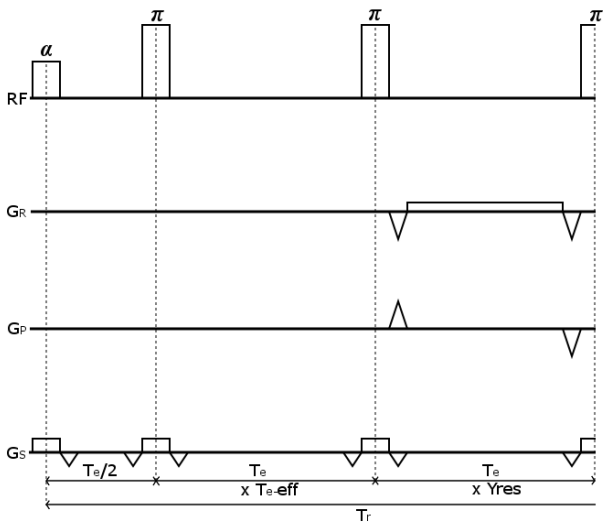

where T_e is the effective T_e for scan n, S_n is the Signal intensity for scan n, S_0 is the signal intensity for a scan with an effective T_e of 0. However, this does not account for noise. Adding a noise term (N), gives:

$$S_n = \sqrt{(S_0 e^{-\frac{T_e}{T_2}})^2 + N^2} \tag{39}$$

Using this equation, the T_2 for each pixel of the scans can be calculated, creating a T_2 map, once the data have been reconstructed into 2D images. This can be performed by using the program 'RECON' (see Section 4.3).

4.2.3 GE Sequence: Inversion Recovery SSFSE

The inversion recovery SSFSE sequence is a certified clinical sequence by GE. It consists of a single shot spin echo routine with selective pulses (the α pulse flip angle can be set before each scan), executed at the fastest speed (i.e. shortest T_e) that the system can perform. To give T_1 weighting, an initial 180° pulse is used, followed by a delay T_i, before the standard T_2

prepared SSFSE is performed (where echoes are ignored at the beginning to simulate a long initial T_e time (known as T_e effective)).

Figure 28: Diagram of the Inversion Recovery SSFSE sequence.

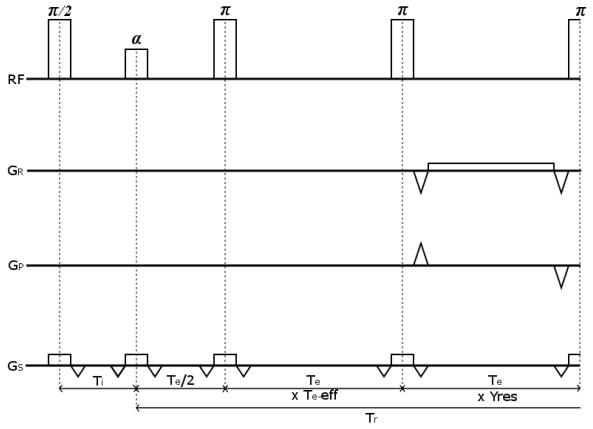

By performing multiple scans, with varying T_i times, the T_1 of the sample can be calculated at each pixel. The signal intensity for scan is described by:

$$S_n = S_0 - 2S_0 e^{-\frac{T_i}{T_1}} \tag{40}$$

However, this does not account for noise. Adding a noise term gives:

$$S_n = \sqrt{(S_0 - 2S_0 e^{-\frac{T_i}{T_1}})^2 + N^2} \tag{41}$$

Using this equation, the T_2 for each pixel of the scans can be calculated, creating a T_1 map, once the data have been reconstructed into 2D images. This can be performed by using the program 'RECON' (see Section 4.3).

4.2.4 Site Sequence: bb2dfast

The bb2dfast sequence was created at the University of Sheffield, and is a broad-banded version of the GE certified 2dfast sequence. The 2dfast sequence is a gradient echo sequence using a selective RF pulse (whose flip angle (α) can be set before each scan), that has been optimised to improve acquisition time. Fig. 29 shows a single acquisition of the bb2dfast sequence. The gradients are mostly played out in a triangular shape (except where required to be a plateau for slice selecting or frequency encoding). The acquisitions are then repeated as many times as are needed for phase encoding, and then the sequence is repeated as many times as needed to acquire all slices and images. Sometimes the slices are interleaved, taking one acquisition of each slice (at the same phase encode step) within a single T_R.

Figure 29: Diagram of the bb2dfast sequence.

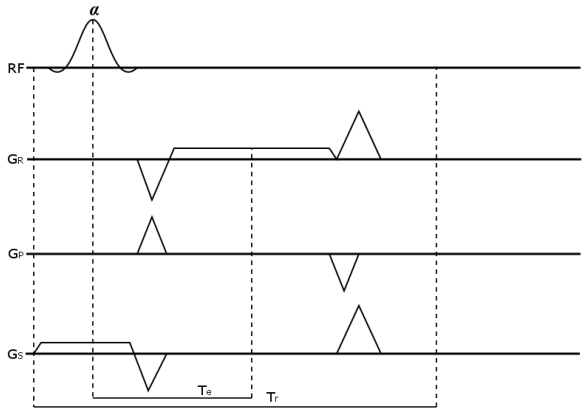

The data can then be reconstructed into an image, by either the on-board GE reconstruction engine, or elsewhere using the program 'RECON' (see Section 4.3).

4.2.5 Site Sequence: bbfgre

After the scanner console was updated from EPIC version 14M5 to 16, the existing site sequence, bb2dfast, could no longer be used. Instead a new sequence was created, by broad-banding the GE certified fgre sequence. Like the 2dfast sequence, the fgre is also a gradient echo sequence using a selective RF pulse (whose flip angle (α) can be set before each scan), with a few slight differences, mainly in the setup options. The bbfgre sequence was created in house at the University of Nottingham. Fig. 30 shows a single acquisition of the bbfgre sequence. As with the bb2dfast, the gradients are mostly played out in a triangular shape (except where required to be a plateau for slice selecting or frequency encoding). The acquisitions are then repeated as many times as are needed for phase encoding, and then the sequence is repeated as many times as needed to acquire all slices and images. Sometimes the slices are interleaved, taking one acquisition of each slice (at the same phase encode step) within a single T_R.

One of the prime reasons for broad-banding the fgre sequence over the 2dfast sequence was the larger amount of setup options available. One such setup options is the phase-encoding method, which was permanently set to sequential only on the 2dfast sequence, where-as the fgre provides multiple options, such as centre-out. Another setup option of interest was the minimum frequency/phase resolution, which with the 2dfast was 128x128,

Figure 30: Diagram of the bbfgre sequence.

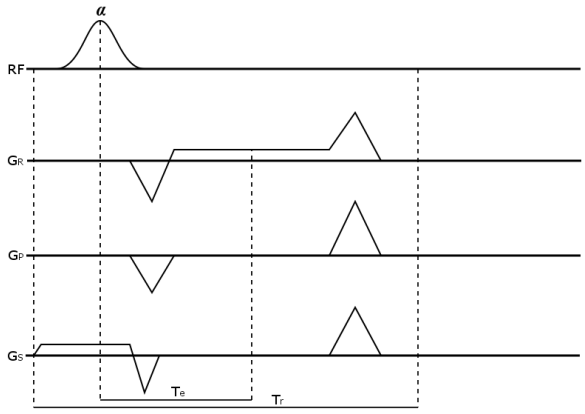

whereas the fgre sequence allowed resolutions down to 64x64.

As with bb2dfast, the data can then be reconstructed into an image, by either the onboard GE reconstruction engine, or elsewhere using the program 'RECON' (see Section 4.3).

4.2.6 Safety - Site Sequence Code Review

To ensure that the Site sequences are safe for use on human volunteers (along with the non-GE ^{129}Xe RAPID Coil) the sequences must be checked, and SAR levels measured experimentally.

In EPIC programming, SAR estimations are performed by converting the RF pulses into an equivalent number of 'standard' RF pulses, and then entering them into the following equation:

$$Average\,SAR = \frac{\left(\begin{matrix}No.\,of\,'standard'\,RF\\ pulses\,in\,sequence\end{matrix}\right) \times \left(\begin{matrix}Energy\,deposited\,by\\ 'standard'\,RF\,pulse\end{matrix}\right)}{(Sequence\,repetition\,time) \times (Patient\,weight)} \tag{42}$$

The estimated energy deposited by a standard pulse into a patient is a function of patient's weight, strength of the B_0 field, and the coil used. GE have determined this experimentally, by scanning patients of various weights and sizes, at different field strengths. These estimates have then been stored in the code file 'peakrf.c' It uses just one set of equations for both PSD_BODY (the *opcoil* value of the main BODY coil), and $PSD\_SURFACE$ (the *opcoil* value of the ^{129}Xe RAPID Coil). This is where an error in the SAR calculations can arise, as the SAR equation will not take into account the characteristics (such as close proximity) of the coil.

To convert a single RF pulse into Standard Pulses, the peak B_1 of the RF pulse, as it is played out in the sequence, is calculated using the following equation:

$$peak\, B_1 \;=\; max\_b1 \;\times\; \frac{nom\_pw}{pw} \;\times\; \frac{act\_fa}{nom\_fa}\,, \tag{43}$$

where nom_pw is the nominal pulse width (the time the pulse is played out for, which may or may not be the same as the actual pulse width of the pulse), nom_fa is the nominal flip angle (the flip angle the pulse delivers if its actual pulse wdith was nom_pw and its peak B_1 was at the maximum), max_b1 is the peak pulse amplitude (if the RF pulse width was nom_pw and the desired flip angle was nom_fa). pw is the actual pulse width as played out in the sequence, and act_fa is the actual flip angle of the pulse as it is implemented.

Now that the peak B_1 has been calculated, the number of Standard Pulses per sequence can be calculated using:

$$\#\,Std.\,Pulses = num \times effwidth \times \frac{pw}{std.pulse's\,width} \times \frac{peak\,B_1}{std.\,pulse's\,B_1}\,. \tag{44}$$

where num is the number of times the actual pulse is used in the sequence, and $effwidth$ is the effective pulse width (an integral of the pulse amplitude squared, divided by the width of the pulse, mad on normalized pulses). $effwidth$ is used to compare energies of RF pulses of differing shape.

Although the SAR calculation in itself is not too complex, it is important that the sequence code implement pulses consistently with the parameters that are used in the SAR calculations. If one is modifying a product sequence code, it is important that the arguments to the *powermon_b1scale()* function are correct, as within this internal function is where the SAR calculations are performed, and that fields in the $rfpulse$ structure are filled in correctly for any new RF pulses either in the sequence code or in the 'grad_rf_ <psdname>.h file'. Thus, in modifying a product sequence code, it is not hard to ensure that the SAR calculations are correct.

This was confirmed by a review of both the bb2dfast and bbfgre code, where it was found that the *powermon_b1scale* routine inputs were still as they were in the original GE source code they were based on, and that all the important variables that the SAR calculations used were still initialised and used correctly. To further review the sequences, an oscilloscope was attached to the X, Y and Z gradient outputs, as well as the RF pulse output. Then each sequence was played out, using a variety of settings, monitoring the

results on the oscilloscope each time. It was found that for every setting used the gradients and RF pulses played out as expected, occurring at the correct time and for the correct length and power, for both Proton and Xenon modes. This strongly implies that the source codes were implemented correctly.

4.2.7 Safety - SAR Experiments

After reviewing the sequences, the max SAR of the sequence, when used with the ^{129}Xe RAPID Coil, must be checked experimentally.

The specific absorption rate (SAR) can be measured physically by monitoring the temperature change of a phantom subjected to the sequence over time. The equation for calculating the SAR (in Wkg^{-1}) is:

$$SAR = \frac{C \times \Delta T}{t}, \tag{45}$$

where C is the specific heat capacity of the phantom ($JK^{-1}kg^{-1}$), ΔT is the measured change in temperature (K), and t is the exposure time (s).

For the SAR tests, 1 L Saline bags were used as the target phantom/s, which consisted of 0.9% Sodium Chloride by volume. At this low concentration of Sodium Chloride, the specific heat capacity can be assumed to be the same as that for pure water (4181 $JK^{-1}kg^{-1}$). SAR tests were run using the BODY coil with a GE standard Fast Spin Echo sequence (called FSE-XL on the scanner) for a proof of concept test, and then at both Xenon and Proton frequencies for the bb2dfast sequence and at Xenon frequencies only for the bbfgre sequence, using the BODY coil for the Proton frequency

runs and the RAPID coil for the Xenon frequency runs. For the BODY coil tests one or two phantoms were used, positioned on the center of the bed. For the bb2dfast/bbfgre Xenon frequency tests the RAPID coil was filled with 20 bags, so that the minimum loading of 20 kg required by the coil was achieved. During each test run, the before and after temperature of one or more bags were measured. Control bag/s were also measured alongside the test bag/s, and left on the bed just outside the scanner bore during scanning. This was done to ensure that any temperature change measured in the test bag/s subjected to the scan were not due to temperature fluctuations in the room.

The temperature measurements were performed immediately before and after the scans, using a Quartz Digi-Thermo thermometer. For each measurement the probe of the thermometer was inserted into the Saline bags through a valve, and left for a minute for the temperature reading to stabilise, before being removed and the valve resealed. The Digi-Thermo thermometer resolution is 0.1°C. The value used in SAR calculations is the change in temperature of the test bag (ΔT_P), minus the change in temperature of the control bag (ΔT_C).

As can be seen in the results table (Table 3), the Proton frequency tests showed a measurable but small increase of temperature over the control phantom, and the calculated SAR value is similar to that which was estimated by the scanner for the sequence. For the protocols of the scans used, see A.1. The temperature increase for the first few bb2dfast scans matches those of equivalent FSE-XL sequences with the same Est. SAR value, however the latter bb2dfast scans see a greater temperature increase.

These scans were performed later in the day, after long periods of MRI use. It may be that constant use of the MRI scanner lead to a slight warming of the bore of the MRI scanner compared to the rest of the room.

Table 3: Proton Test Results

Sequence	Protocol	ΔT_P (K)	ΔT_C (K)	t (s)	Calc. SAR (W kg^{-1})	Est. SAR (W kg^{-1})
FSE-XL	2	0.7	0.0	2570	1.14	1.4
FSE-XL	1	0.5	-0.1	2980	0.84	0.9
FSE-XL	3	0.8	0.1	2567	1.14	1.7
FSE-XL	3	0.9	0.0	2567	1.47	1.7
FSE-XL	3	0.8	0.0	2567	1.30	1.7
bb2dfast	4	0.8	-0.2	2595	1.61	1.7
bb2dfast	4	0.8	-0.2	2595	1.61	1.7
bb2dfast	4	1.7	-0.2	2595	3.06	1.7
bb2dfast	4	1.9	-0.2	2595	3.38	1.7
bb2dfast	6	1.6	-0.1	2595	2.74	1.7
bb2dfast	6	1.3	-0.1	2595	2.26	1.7

For the Xenon frequency tests on bb2dfast and bbfgre, multiple positions inside the RAPID coil were tested, to check for localised heating effects. Fig. 31 shows the positions of the phantoms measured. For the protocols of the scans used, see A.2. As the only concern is the emitted RF, the upper receive coil was not used during the scans to allow closer access to the upper transmit coil.

When running the bb2dfast and bbfgre sequences, it was apparent that when the target nuclei was changed from ^{1}H to ^{129}Xe, the Estimated SAR reduced by a factor of $\sim$16, which is similar to the expected change, as the RF frequency required for ^{129}Xe is 4 times lower than that needed for proton, and as RF power has a square relationship to frequency, this would

Figure 31: Positions of the Phantoms Measured.

Positions of phantoms (1-7) inside RAPID Coil, with the control (C) on the bed outside the scanner.

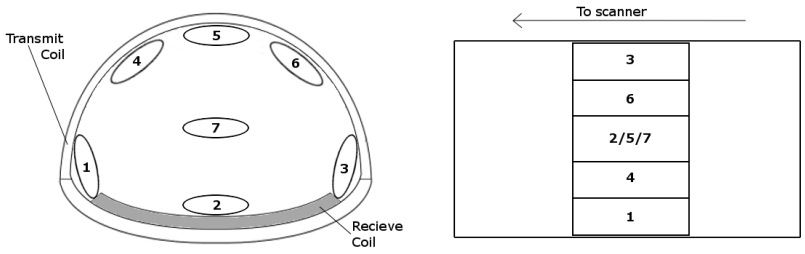

(a) Axial Cross-Section View. (b) Top Down View.

mean about 16 times less RF power for ^{129}Xe than for proton. However it should be noted that the SAR calculations do not change when swapped from BODY to RAPID coil, as it does not have the knowledge of the specifics of the RAPID coil.

As can be seen in the results table (Table 4), there was a measurable increase of temperature in some of the bags. Mostly the temperature increase is negligible, or is likely due to slightly more RF intense local zones. Most of the higher temperature increases (0.5-0.7°C) were seen in tests that had been performed later in the day, after many previous tests. It was noticed that after such long use the outer shell of the RAPID coil was slightly warm to the touch. Hence some of the heating may be accredited to the heating of the internal circuitry of the RAPID emit coil as opposed to being purely due to absorption of the emitted RF. However the coil was not excessively warm, so contact burns were not considered a risk. However, the temperature increases involved never reached those of the High SAR level Proton scans. This implies that the bb2dfast/bbfgre sequences and RAPID coil are safe to use on patients, especially when it is remembered that to get

these temperatures the scan ran for over 40 minutes with a high flip angle of 45°, whereas on a human subject it will be ran for no more than 20 seconds (a breath hold), and often with a much lower flip angle.

Table 4: bb2dfast/bbfgre Xenon Test Results

Sequence	Position	Protocol	ΔT_P (K)	ΔT_C (K)	t (s)	Calc. SAR (W kg^{-1})	Est. SAR (W kg^{-1})
bb2dfast	2	1	0.0	-0.1	2411	0.17	0.0
bb2dfast	1	1	0.4	0.1	2411	0.52	0.0
bb2dfast	3	1	0.3	-0.1	2411	0.69	0.0
bb2dfast	5	1	0.5	0.5	2411	0.00	0.0
bb2dfast	6	1	0.5	0.0	2411	0.87	0.0
bb2dfast	7	1	0.3	0.0	2411	0.52	0.0
bb2dfast	2	1	-0.1	0.0	2411	-0.17	0.0
bb2dfast	1	1	0.0	0.0	2411	0.00	0.0
bb2dfast	3	1	0.1	0.0	2411	0.17	0.0
bb2dfast	4	1	0.0	-0.1	2411	0.17	0.0
bb2dfast	6	1	0.1	-0.1	2411	0.35	0.0
bb2dfast	7	1	0.3	-0.1	2411	0.69	0.0
bb2dfast	2	2	0.5	-0.1	2411	1.04	0.1
bb2dfast	1	2	0.7	-0.1	2411	1.39	0.1
bb2dfast	3	2	0.7	-0.1	2411	1.39	0.1
bb2dfast	4	2	0.6	0.0	2411	1.04	0.1
bb2dfast	6	2	0.6	0.0	2411	1.04	0.1
bb2dfast	7	2	0.3	0.0	2411	0.52	0.1
bbfgre	1	3	0.2	-1.5	2940	0.57	0.0
bbfgre	2	3	0.1	-1.5	2940	0.43	0.0
bbfgre	3	3	0.2	-1.5	2940	0.57	0.0
bbfgre	4	3	0.2	-1.5	2940	0.57	0.0
bbfgre	5	3	0.1	-1.5	2760	0.45	0.0
bbfgre	6	3	0.0	-1.5	2760	0.30	0.0
bbfgre	7	3	0.2	-1.5	2760	0.61	0.0
bbfgre	4	4	0.0	0.0	1440	0.00	0.0
bbfgre	2	4	0.0	0.0	1440	0.00	0.0
bbfgre	6	4	0.2	0.0	1440	0.58	0.0
bbfgre	7	4	0.0	0.0	1440	0.00	0.0

4.2.8 Safety - Conclusion

The review of the codes, along with the knowledge of how EPIC sequence codes perform their safety checks, shows that both codes appear to perform the SAR calculations correctly, except for an estimation of the specific coil used. This discrepancy is the most likely cause of any difference between the estimated SAR and that measured in the SAR tests. This discrepancy must be kept in mind when using this sequence with any non-GE coil.

The SAR tests show that there is a higher than estimated heating effect when using the ^{129}Xe coil, but that it is still well below safe limits even with RF rich versions of the both Site sequences. If other sequences are to be used on this coil, it is highly recommended that SAR tests are performed to confirm their actual max SAR, as was done with bb2dfast and bbfgre, before use on human volunteers.

In conclusion the sequences bb2dfast and bbfgre were deemed safe for use on human volunteers with all GE coils, and the ^{129}Xe RAPID Coil.

4.3 Image Reconstruction

Both the 0.15T and 1.5T MRI systems have an array of imaging sequences, which may be used during test runs and studies. Although they both have in-built image reconstruction, there is little to no control on how the final image looks, and much of the raw data is lost as the image can only be saved in traditional image formats (.JPG, DICOM). Hence it is important that the raw data files from both platforms can be read, interpreted and reconstructed elsewhere, with greater user control and keeping all data intact for any further analysis that may be desired.

In response to this need, the multi-platform Graphical User Interface program called 'RECON' was created, alongside a secondary command-line based streamlined version called 'RECONlite'. Both programs provide image reconstruction from raw data files produced by either MRI scanner, with options to save the raw data, reconstructed data, and header information in ASCII text file format, as well as saving the reconstructed image in traditional image formats (.PNG,.BMP). On top of this, 'RECON' has a plethora of extra features, such as white balance, 3D modeller, multi-file reconstruction, T1 and T2 map analysis, ADC map analysis and image masking analysis. The following is a brief review of the features of the programs, and how they work.

4.3.1 Raw Data File Interpretation

The single most important part of both programs is to be able to interpret both MRI scanners raw data files. Both the raw image data and any header/footer information containing scan details must be recovered, as both are required for full reconstruction and analysis.

For the 0.15T MRSolutions console, the raw data is saved to a '.MRD' file. As can be seen in Table 5, the file is split into 3 main sections: Header, Data and Footer. The header section contains the main key values, required to interpret the data section, such as x/y/z/d/e dimensions, and the data type (short/long int, float, double, complex, etc.). The data section contains the actually raw data from the scan, in 'datatype' format, ordered by x, y, z, d then e blocks. Immediately following the data section is the footer. The footer contains all the settings used in the scan sequence, in ASCII char format. It can be variable in length, as the number of user-editable variables in a sequence can vary. Each variable in the footer starts with a ':', followed by the variable name (e.g. 'PPL'), then a space, then 1 or more values separated by ', ' (e.g. 'C:\SEQUENCES\FGRE.PPL'). If the variable name is 'VAR', it represents a non-standard variable, and the first value following it is the name given to it in the source code (e.g. ':VAR read_lobe, 100').

The raw data on the 1.5T GE scanner is saved into as a binary 'P-file', which has the file name P#####.7, where the ##### is a 5 digit number representing the run number of the scan. Sometimes longer scans of multiple phases or slices are split into multiple P-files, with incrementing numbers. Table 6 shows the structure of a P-file. It consists of two main

Table 5: Structure of a .MRD raw data file

Section	Data Name	Data Type	Size (bytes)
Header 512 bytes	X size	long int	4
	Y size	long int	4
	Z size	long int	4
	D size	long int	4
	padding	short int	2
	datatype	short int	2
	padding	long int x7	28
	scaling	float	4
	padding	long int x14	56
	bitsperpixel	char	1
	padding	char x3	3
	padding	long int x10	40
	E size	long int	4
	padding	long int x25	100
	text	char x256	256
Data ? bytes	Image data	Dependant on 'datatype'	Xsize x Ysize x Zsize x Dsize x Esize x 'datatype'
Footer ?	Footer data	char x?	Variable

sections, the header and the data. The header in a P-file contains a lot more information than the .MRD files, a reflection on the vastly more complicated sequence source codes used by the GE system. The header section is split into 11 sub-sections, each containing information on different settings used in the scan. Immediately following the header section is the image Data. It can be correctly interpreted according to values given in the header sections (such as x-resolution, y-resolution, data-type, etc.)

Table 6: Structure of a P#####.7 raw data file (version 14.3)

Section	Sub Section	Description	Start byte	Size (bytes)
Header	rdb_hdr	Database Header	0	2048
	perpass_hdr	Per Pass Header	2048	16384
	uraw_hdr	Unlock Raw Header	18432	16384
	data_hdr	Data Header	34816	98304
	nex_hdr	NEX Header	133120	2052
	nexabort_hdr	Nex Abort Header	135172	2052
	tool_hdr	Tool Header	137224	2048
	ps_hdr	PS Header	139272	1500
	exam_hdr	Exam Header	140772	1040
	series_hdr	Series Header	141812	2048
	image_hdr	Image Header	143860	2048
Data	Image Data	Image Data	145908	?

4.3.2 Image Scaling and Gaussian Filter

Once the files have been interpreted, the image data can then be reconstructed into an image. Basic image reconstruction consists of a 2-Dimensional Fast Fourier Transform (2DFFT) applied to each set of image data. This creates an image of equal size to that of the original data (i.e. a 128 x 128 data set creates a 128 x 128 image). However these images are often small, typically 128x128. To get a larger image for easy viewing, they should be increased to 512x512. The best way to perform this, with the least

distortion effects (such as pixelation), is to create a 512x512 zero-filled array, and place the original data in the centre of it, before performing the 2DFFT. This results in a respectable looking larger image. Figure 32 shows an example of this technique, compared to resizing the image post-reconstruction (using GNU Image Manipulation Program, (GIMP)).

Figure 32: Pre and Post 2DFFT Image Scaling

Original data 128x128. Scaled to 512x512

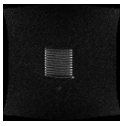

(a) Original Image.

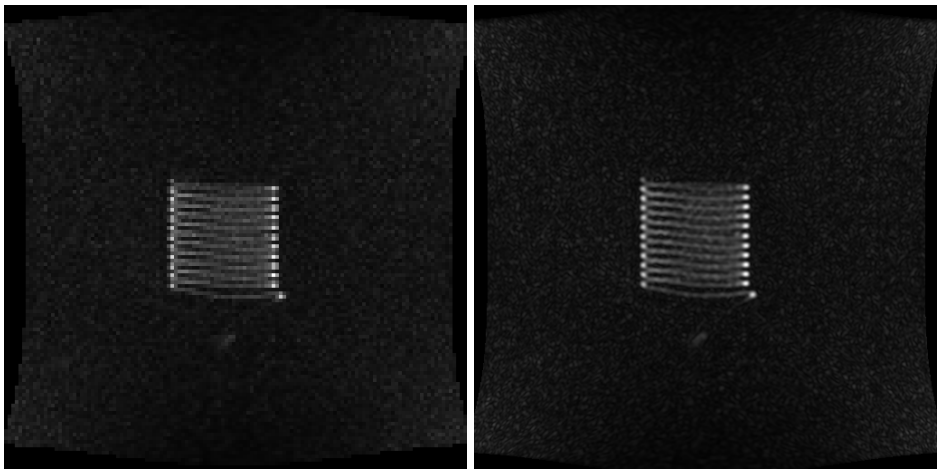

(b) Scaled using GIMP Post-2DFFT. (c) Padded with zeros Pre-2DFFT.

Often there is false detail created from this scaling process. This can be removed, with the image brightened at the same time, by applying a Gaussian Filter prior to the 2DFFT. A Gaussian filter scales the value at each data point according to a Gaussian peak centred on the middle of the array. So in a 1-dimensional array of length L_x, the data D at point x would

be scaled by:

$$D = D * e^{-(x-L_x/2)^2/2(\sigma L_x)^2}, \tag{46}$$

where σ is the standard deviation of the Gaussian filter (normalised to the length of the array). For a 2D array, the 1-Dimensional filter is simply applied once for each data-point in the x-direction, then again across each data-point in the y-direction. Figure 33 shows the result of applying the Gaussian filter with different σ values.

Figure 33: Gaussian Filter Examples

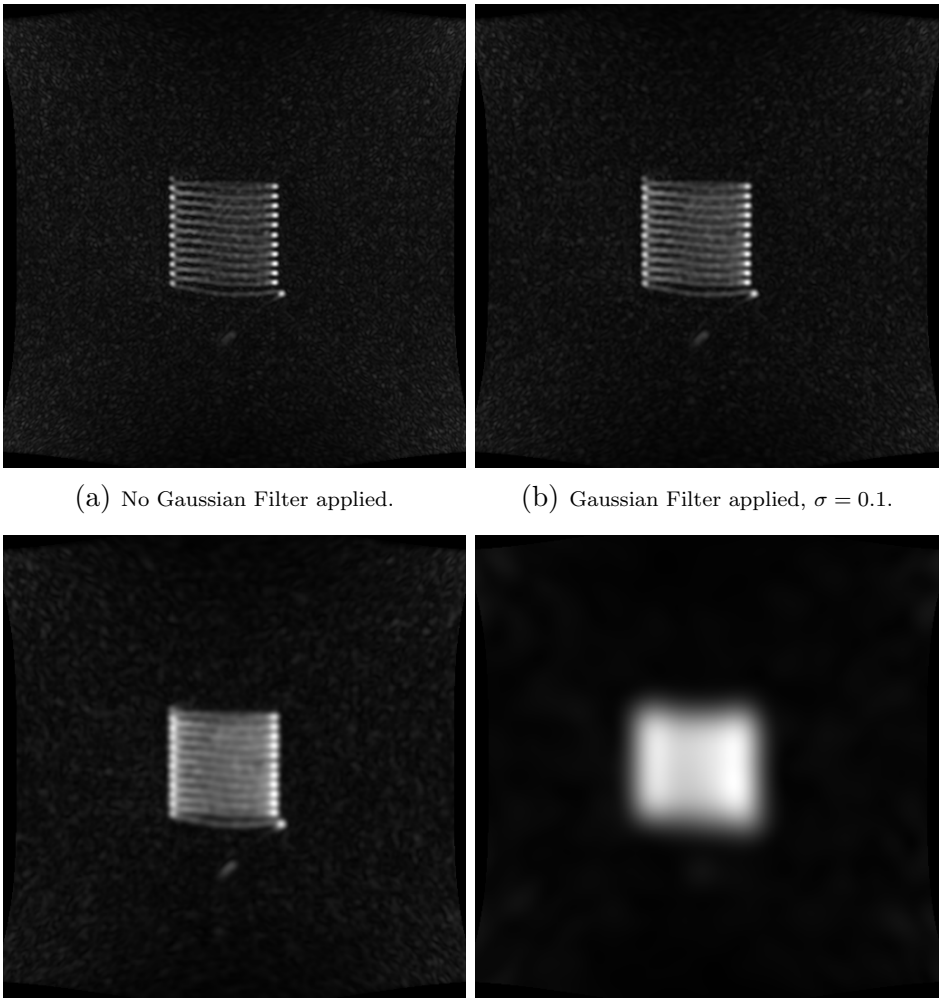

(a) No Gaussian Filter applied.

(b) Gaussian Filter applied, $\sigma = 0.1$.

(c) Gaussian Filter applied, $\sigma = 0.05$.

(d) Gaussian Filter applied, $\sigma = 0.01$.

4.3.3 Partial k-Space Reconstruction

When a fast scan sequence is required, it is sometimes necessary to perform a partial NEX scan (i.e. do less than the full amount of acquisitions), and/or a partial Echo (take less samples per acquisition) to reduce the T_R, T_E or total scan time. In both cases, the simplest way to reconstruct is to pad the missing data with zeros before performing the 2DFFT. For partial Echo images the zero-padded reconstruction looks fine, but for partial NEX the reconstructed image is significantly blurred in the phase-encode direction.

To fix the blurring, the missing (uncollected) data must be filled in. This is achieved via a simplistic version of the POCS (Projection Onto Convex Sets) algorithm [40]. Figure 34 shows the steps involved in the POCS algorithm. The original k-space data is padded with zeros, while a second data set is created, using only the central symmetric k-space data and padded with zeros. Both are then 2DFFT into images Mi and Ms respectively. Then the phase-corrected image P is created via the following formulas:

$$Mie(x,y) = e^{iarg(Mi(x,y))}, \tag{47}$$

$$P(x,y) = Mie(x,y)abs(Ms(x,y). \tag{48}$$

A inverse 2DFFT is then performed on Image P to return it to k-space data, which is then used to replace the zero-padding section in the original k-space data. A 2DFFT is applied once more to create image Mi, and then the process is repeated multiple times, finally ending when image P is satisfactory. Figure 35 shows an example image with no POCS algorithm correction and various numbers of POCS algorithm iterations. There is a

Figure 34: Summary of the Simplified POCS Algorithm.

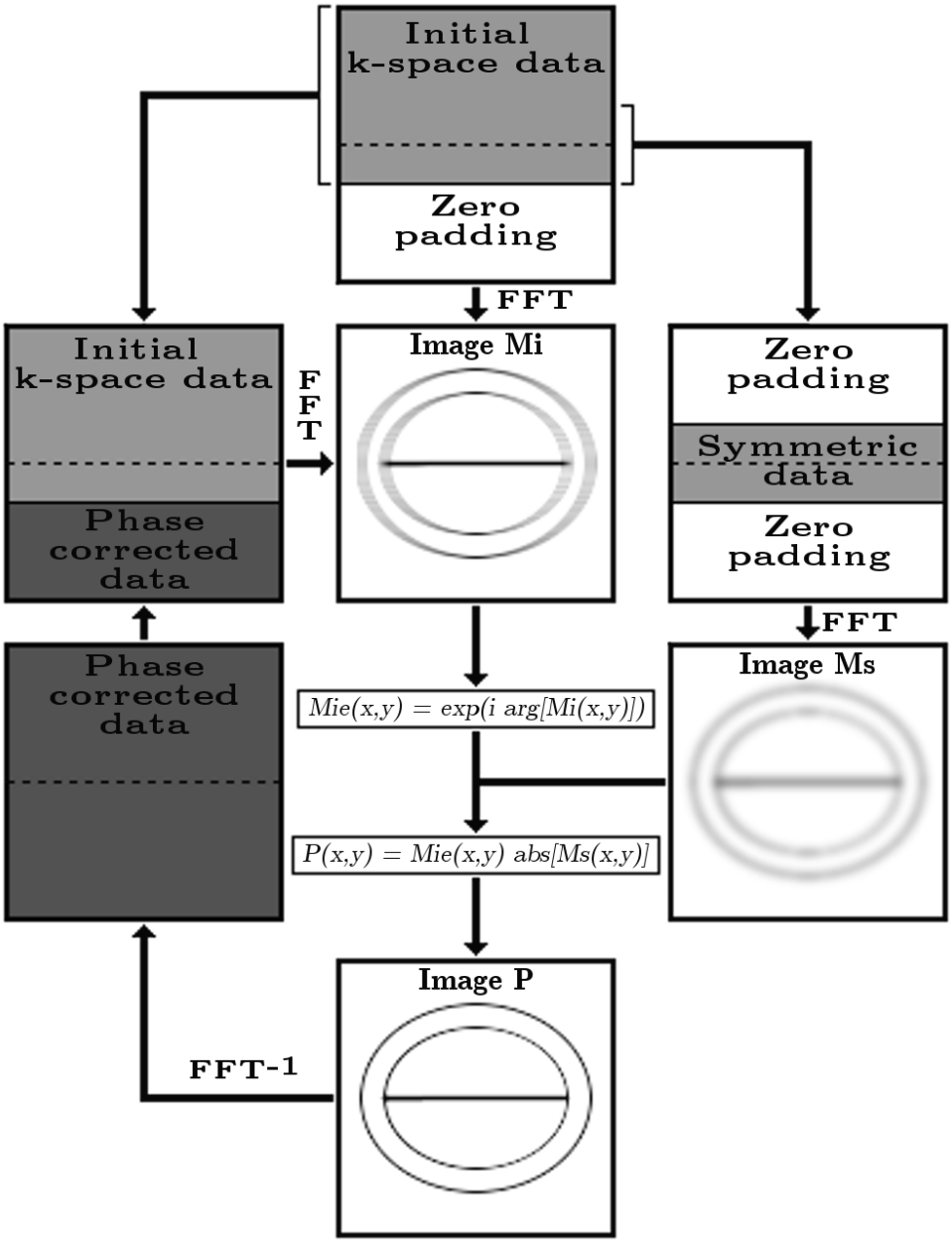

clear reduction in blur between the no POCS and 1 iteration POCS images, and a marginal reduction between 1 and 5 iterations. Performing 10 iterations did not noticeably improve the image when compared to 5 iterations, so 5 iterations of the simplified POCS algorithm has been implemented in both RECON and RECONlite's partial NEX reconstruction.

Figure 35: Partial NEX Reconstruction.

A 256x256 image taken with only 134 phase-encode steps (NEX=0.52).

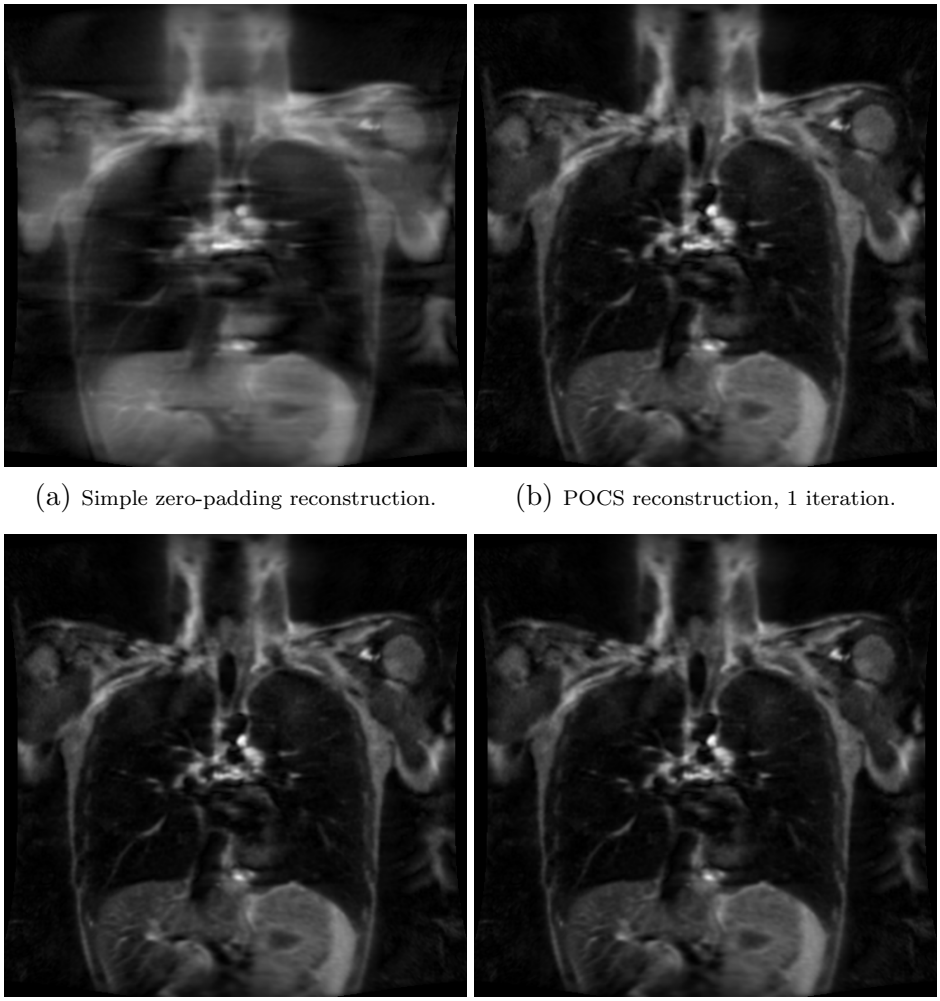

(a) Simple zero-padding reconstruction.

(b) POCS reconstruction, 1 iteration.

(c) POCS reconstruction, 5 iterations.

(d) POCS reconstruction, 10 iteration.

4.3.4 Gradient Warping

Inhomogeneous gradient fields can cause distortions in the images collected, known as 'Gradient Warping'. Although the gradients are manually corrected as much as possible when first installed, some inhomogeneity always remains, providing slight distortions to the acquired images. On the lower field 0.15T this effect is greatly reduced and is barely noticeable, however on the 1.5T scanner it can cause visible deformities, such as straight sections in the phantom being scanned appearing as curves in the acquired image.

If the inhomogeneity of the gradient fields is known, this deformation can be corrected in the final image. In fact, GE's onboard reconstruction engine does correct for the inhomogeneities in the 1.5T scanner's gradient fields. Hence it is important that RECON and RECONlite replicate this reconstruction, such that important clinical images appear as they should.

The GE 1.5T scanner contains a file, called 'gw_coils.dat', that contains the information describing the inhomogeneity of the scanner's gradient fields (as measured when first installed), via several spherical harmonic coefficients. Using spherical harmonic equations, with the provided coefficients, the gradient warping can be corrected. RECON and RECONlite use the following equations for correcting the gradient warping, based on an inter-

pretation of GE's gradient unwarping process [2]:

$$F_x = x + (c_1 x), \tag{49}$$

$$G_x = c_2 x\Big((4z^2) - x^2 - y^2\Big), \tag{50}$$

$$H_x = c_3 x\Big((8z^4) - (12y^2z^2) - (12z^2z^2) + y^4 + (2x^2y^2) + x^4\Big), \tag{51}$$

$$D_x = F_x + G_x + H_x - x, \tag{52}$$

where x,y and z are the x,y and z coordinates in real space of a pixel in the uncorrected image, D_x is the offset to apply to x to get the true x-coordinate of the pixel, and c_1, c_2 and c_3 are the spherical harmonic coefficients (label as 'SCALEX1', 'SCALEX3' and 'SCALEX5' in 'gw_coil.dat' respectively). To get the offset to the true y coordinates, the same equations are used, swapping the x and y terms, and using the respective spherical harmonic coefficients (c_1 = SCALEY1, c_2 = SCALEY3 and c_3 = SCALEY5). To get the offset to the true z coordinates, the following equations are used:

$$F_z = z + (c_1 z), \tag{53}$$

$$G_z = c_2 z\Big((2z^2) - (3y^2) - (3x^2)\Big), \tag{54}$$

$$H_z = c_3 z\Big((8z^4) - (40y^2z^2) - (40x^2z^2) + (15y^4) + (30x^2y^2) + (15x^4)\Big), \tag{55}$$

$$D_z = F_z + G_z + H_z - z, \tag{56}$$

where the respective spherical harmonic coefficients are used (c_1, c_2, c_3 = SCALEZ1, SCALEZ3, SCALEZ5 respectively).

Figure 36 shows an overview of the gradient unwarping process used in RECON and RECONlite. A Catmull-Rom spline interpolation [5] is utilised to create the new unwarped image, and the brightness corrected via a Jacobian matrix (as compressed areas become brighter and stretched areas become duller during the interpolation). Figure 37 shows an example of an image before and after gradient unwarping using RECON.

Figure 36: Summary of the Gradient Unwarping Process.

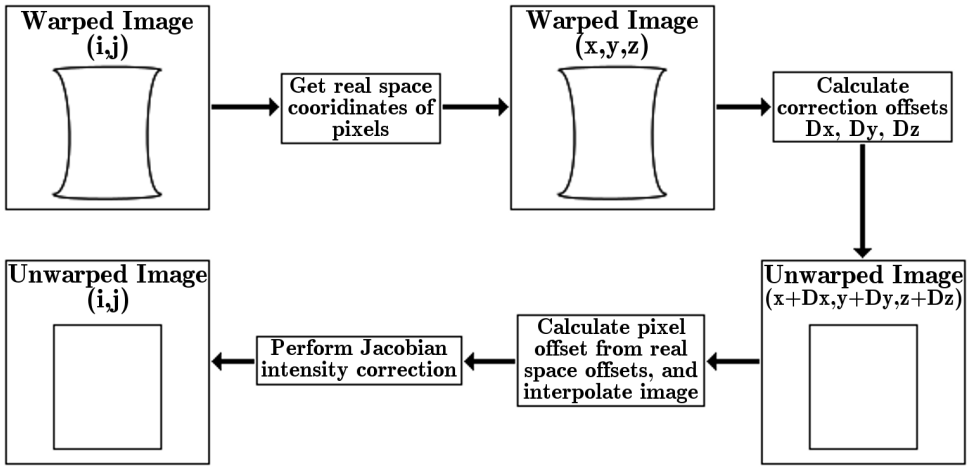

4.3.5 RECON Bonus Functions

Alongside the image reconstruction as discussed in the previous sections, the GUI program RECON has additional features over the simplified command-line program RECONlite, which only reconstructs the image and optionally stores the raw/processed data and header information in ASCII format for any further analysis elsewhere. Using RECON, the user can adjust the white balance of the images, load and reconstruct multiple files, see important scan information at a glance, and perform a small selection of further analysis.

Figure 37: Example of Gradient Warping and Correction.

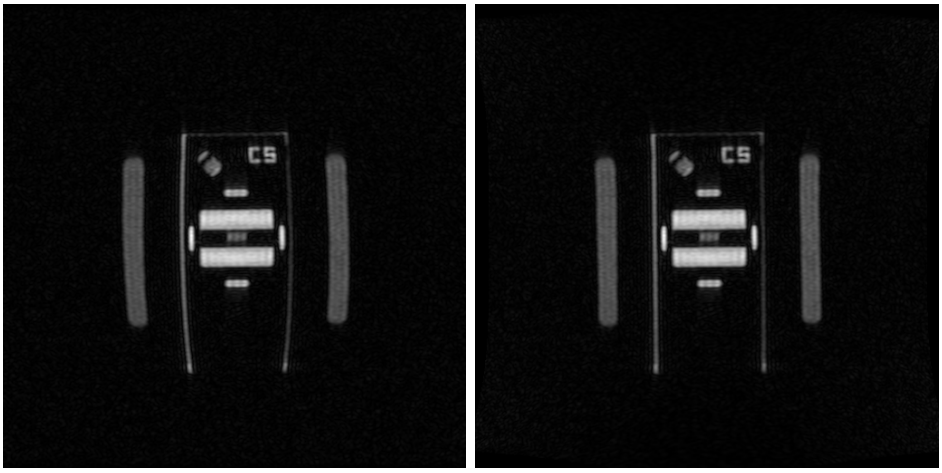

(a) Before Gradient Unwarping (b) After Gradient Unwarping

Figure 38 shows a reconstructed image, along with the some of the important scan information displayed in RECON. Figure 39 shows RECON's file selection window, where multiple scan files can be selected. Figure 40 shows how RECON can be used to alter the white balance of a reconstructed image.

For further analysis, RECON provides a mask analysis mode, where areas of each image can be selected, and certain statistics for the selected areas are displayed, such as the size of the selected area/s , and each areas signal/area ratio. Figure 41 shows an example of the mask analysis in action, comparing the signal/area ratio between the background noise, a lung, a liver, and heart muscle.

Figure 38: Scan Information and Reconstuction using RECON

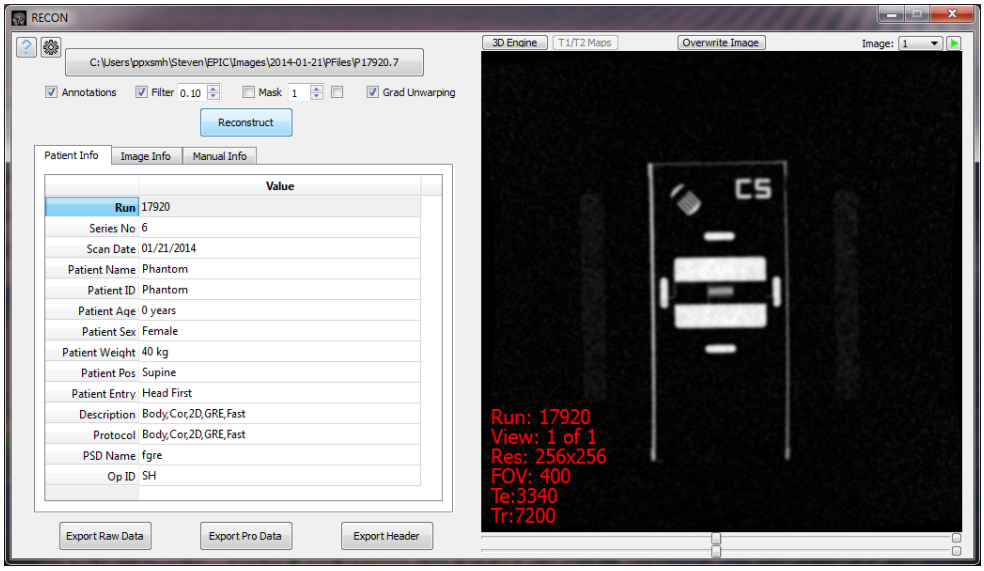

(a) Reconstructed image, with patient information displayed.

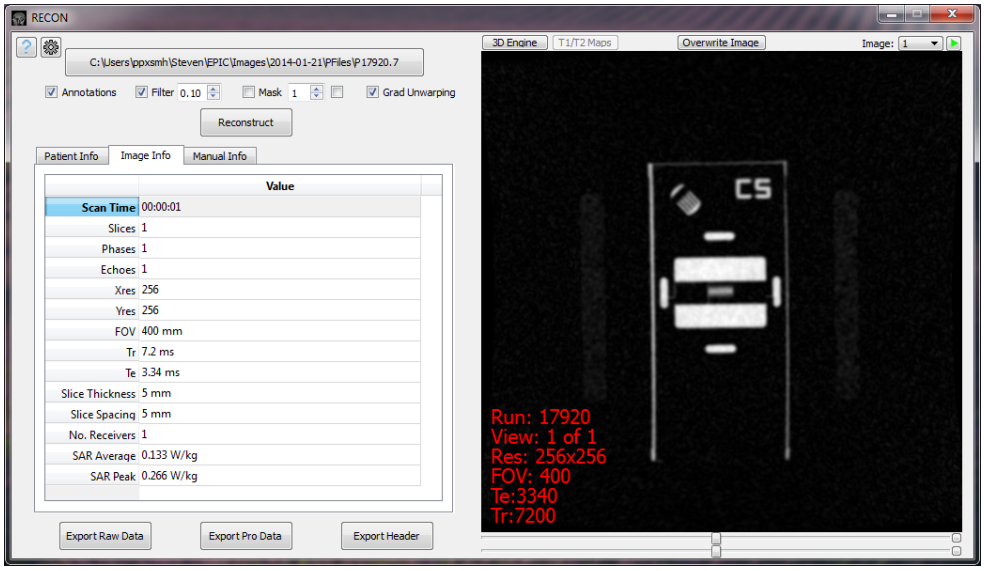

(b) Reconstructed image, with scan information displayed.

Figure 39: Selecting Files in RECON

RECON can also be used to construct T_1 and T_2 maps, if multiple scans with varying T_e or T_i times are reconstructed. The images are formed by fitting equations 39 or 41 via a least-squares algorithm to the pixels of reconstructed images, and displaying the results as a heat map. Mean T_1/T_2 values, both general and intensity weighted (from chosen scan), are displayed, and area specific mean values can be displayed using the same mask analysis program as described above. RECON can handle multiple slices/phases, but all scans must contain the same number of slices/phases. Figure 42 shows the background noise selection process required before running the map analysis. Figure 43 shows the a T_2 map, and an example of extracting area specific information using the mask analysis function.

Figure 40: Image White Balance Alteration using RECON

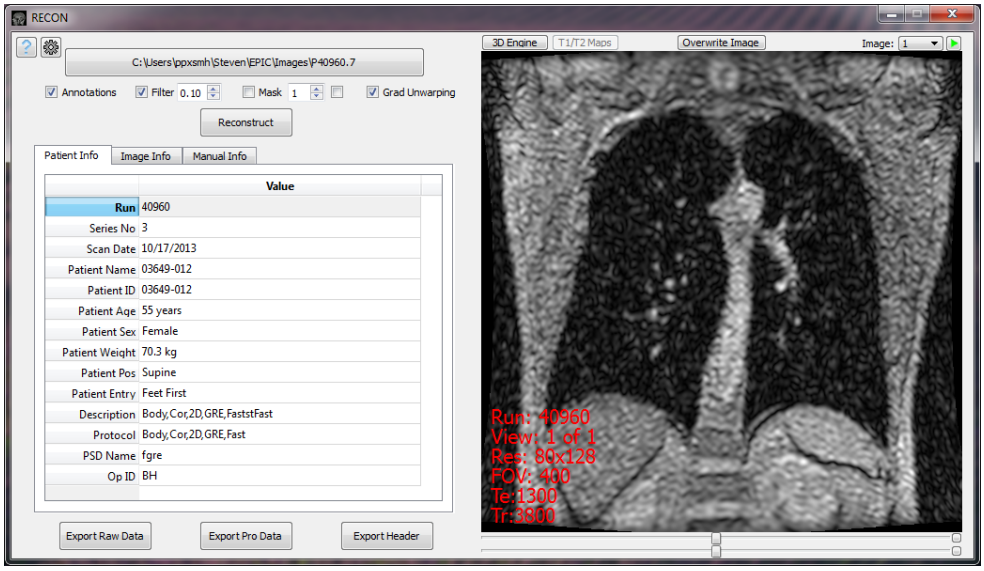

(a) Default white balance.

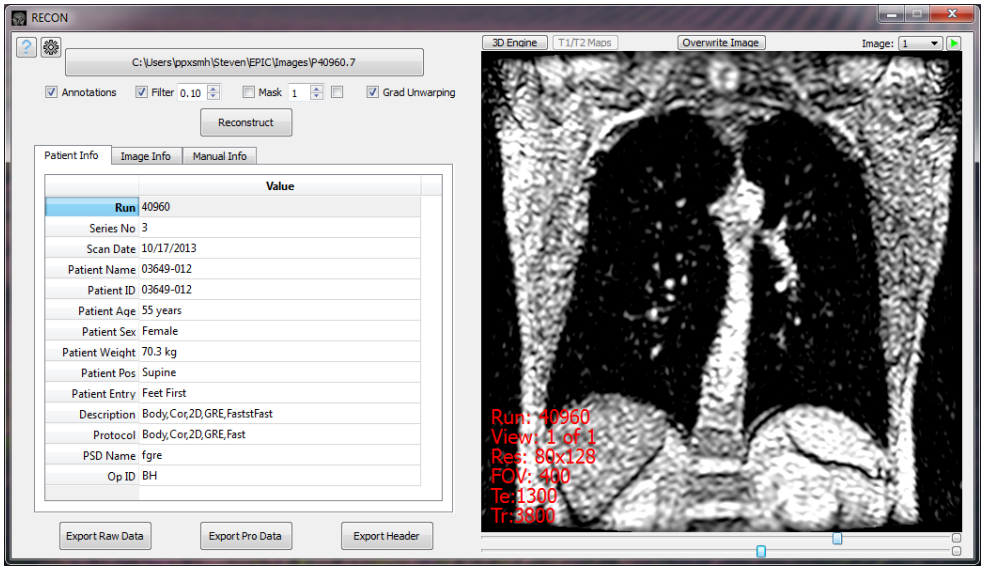

(b) Altered white balance.

Figure 41: Example of Mask Analysis in RECON

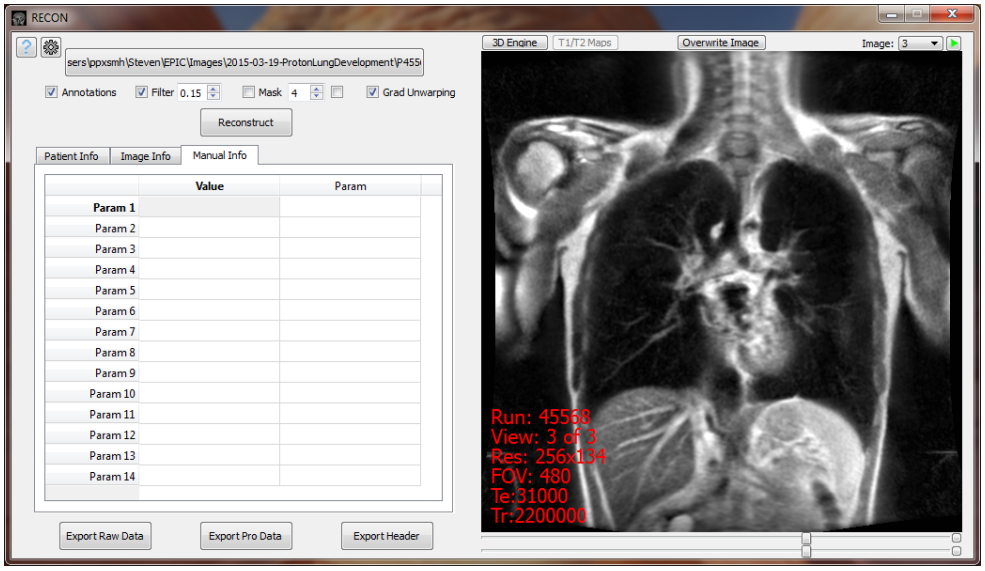

(a) Image before mask analysis is applied.

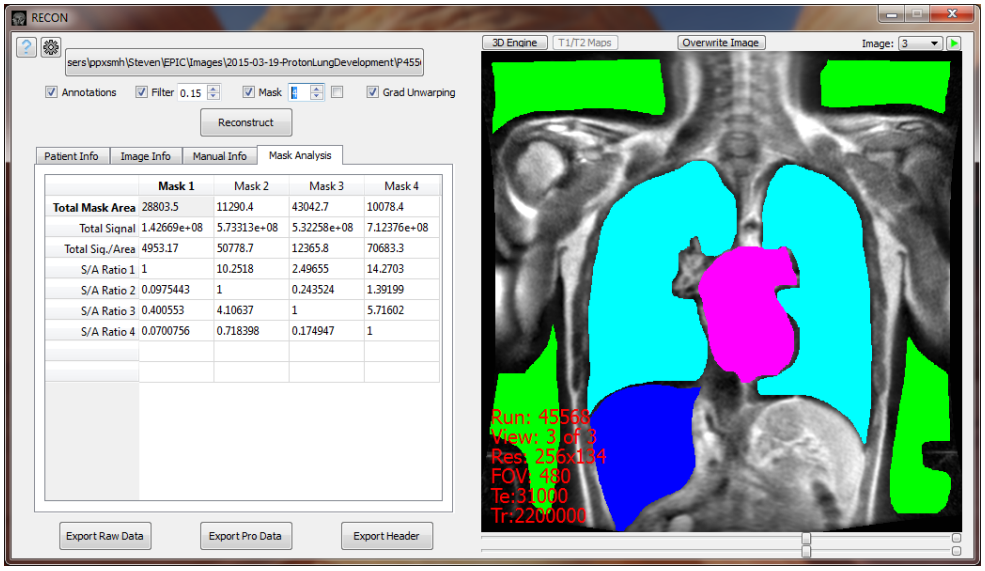

(b) Image with mask analysis is applied, where Mask 1 = Noise (green), Mask 2 = Liver (dark blue), Mask 3 = Lungs (light blue) and Mask 4 = Heart (pink).

Figure 42: RECON Noise selection using Masks

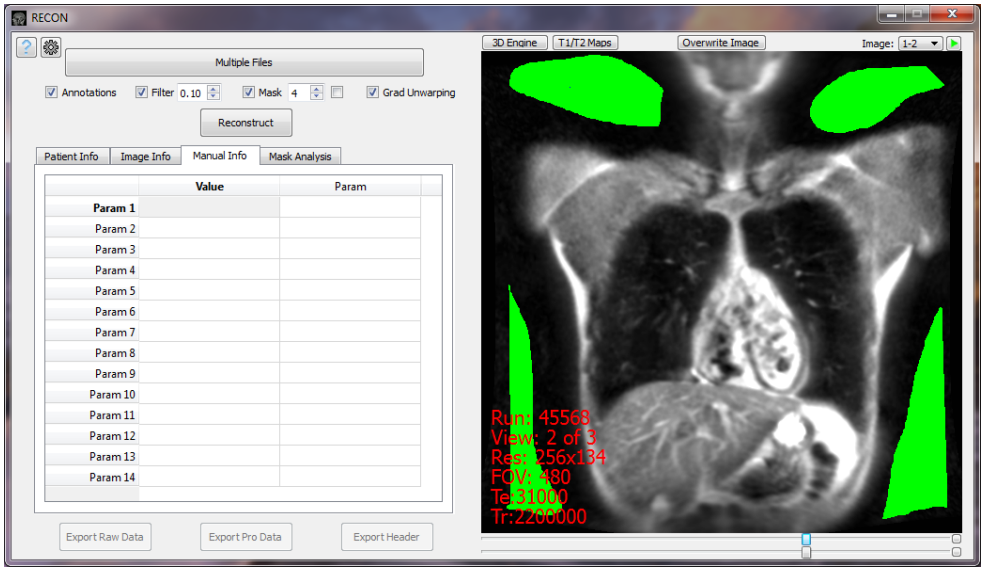

RECON also contains a 3D image reconstruction, which takes the images from multiple slices, and gives them thickness (according to their slice thickness) and assembles a 3D image that can be rotated as desired by the user. Figure 44 shows an example of the 3D image reconstruction.

Figure 43: Example of T2 Maps in RECON

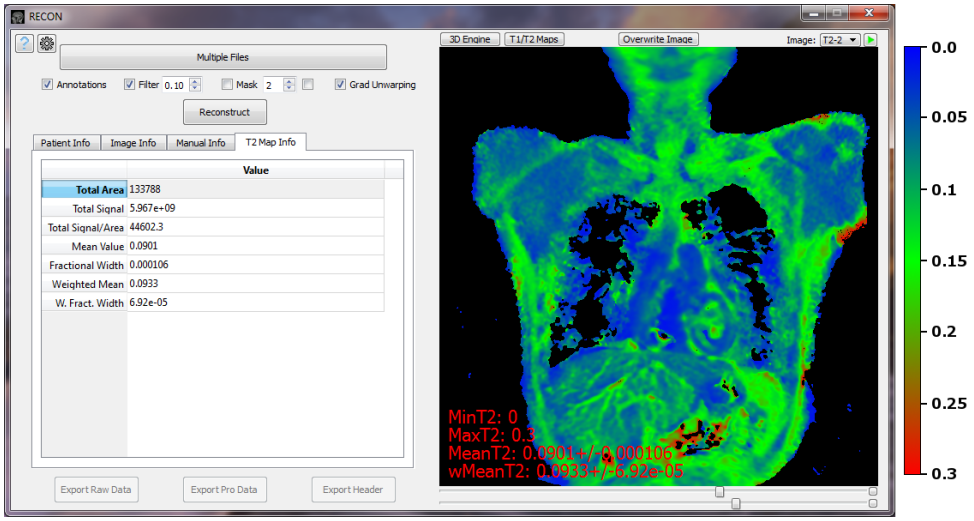

(a) Example T2 Map.

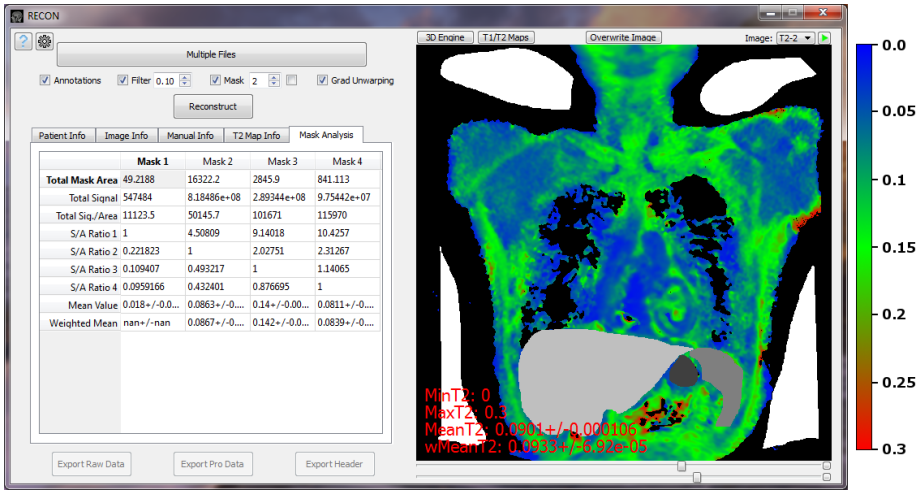

(b) Example T2 map with mask analysis.

Figure 44: RECON 3D Image Reconstruction

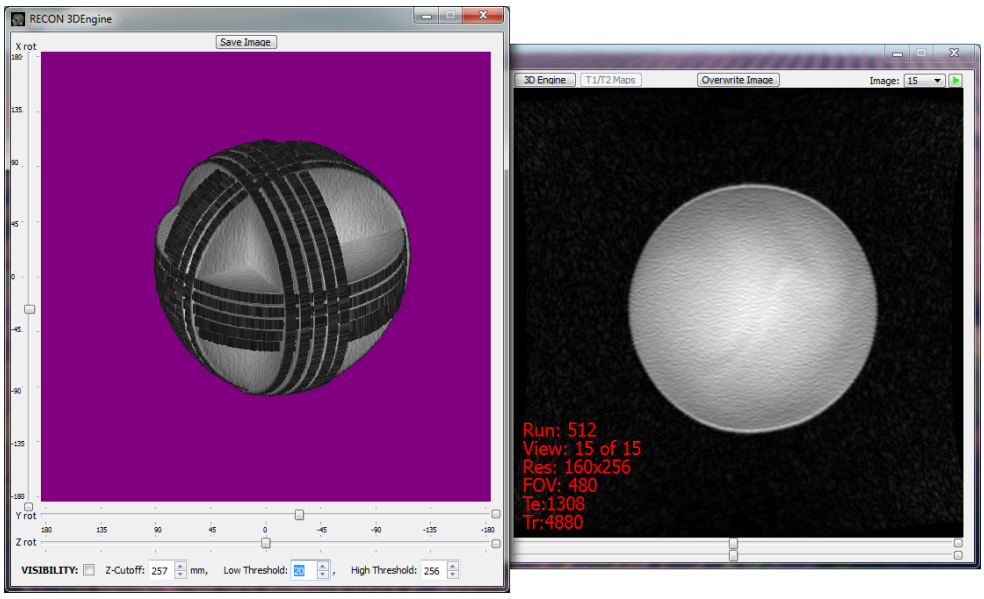

5 Chiesi Study

5.1 Background

In 2010 an estimated 300 million people across the world suffered from asthma, with the number likely to increase considerably in the following decades [11]. It is known that asthma is a chronic inflammatory airway disease which affects both the large and the small airways, and is characterised by airway hyper responsiveness, variable airflow obstruction and structural remodelling [12]. However it is not known whether the inflammatory and structural changes in asthma also occur in the distal acinar airways.

It is crucial to understand the effect asthma has on the acinar airways, as currently available inhaled therapies do not penetrate to these airways [16]. There has already been increasing interest in targeting the small airways with inhaled therapies [85]. The structure of the acinar airways can be non-invasively probed using a number of methods, such as the physiological assessment of gas mixing using Multiple Breath inert gas Washout (MBW) [74], Computed Tomography (CT) densitometry to evaluate expiratory air trapping [92], and measurement of gas diffusion using hyperpolarised noble gas MRI [108]. No comprehensive assessment of the acinar airways in asthma has been performed to date, that combines the use of all the described methods.

The gas mixing inefficiency in the lungs is thought to be due to two independent mechanisms: convection-dependent inhomogeneity (CDI), which is due to unequal convective ventilation between small conductive airways and the relatively large lung units; and diffusion-convection-dependent inhomogeneity (DCDI), a complex mechanism that arises due to an interaction between diffusive and convective gas flows occurring at the region of the airway tree where these flows are approximately equal in magnitude. Verbanck et al. [86] proposed two MBW parameters, S_{cond} and S_{acin}, as measure of CDI and DCDI (respectively). The convection-diffusion front, the region of the airway tree where convection and diffusion gas flows occur with approximately equal magnitude (and the proposed site of DCDI), is thought to be located within the pulmonary acinus. Due to this, S_{acin} was proposed as a putative physiological marker of acinar airspace disease. However, the molar mass of the probing gas can vastly alter the actual location of the convection-diffusion front, with lighter gases (such as N_2) probing earlier in the airway tree than heavier gases (such as SF_6) which can probe much more distal regions of the pulmonary acinus [74]. Patients with asthma have been observed to have elevated S_{acin} values [91], suggesting that a specific structural abnormality in the pulmonary acinus may be a characteristic of asthma, although its precise nature has not been made clear.

Using hyperpolarised ^{3}He diffusion MR, the Apparent Diffusion Coefficient (ADC) of ^{3}He within the pulmonary acinus may be measured, across a range of time-scales. The shorter time-scales, on the order of a few milliseconds, correspond to diffusion inside a single alveolus or acinar airway, with the longer time-scales, of the order of seconds, corresponding to dif-

fusion across several acinar airways [108]. There have been several studies that the short time-scale ADC of ^{3}He or ^{129}Xe is elevated in patients with emphysema [32, 50, 75, 76, 93, 105, 107], and in animal models of emphysema [10, 15, 56, 70] when compared to healthy lungs. Additionally, the ADC was found to correlate with quantitative histological measures of emphysema in a number of the studies, such as mean linear intercept, mean alveolar internal area and mean chord length [10, 15, 56, 70, 93, 105].

Physiological measurements of lung volumes [21], and quantitative CT densitometry [92] can be used to assess air trapping in the lungs. CT imaging phenotypes of asthma have recently been identified using such techniques, and air trapping has been identified as a feature of all CT imaging clusters associated with more severe disease [39].

This study was funded by the National Institute for Health Research (NIHR) and partly funded through research collaborations with Chiesi Farmaceutici S. P. A. and Novartis Pharmaceuticals. Additional funding was received from the FP7 EU Airway Disease PRedicting Outcomes through Patient Specific Computational Modelling (AirPROM) project.

5.2 Objectives

The aim of this study was to determine the nature of the acinar airway involvement in patients with asthma. This was done using quantitative Computed Tomography (CT) densitometry and ^{3}He diffusion magnetic resonance (^{3}He-MR) at multiple time-scales alongside spirometry, body plethysmography, and SF_6 Multiple Breath Washout (MBW). It was hypothesised that:

1) Asthma patients with elevated S_{acin} would manifest altered long range diffusion, suggesting intra-acinar airway disease; 2) Lung hyperinflation would not affect the degree of acinar involvement in asthma.

5.3 Method

This was a collaborative study, with contributions from the following people:

- Dr. Salman Saddique - Designed the study. Co-Principal Investigator.
- Prof. John Owers-Bradley - Helped design the study. Co-Principal Investigator. Assisted in performance of MRI scans.
- Dr. Sherif Gonem - Performed clinical lung function tests at Glenfield Hospital. Recruited and screened patients and volunteers. Performed statistical analysis. Prime author on paper.
- Dr. Niels Buhl - Provided theoretical input for formulation of the STE sequence and its analysis.
- Steven Hardy - Prepared ^{3}He polarised gas and performed MRI scans. Performed MRI raw data analysis. Created STE sequence. Performed statistical analysis of results.

Wang *et al* [93] reported a $0.0051 cm^2 s^{-1}$ difference in mean ADC at 1.5 s between the healthy and asthma groups, with a standard deviation of $0.0026 cm^2 s^{-1}$ in the healthy group and $0.0055\ cm^2 s^{-1}$ in the asthma group, using a similar methodology to that used in this study. From this it was calculated that to detect the same difference between healthy and asthma

groups at 90% power, using a t test at 5% significance level, each group required at least 15 participants.

37 asthmatic and 17 age-matched healthy subjects were recruited. The participants were recruited from the secondary care asthma centre at Glenfield Hospital, Leicester. The recruited population was representative of the secondary care asthma population in the UK, and included patients with treatment refractory disease. All participants were either never smokers, or ex-smokers with less than 10 pack years smoking history. The diagnosis of asthma in a secondary care setting was performed according to British Thoracic Society guidelines [79]. All participants gave their written informed consent, and the study was approved with alterations by the National Research and Ethics Committee (East Midlands, Leicester, Project code: 'UHL 09580' , REC: '04/Q2501/114').

Patients, in the stable state with no changes having been made to their regular inhaled or oral asthma therapy in the preceding six weeks, first visited Glenfield Hospital, before being transported to the University of Nottingham. At Glenfield Hospital, the participants underwent:

- Asthma Control Questionnaire [48]. (Asthmatic participants only)
- Asthma Quality of Life Questionnaire [47]. (Asthmatic participants only)
- 200 micrograms of salbutamol, via a metered-dose inhaler and spacer.
- Spirometry, according to [61].
- Body Plethysmography, according to [96].

- Measurement of Carbon Monoxide diffusing capacity, according to [55].
- Induced sputum inflammatory cell counts, according to [69].
- Multiple breath washout (MBW) according to [73], using sulphur hexafluoride and the technique detailed in [44].

The salbutamol was administered so that the confounding effects of airway smooth muscle tone on physiological and imaging assessments were minimised. The Global Lung Function Initiative (2012) [72] equations were used to derive predicted values and standardised residuals (z scores) for spirometry, and the European Community for Steel and Coal (1993) [71] equations were used to derive predicted values and standardised residuals (z scores) for lung volumes and the carbon monoxide transfer coefficient.

The choice of SF_6 as the inert tracer gas was due to its heavy molar mass, which means that it will probe the more distal regions of the pulmonary acinus. A lighter gas such as N_2 would not probe such regions [74]. Additionally, simulation data [26] suggests that phase III slope sensitivity to SF_6 is maximal at alveolar duct level (generations 20-21). A nose clip was worn by the participants, as they breathed an air mixture containing 0.2% SF_6. Exhaled breath SF_6 concentrations and respiratory flow were monitored by an Innocor photo-acoustic gas analyser (Innovision A/S, Odense, Denmark). A steady respiratory rate of approximately 12 breaths per minute was maintained by the participants, along with a constant tidal volume of 1 L throughout the test. A real-time visual display of inspired volume was used as a guide to allow the participant to achieve this. At the end of the wash-in phase corresponding to equalisation of inhaled and exhaled SF_6

concentrations, the participants were switched to breathing room air, until the end-tidal concentration of SF_6 in exhaled breath fell below 1/40th of original concentration (for three consecutive breaths) when the test was terminated. Custom software was then used to calculate Lung Clearance Index (LCI) [74], S_{cond} and S_{acin} [86].

At the School of Physics and Astronomy, University of Nottingham, the volunteers underwent the ^{3}He magnetic resonance (^{3}He-MR) tests, performed using a 0.15 T scanner. Upon arrival, the participant confirmed that they had filled and understood the MRI safety form. The participant was then placed into the scanner for two scans, in a supine position, the first time to undergo three CPMG scans, and the second time to undergo a gADC scan and then a STE scan. Between each set of scans there was a wait of approximately 30 minutes. During each scan the patient was given a bag containing 600 ml of ^{3}He/He^4 mixture to breathe in and hold until the scan was complete. The longest scan time was 8 seconds. The first two healthy controls, and the first seven patient volunteers entered the study during the pilot phase, and only underwent the CPMG and gADC scans. Custom software was used to calculate ADC values.

As discussed in section 4.1.1, it has already been found that ADC at short-time scales has a strong positive correlation with the degree of lung inflation, such that a volume-correction must be applied to the ADC values calculated [98]. However the effect of lung inflation on long-time scale ADC has yet to be checked. In order to investigate this relationship, a further 6 volunteers (3 Asthma, 3 Control) were recruited, who only underwent body plethysmography at Glenfield Hospital, and the STE sequence at various

lung volumes at University of Nottingham. To achieve different lung volumes, the $^3He/He^4$ mixture bag (0.5 L) was inhaled from either residual volume (RV) or from function residual capacity (FRC), and then followed by inhalation of various set sizes of air (0-1 L), before holding their breath for the scan. The results of the body plethysmography were used for the absolute values of RV and FRC.

Twenty-seven of the asthmatic patients also underwent a quantitative Computed Tomography (CT) densitometry at a later date. These were obtained using a Siemens Sensation 16 scanner at Glenfield Hospital, using the following low dose protocol: 16 x 0.75 mm collimation, 1.5 mm pitch, 120 kVp, 40 mAs, 0.5 s rotation time, 500 mm scanning field, and dose modulation off. Full inspiration and full expiration scans were obtained. A B35f kernel was used to reconstruct the images, with a slice thickness of 0.75 mm and at 0.5 mm intervals. Quantitative analysis of lung densitometry was performed using Apollo image analysis software (VIDA Diagnostics, Coralville, Iowa). The main parameters of interest were the expiration/inspiration ratio of mean lung density, a marker of expiratory air trapping [35], and the fifteenth lower percentile of the inspiratory lung attenuation curve (P_{15}), a marker of emphysema [24].

5.4 Results

This work has been published in the Journal of Allergy and Clinical Immunology [33].

Statistical analysis was performed on all data, with Student's t-test for group comparisons, Tukey test for one-way analysis of variance (multiple comparisons) with Mann-Whitney U test for continuous variables, Fisher's exact test or Chi-squared test for proportions, and the use of Pearson's correlation coefficient for investigating relationships between continuous variables.

5.4.1 Clinical and Demographic Data

Table 7 shows a selection of the demographic and clinical data collected at Glenfield Hospital. The asthma group has been subdivided into Asthma (L) and Asthma (H), according to whether they have normal or high S_{acin}, the upper limit of Low S_{acin} being defined as the mean + 1.64 standard deviations of the control group (L-$S_{acin} \leq 0.204$ L^{-1} < H-S_{acin}). Each group was well matched for age and sex. Evidence for suboptimal asthma control was seen in the H-S_{acin} group, with ACQ-6 scores significantly higher than the L-S_{acin} group. Additionally, evidence of refractory asthma was seen in 76% of the H-S_{acin} group ($p<0.05$ vs L-S_{acin}) according to the ATS criteria [78], with the majority (n=16/17) having GINA treatment step 4-5 asthma [19]. Out of the L-S_{acin}, only 45% showed evidence of refractory disease, with patients belonging to the full spectrum of GINA treatment steps.

Table 7: Demographic and Clinical Data

Showing the mean (standard error) values for each group.

	Control	Asthma (L)	Asthma (H)
No. of volunteers (n)	17	20	17
Age (years)	56.5 (2.89)	53.3 (3.2)	60.3 (2.0)
Sex (% male)	40	46.7	66.7
Height (cm)	169 (2.70)	164.9 (2.6)	170.5 (1.9)
Weight (kg)†	74.5 (3.01)	75.3 (3.5)	93.2 (4.7)$^{\#}$
Body Mass Index (kg/m^2)†	25.8 (0.8)	28.9 (1.3)	31.2 (1.4)$^{\#\#}$
Smoking Status Never Smoke (%) Ex-smokers (%) Pack Years (median[range])	 88 12 0[0-2]	 15 25 0[0-7]	 10 7 0[0-8]
Age of Onset of Asthma Symptoms (years)	-	23.4 (5.0)	27.5 (5.3)
Duration of Asthma (years)	-	23.4 (5.0)	27.5 (5.3)
Atopic Status (% positive)	-	85	82
ACQ-6 Score†	-	1.43 (0.26)	2.14 (0.22)
AQLQ(S) Score*	-	5.61 (0.23)	4.95 (0.31)
Sputum Neutrophil Count (%)	-	57.2 (6.0)	61.8 (7.1)
Sputum Eosinophil Count (%)$^{+}$	-	2.69 (1.23-5.89)	1.76 (0.76-4.04)
Blood Eosinophil Count ($x10^9/L$)	-	0.33 (0.04)	0.34 (0.07)
Daily Inhaled Corticosteroid Dose (beclometasone dipropionate equivalent) Median (μg) Range (μg)	 - -	 1000 0-2000	 1600 200-2000
Use of Long-Acting Beta-Agonists (%)	-	75	94
Regular Use of Oral Prednisolone (%)	-	20	35
Use of Leukotriene Receptor Anatagonist (%)	-	10	35
Use of a Methylxanthine (%)*	-	10	41
Patients in Asthma Treatment (Step 2:Step 3:Step 4:Step 5)*	-	1:6:9:4	1:0:9:7
Refractory Asthma (%)*	-	45	76

$^{+}$ Expressed as geometric mean (95% confidence interval).

* Trends towards significant differences across or between groups ($p < 0.1$).

† Significant differences across or between groups ($p < 0.05$).

$^{\#}$ Significant differences compared to healthy group ($p < 0.05$).

$^{\#\#}$ Highly significant differences compared to healthy group ($p < 0.01$).

5.4.2 Example MRI Data

The following are a selection of the data collected from the MR scans, with an example from each study group (Control, Asthma L and Asthma H).

Figure 45 shows the 1-dimensional Signal Profile collected from CPMG scans on a single volunteer from each group (this data is used for weighting). Figure 46 shows the 1-dimensional ADC Profile as calculated from the same scans. Figure 47 shows the final histogram data from each of the scans, which is used to get the weighted and un-weighted 13ms ADC values.

Figure 48 shows the raw Signal Intensity results from STE scans performed on the same 3 volunteers. Figure 49 shows the calculated ADC values against time for each STE scan.

Figure 45: CPMG Signal Profiles

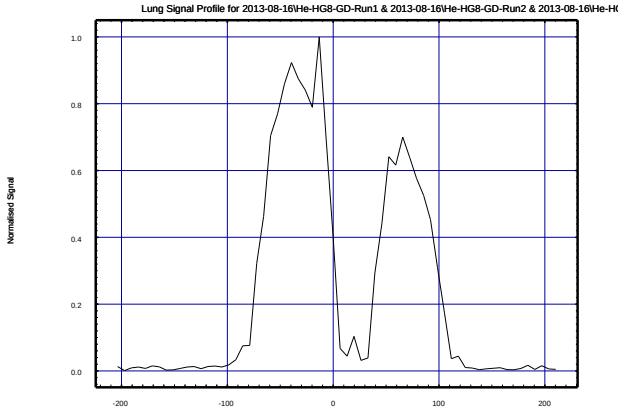

(a) Control Volunteer's Results

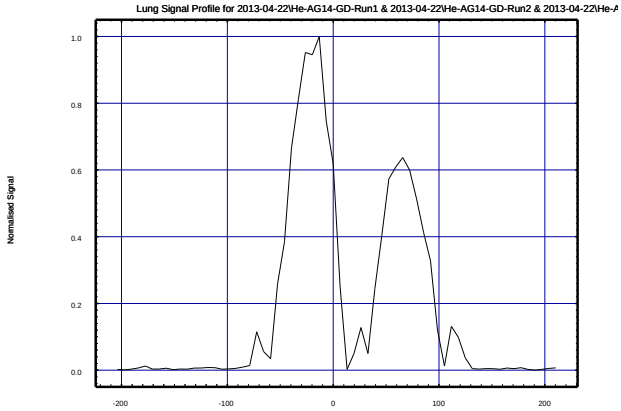

(b) Asthma L Volunteer's Results

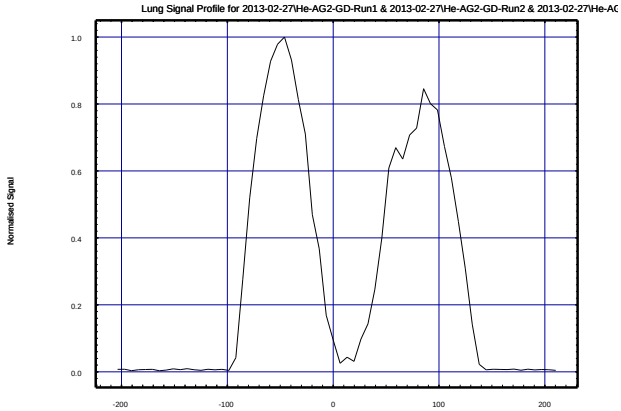

(c) Asthma H Volunteer's Results

Figure 46: CPMG ADC Profiles

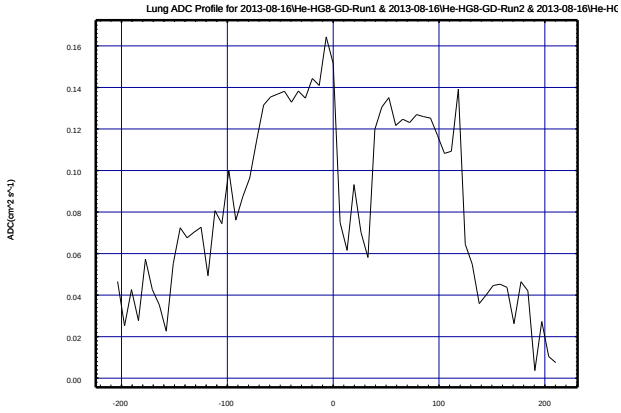

(a) Control Volunteer's Results

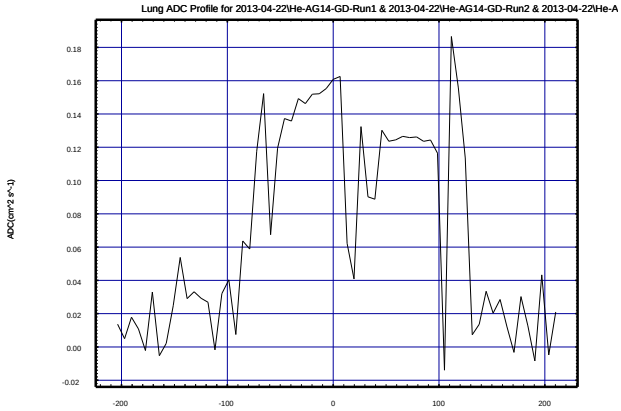

(b) Asthma L Volunteer's Results

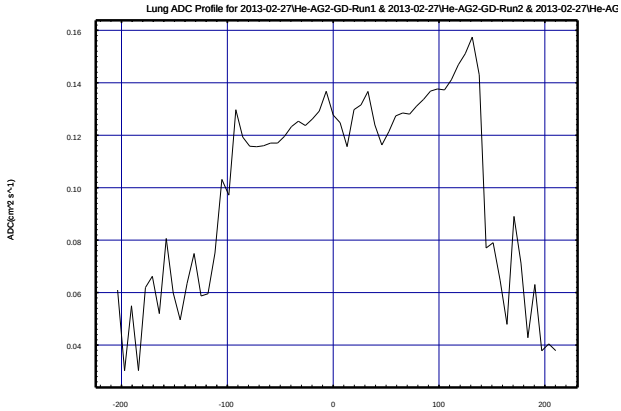

(c) Asthma H Volunteer's Results

Figure 47: CPMG Histograms

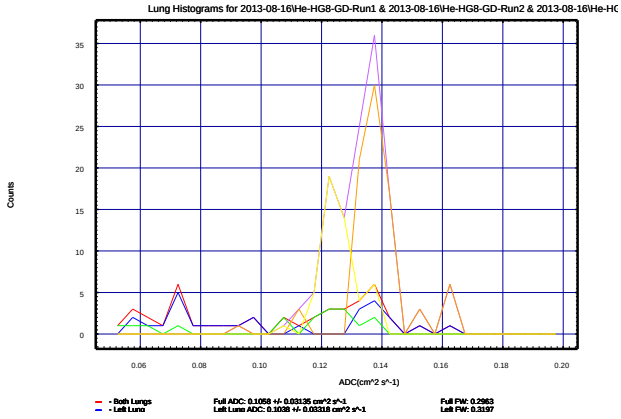

(a) Control Volunteer's Results

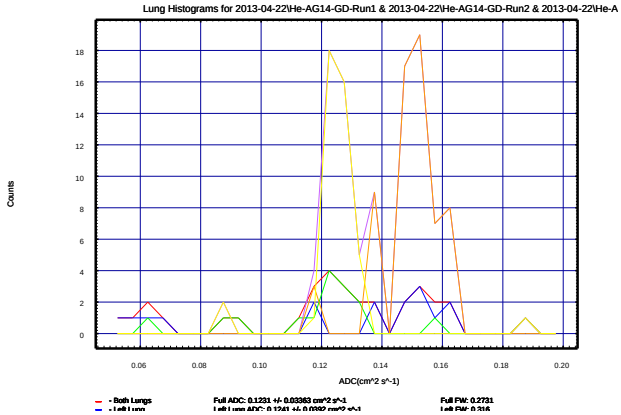

(b) Asthma L Volunteer's Results

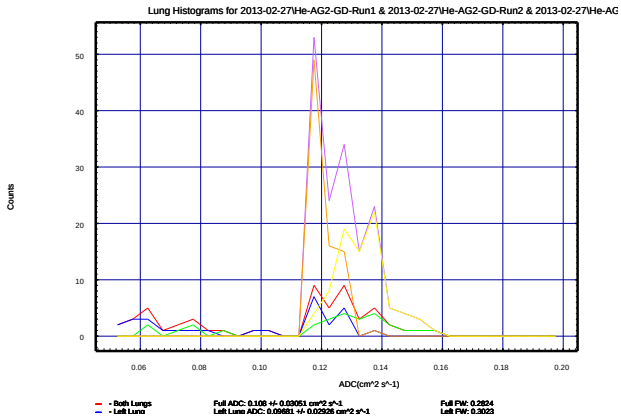

(c) Asthma H Volunteer's Results

Figure 48: STE Signal Attenuation Plots

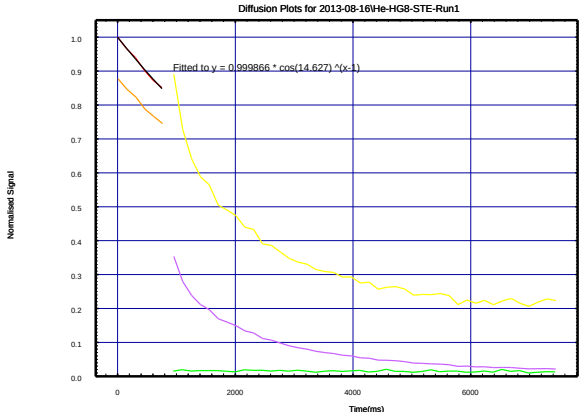

(a) Control Volunteer's Results

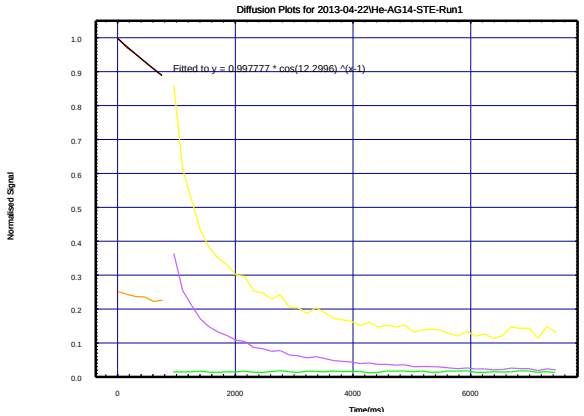

(b) Asthma L Volunteer's Results

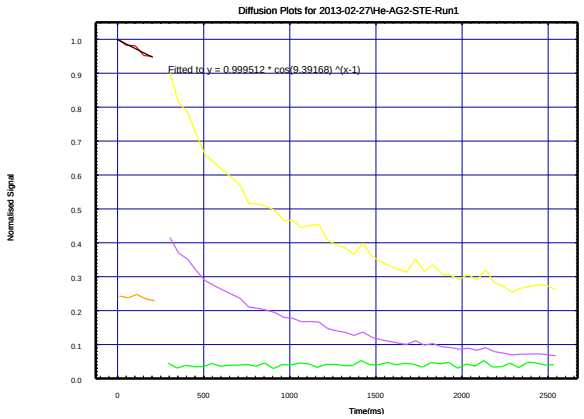

(c) Asthma H Volunteer's Results

Figure 49: STE ADC Plots

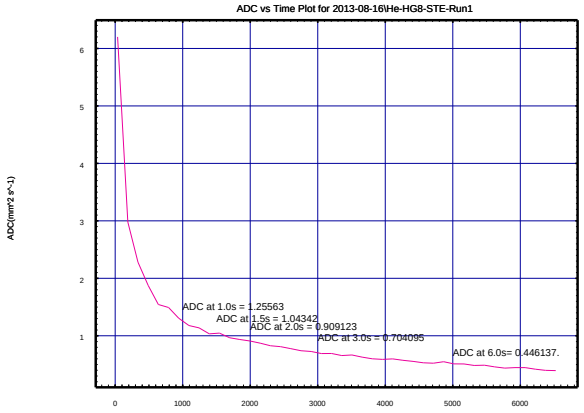

(a) Control Volunteer's Results

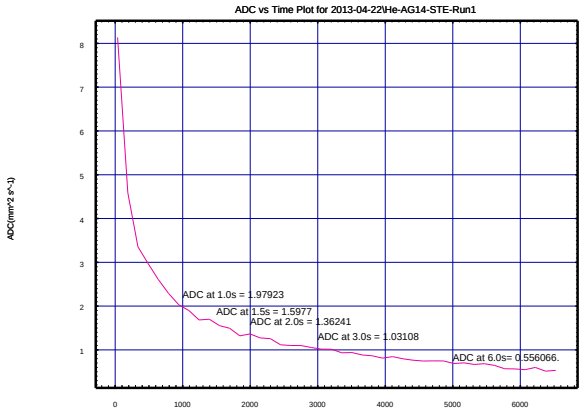

(b) Asthma L Volunteer's Results

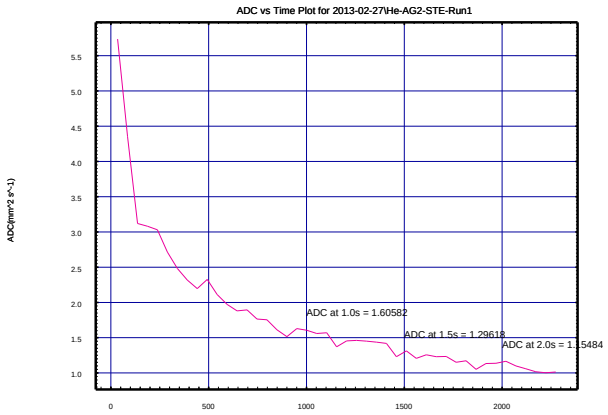

(c) Asthma H Volunteer's Results

5.4.3 Physiological, CT and MRI Data

The physiological results for each volunteer group are shown in Table 8. Expiratory air trapping and flow limitation can be seen to be significantly worse in the H-S_{acin} group than in the L-S_{acin} group. The H-S_{acin} group also has significantly lower FEV_1 (% pred.) than the L-S_{acin} group (69.3 compared to 90.9, with $p<0.01$), as well as a significantly higher residual volume to total lung capacity ratio (RV/TLC) (48.3% compared to 38.2%, with $p<0.01$) and significantly lower FRC (% pred.) (131.5% compared to 103.7%, with $p<0.01$). No difference in the carbon monoxide transfer coefficient (Kco) between the groups was seen.

The Magnetic Resonance results for each volunteer group are shown in Table 9. The short time-scale ADC values are shown, alongside their weighted (W), Volume Corrected (VC) and weighted and volume corrected (VC W) values. It can be seen that correcting for volume greatly affects the means for each group (as expected), whereas signal weighting has little effect on the control group, but does impact the values of the asthma groups (both reducing the mean and the spread). A significant difference was seen in the weighted short time-scale ADC between the L and H groups, however this difference was not seen in either of the Volume Corrected values.

Figure shows the shorter time-scale ADC results, and Figures 51-53 shows the long time-scale ADC results across all three groups. The measured ADC at 1 second was found to be significantly higher in the H-S_{acin} group, when compared to the healthy control group (0.024 compared to 0.017, with $p<0.05$), and a trend towards a significant difference between the H-S_{acin}

Table 8: Physiological, Computed Tomography Data

Showing the mean (standard error) values for each group.

	Control	Asthma (L)	Asthma (H)
FEV_1 (% pred.)****	97.7 (3.4)	83.9 (3.8) $^{\#}$	65.4 (4.8) $^{\#\#\#\#,\dagger\dagger}$
FEV_1 Z Score ****	-0.18 (0.23)	-1.16 (0.26) $^{\#}$	-2.28 (0.29) $^{\#\#\#\#,\dagger}$
FVC (% pred.)**	107.7 (3.7)	94.4 (2.9) $^{\#}$	91.6 (3.3) $^{\#\#}$
FVC Z Score **	0.53 (0.27)	-0.42 (0.21) $^{\#}$	-0.66(0.26) $^{\#\#}$
FEV_1/FVC (% pred.)****	72.1 (1.7)	70.6 (2.5)	55.6 (3.3) $^{\#\#\#,\dagger\dagger\dagger}$
FEV_1/FVC Z Score ***	-1.03 (0.23)	-1.23 (0.30)	-2.73 (0.31) $^{\#\#\#,\dagger\dagger}$
FRC (L)**	3.67 (0.26)	3.08 (0.23)	4.28 (0.26) ††
FRC (% pred.)*	114.4 (6.2)	103.7 (6.7)	131.5 (6.2) ††
TLC (L)	6.92 (0.48)	5.70 (0.34)	6.77 (0.39)
TLC (% pred.)	109.8 (3.7)	103.3 (3.8)	109.5 (3.4)
RV/TLC (%)****	31.9 (2.2)	38.2 (1.9)	48.3 (2.3) $^{\#\#\#\#,\dagger\dagger}$
RV/TLC (% pred.)****	88.3 (3.6)	104.8 (4.2)	125.6 (6.0) $^{\#\#\#\#,\dagger\dagger}$
V_A/TLC (%)****	88.2 (1.8)	82.0 (1.9)	74.3 (1.9) $^{\#\#\#\#,\dagger}$
Kco (mmol min^{-1} kPa^{-1} L^{-1})	1.55 (0.06)	1.66 (0.06)	1.58 (0.07)
LCI ****	7.34 (0.26)	7.43 (0.25)	9.59 (0.31) $^{\#\#\#\#,\dagger\dagger\dagger\dagger}$
S_{cond} (L^{-1})	0.029 (0.004)	0.054 (0.015)	0.068 (0.012)
S_{acin} (L^{-1})****	0.120 (0.012)	0.115 (0.011)	0.319 (0.026) $^{\#\#\#\#,\dagger\dagger\dagger\dagger}$
MLD E/I	-	0.83 (0.02)	0.89 (0.01)
P_{15} (HU)	-	-941 (5)	-950 (5)

Significant differences across groups denoted:
$^{*}(p < 0.05)$, $^{**}(p < 0.01)$, $^{***}(p < 0.001)$, $^{****}(p < 0.0001)$.
Significant differences compared to control group denoted:
$^{\#}(p < 0.05)$, $^{\#\#}(p < 0.01)$, $^{\#\#\#}(p < 0.001)$, $^{\#\#\#\#}(p < 0.0001)$.
Significant differences between L and H groups denoted:
$^{\dagger}(p < 0.05)$, $^{\dagger\dagger}(p < 0.01)$, $^{\dagger\dagger\dagger}(p < 0.001)$, $^{\dagger\dagger\dagger\dagger}(p < 0.0001)$.

Table 9: Magnetic Resonance Data

Showing the mean (standard error) values for each group.

	Control	Asthma (L)	Asthma (H)
ADC 13 ms ($cm^2\ s^{-1}$)	0.136 (0.006)	0.136 (0.004)	0.145 (0.006)
ADC 13 ms (W) ($cm^2\ s^{-1}$)	0.135 (0.005)	0.129 (0.003)	0.141 (0.004)†
ADC 13 ms (VC) ($cm^2\ s^{-1}$)	0.146 (0.006)	0.146 (0.006)	0.150 (0.006)
ADC 13 ms (VC W) ($cm^2\ s^{-1}$)	0.144 (0.005)	0.136 (0.004)	0.146 (0.004)
ADC 1 s ($cm^2\ s^{-1}$)	0.017 (0.001)	0.019 (0.001)	0.024 (0.002) $^{\#\#}$
ADC 2 s ($cm^2\ s^{-1}$)	0.012 (0.001)	0.013 (0.001)	0.016 (0.001) $^{\#\#,\dagger}$
ADC 3 s ($cm^2\ s^{-1}$)	0.10 (0.001)	0.011 (0.001)	0.012 (0.001) $^{\#\#,\dagger}$

Significant differences across groups denoted:
$^{*}(p < 0.05)$, $^{**}(p < 0.01)$, $^{***}(p < 0.001)$, $^{****}(p < 0.0001)$.
Significant differences compared to control group denoted:
$^{\#}(p < 0.05)$, $^{\#\#}(p < 0.01)$, $^{\#\#\#}(p < 0.001)$, $^{\#\#\#\#}(p < 0.0001)$.
Significant differences between L and H groups denoted:
$^{\dagger}(p < 0.05)$, $^{\dagger\dagger}(p < 0.01)$, $^{\dagger\dagger\dagger}(p < 0.001)$, $^{\dagger\dagger\dagger\dagger}(p < 0.0001)$.

and L-S_{acin} asthma groups (0.024 compared to 0.019, with p=0.09). No evidence for attenuation of acinar airway disease by systemic corticosteroid therapy was seen, as for patients taking long-term oral corticosteroids (OCS) the mean S_{acin} was 0.256 L^{-1}, the mean ADC at 13 ms (VC W) was 0.121 cm^2s^{-1}, and the mean ADC at 1 s was 0.023 cm^2s^{-1}, whereas those not taking OCS had a mean S_{acin} of 0.191 L^{-1} (p>0.05), a mean ADC at 13 ms (VC W) of 0.131 (p>0.05) and a mean ADC at 1 s of 0.021 cm^2s^{-1} (p>0.05).

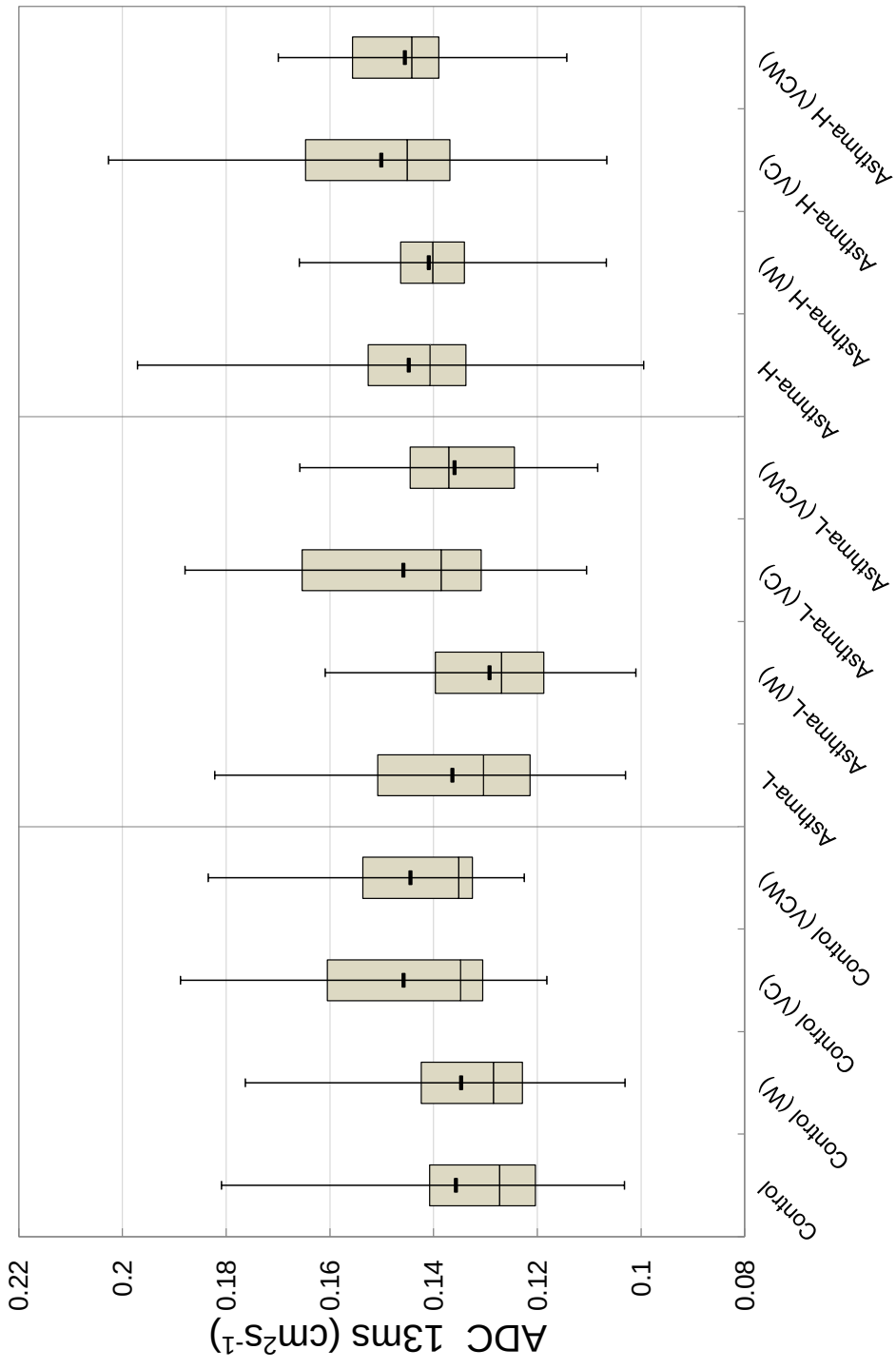

Figure 50: Box Plots of the 13 ms ADC Values for Control and Asthma Groups

Figure 51: Box Plot of the 1 s ADC Values for Control and Asthma Groups

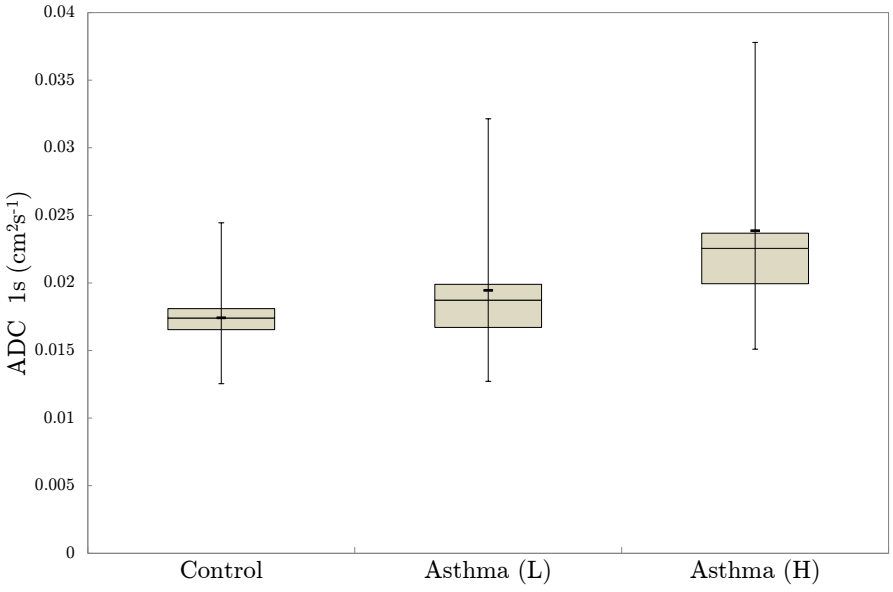

Figure 52: Box Plot of the 2 s ADC Values for Control and Asthma Groups

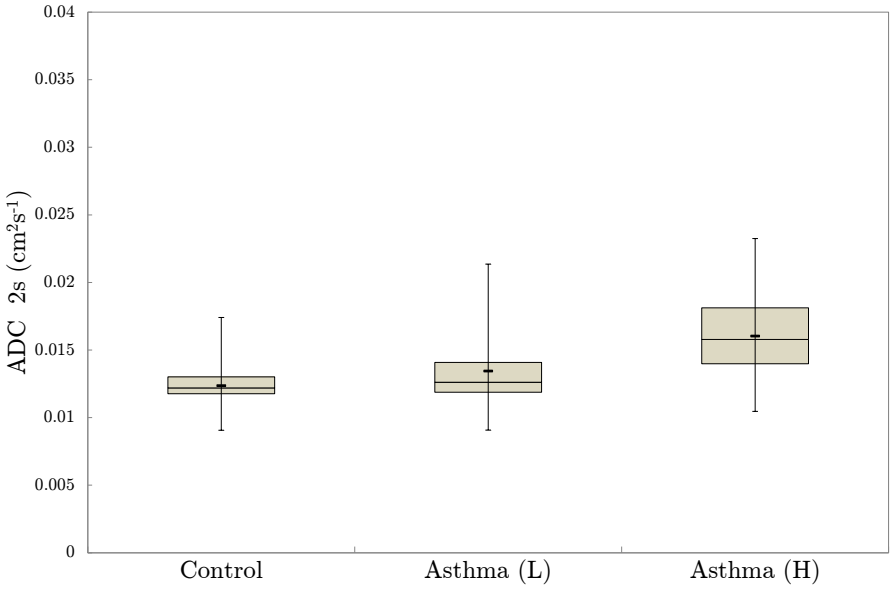

Figure 53: Box Plot of the 3 s ADC Values for Control and Asthma Groups

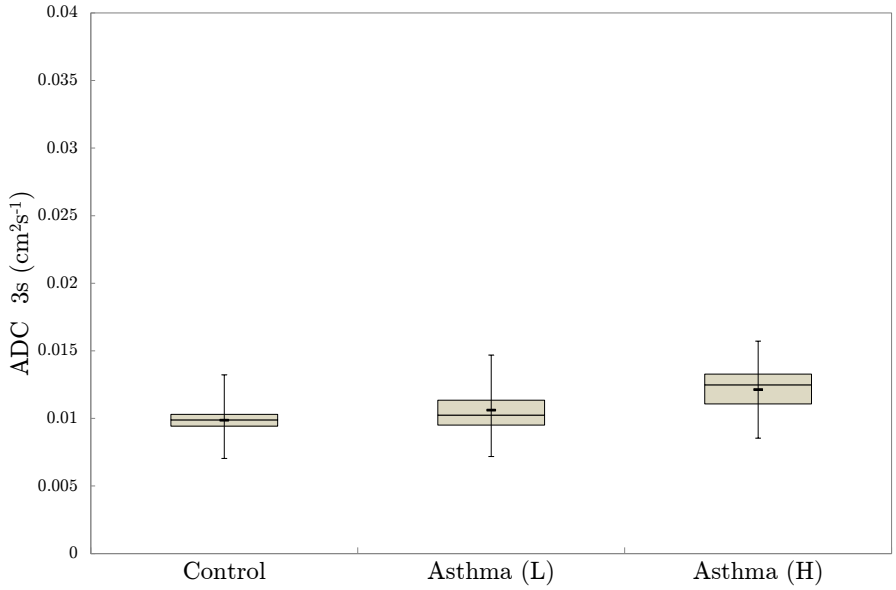

The CT densitometry data from the two asthma groups can be seen in Figures 54-56. Evidence was seen of expiratory air trapping in the H-S_{acin} group, and significantly raised MLD E/I when compared to the L-S_{acin} group (0.89 compared to 0.83, with $p<0.05$). No difference in the inspiratory P_{15} was seen across the groups. This suggests that a raised S_{acin} and CT density-based assessments of emphysema are not associated in patients with asthma.

Figure 54: Quantitative CT Densitrometry

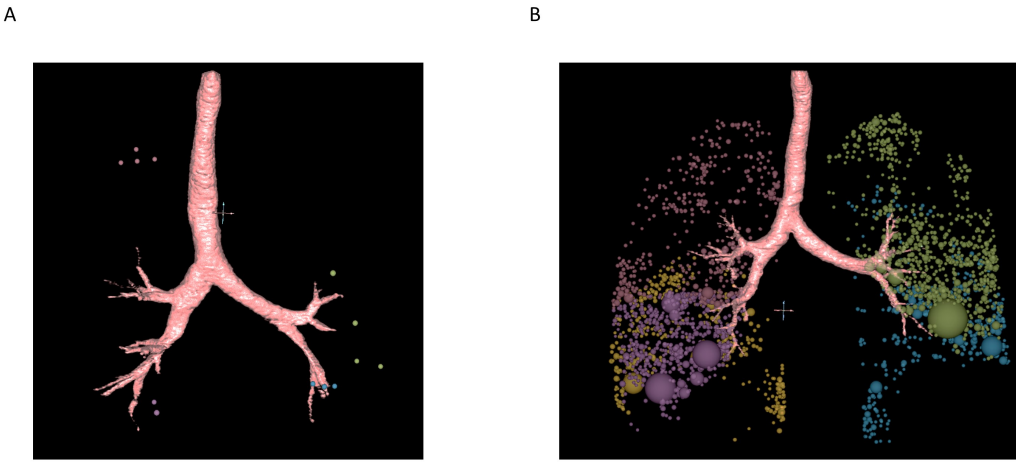

2 diagrams showing the assessment of expiratory air trapping in patients with low (A) and high (B) levels of air trapping. The coloured spheres represent areas of lung >1 ml in volume with an attenuation of expiratory scans of <-856 Hounsfield units.
Source: [33]

Figure 55: Box Plot of the MLD E/I Values for Control and Asthma Groups

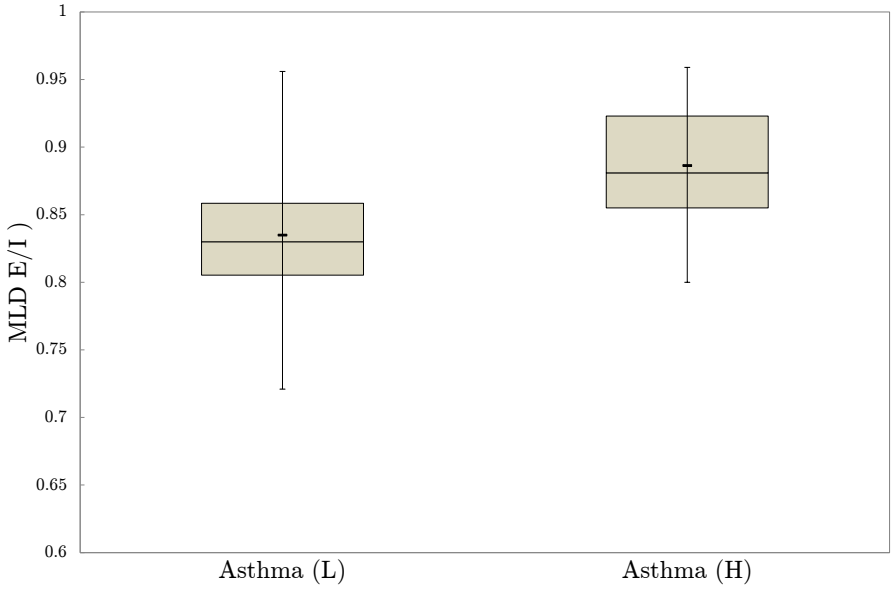

Figure 56: Box Plot of the P_{15} Values for Control and Asthma Groups

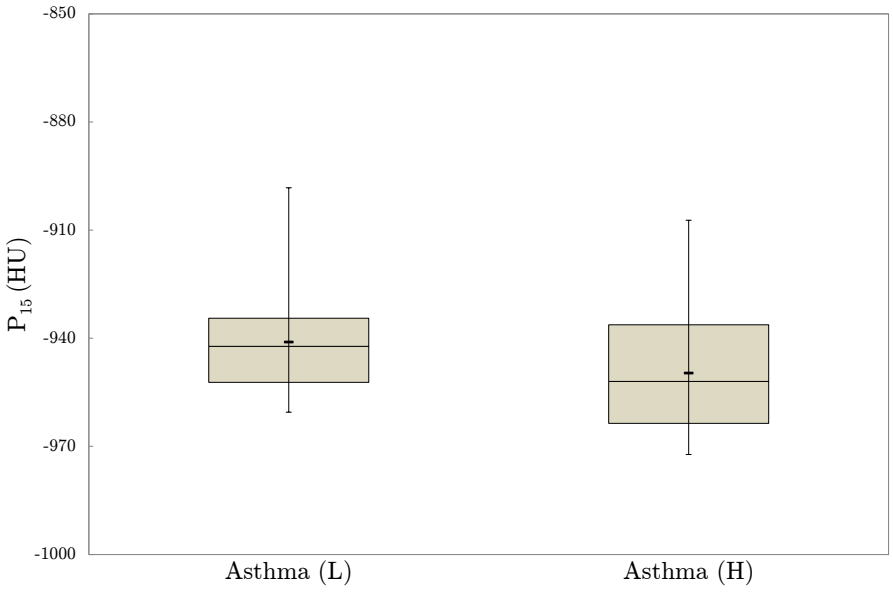

5.4.4 Comparison of Physiological and Magnetic Resonance Data

The following Table 10 shows the correlations between the measured ADCs and FRC (with Figures 57 and 60), S_{acin} (with Figures 58 and 61), and MLD E/I (with Figures 59 and 62). The correlation between S_{acin} and ADC at 13 ms (VC W) is quite weak (with R=0.40 and $p<0.05$) for the asthma groups, whereas the correlation between S_{acin} ADC at 1 s is quite strong (with R=0.65 and $p<0.001$) for asthma groups. S_{cond} did not correlate significantly with either 13 ms ADC (VC W) (with R=0.17 and p=0.37) or 1 s ADC (R=0.10 and p=0.60). This indicates that the ADC value is related only to the acinar component of ventilation heterogeneity. No strong correlations were seen in the Healthy Control group.

Functional Residual Capacity percent predicted (FRC (% pred.)) correlates strongly with both ADC at 13 ms (VC W) (R=0.65 with $p<0.0005$) and ADC at 1 s (R=0.68, $p<0.0001$) as predicted, for patients with asthma. Strong correlations were also found with the Mean Lung Density Expiratory/Inspiratory ratio (MLD E/I) with both ADC at 13 ms (VC W) (R=0.77 with $p<0.0001$) and ADC at 1 s (R=0.72 with $p<0.0001$). No strong correlations were seen in the Healthy Control group.

Table 10: Pearson Correlation Values and p-values

against	13 ms ADC (VC W)		1 s ADC	
	Control	Asthma	Control	Asthma
S_{acin}	R=-0.17, p=0.55	R=0.40, p<0.05	R=0.23, p=0.5	R=0.65, p<0.001
S_{cond}	R=-0.04, p=0.89	R=0.17, p=0.37	R=-0.06, p=0.86	R=0.10, p=0.60
FRC (% pred.)	R=0.15, p=0.65	R=0.65, p<0.0005	R=0.37, p=0.23	R=0.68, p<0.0001
MLD E/I	-	R=0.74, p<0.0001	-	R=0.72, p<0.0001

Figure 57: Scatter Graph of 13 ms ADC (VC W) against FRC.

CPMG "Global Volume-corrected and Weighted" ADC at 13 ms plotted against FRC (% predicted) for both Control and Asthma subjects.

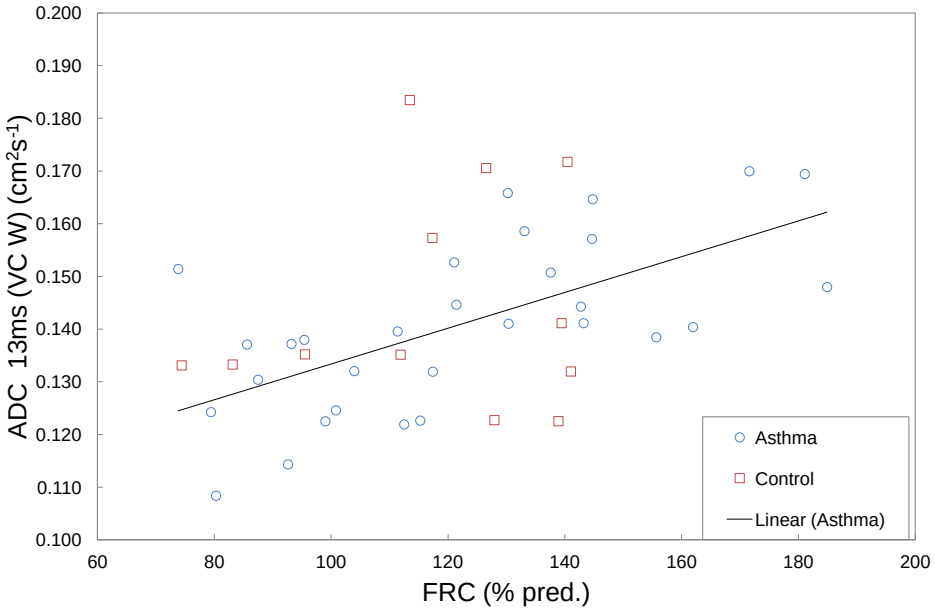

Figure 58: Scatter Graph of 13 ms ADC (VC W) against S_{acin}.

CPMG "Global Volume-corrected and Weighted" ADC at 13 ms plotted against S_{acin} for both Control and Asthma subjects.

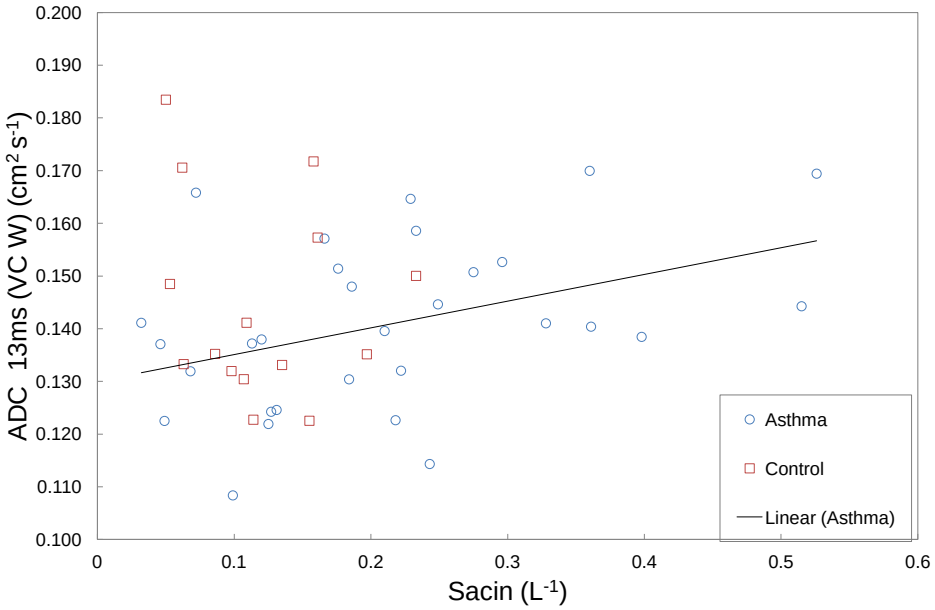

Figure 59: Scatter Graph of 13 ms ADC (VC W) against MLD E/I.

CPMG "Global Volume-corrected and Weighted" ADC at 13 ms plotted against MLD E/I for Asthma patients.

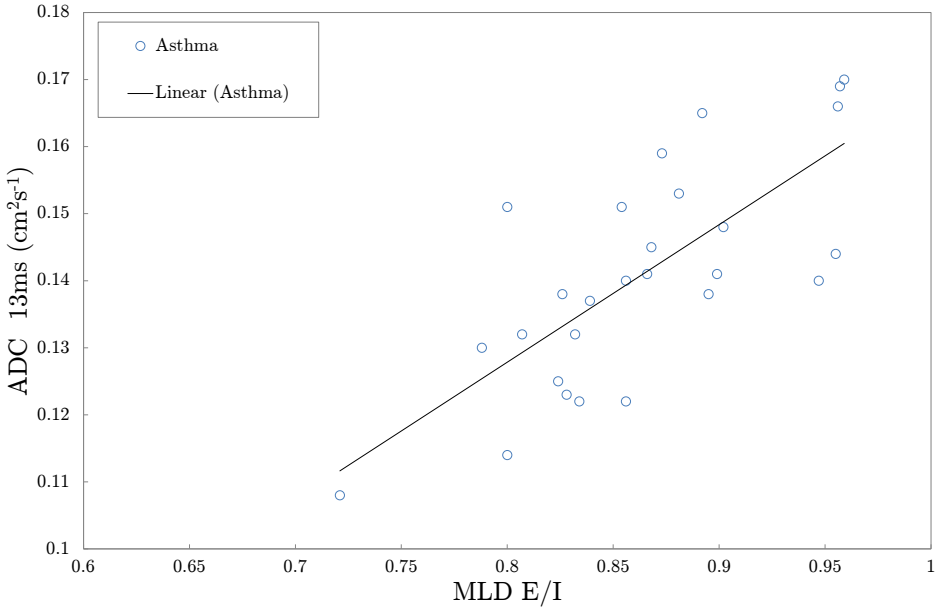

Figure 60: Scatter Graph of 1 s ADC against FRC.

STE 1 s ADC plotted against FRC (% predicted for both Control and Asthma subjects.

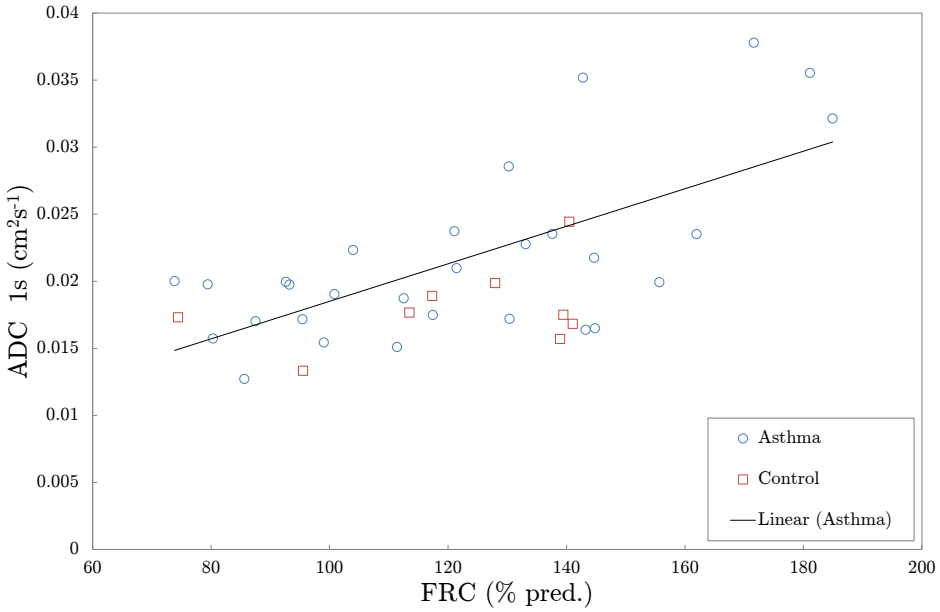

Figure 61: Scatter Graph of 1 s ADC against S_{acin}.

STE 1 s ADC plotted against S_{acin} for both Control and Asthma subjects.

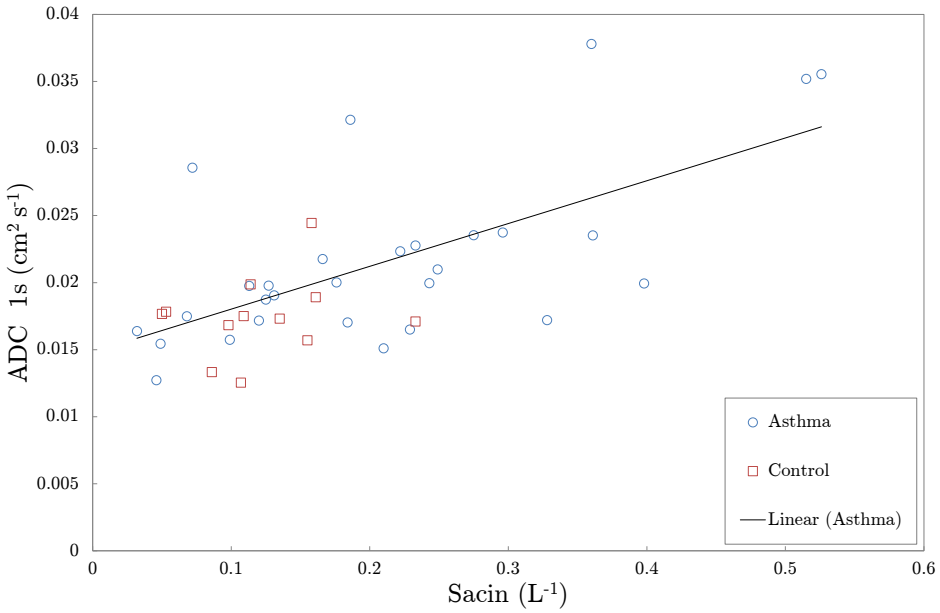

Figure 62: Scatter Graph of 1 s ADC against MLD E/I.

STE 1 s ADC plotted against MLD E/I for Asthma patients.

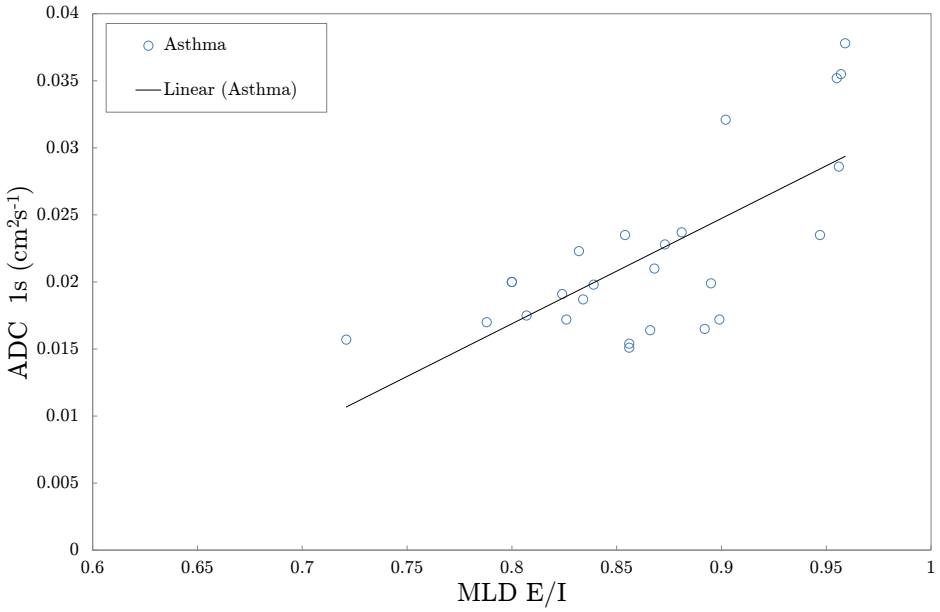

5.4.5 Lung Inflation Magnetic Resonance Data

Figures 63 and Table 11 shows the ADC at 1 s relationship with lung inflation, and Figures 64 and 65 along with Table 12 shows the ADC at 1 s relationship with percentage ^{3}He, for three asthma patients and three healthy control volunteers. Weak correlation between ADC at 1 s and lung inflation was seen in the Asthma patients (R=0.67 with p<0.05), with only a slight trend to a positive correlation seen in the healthy control volunteers (R=0.39 with p=0.15). It was found that a 50% increase in lung inflation would only result in a 3.7% increase in ADC in healthy volunteers, and a 4.5% increase in asthma patients. It was also seen that there was a significant correlation between long time-scale ADC values and percentage ^{3}He in the lungs for the healthy control volunteers. However, the relationship was found to be an inverse power, and so the ADC only changed significantly over the regions of low ^{3}He concentration. Over the range of typical usage (1.0-1.5%) the ADC values varied only slightly.

Table 11: Pearson Correlation Values and p-values for Fractional Volume and Fractional ADC at 1 s.

	(ADC_V - ADC_{FRC}) / ADC_{FRC}	
against	Control	Asthma
(V-V_{FRC}) /V_{FRC}	R=0.39, p=0.15	R=0.67, p<0.05

Table 12: Pearson Correlation Values and p-values for Percentage ^{3}He and ADC.

against	^{3}He Concentration (% by volume)	
	Control	Asthma
1 s ADC (cm^2s^{-1})	R=-0.66, p<0.01	R=-0.14, p=0.68
1.5 s ADC (cm^2s^{-1})	R=-0.67, p<0.005	R=0.003, p=0.99
2 s ADC (cm^2s^{-1})	R=-0.63, p<0.05	R=-0.14, p=0.69
3 s ADC (cm^2s^{-1})	R=-0.65, p<0.01	R=0.065, p=0.85

Figure 63: 1 s ADC and Lung Volume Relationship.

Fractional STE 1 s ADC values plotted against Fractional Volume, for 3 Control subjects and 3 Asthma subjects.

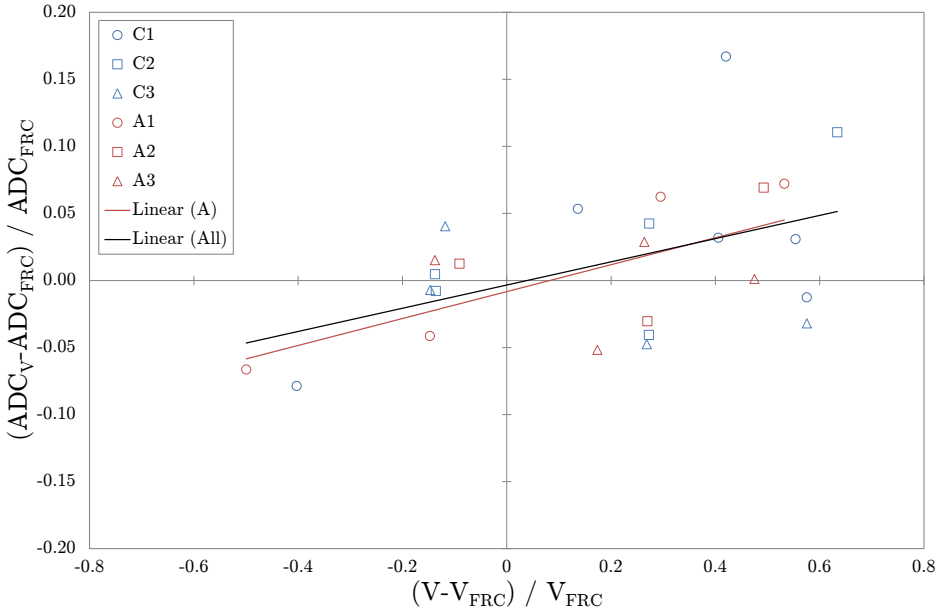

Figure 64: ADC and ^{3}He Concentration Relationship for Control Subjects.

STE ADC values plotted against Percentage ^{3}He (by volume), from 3 Control subjects.

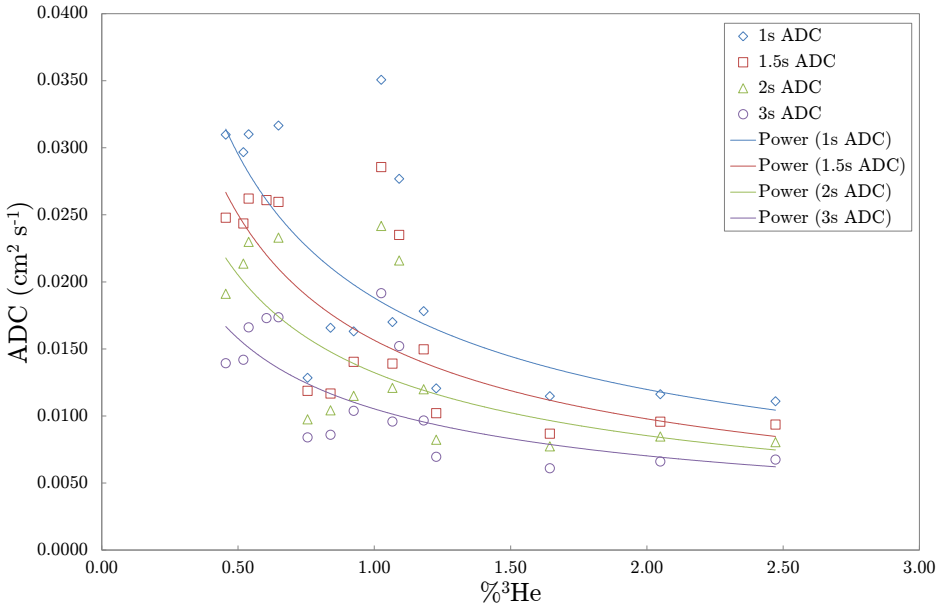

Figure 65: ADC and ^{3}He Concentration Relationship for Asthma Subjects.

STE ADC values plotted against Percentage ^{3}He (by volume), from 3 Asthma subjects.

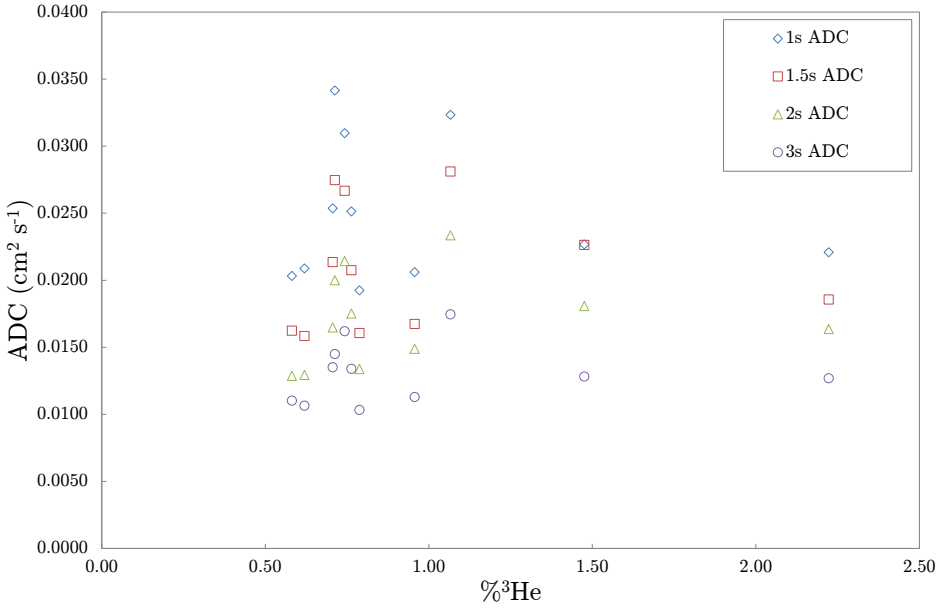

5.5 Discussion

This study found that the MBW parameter S_{acin} (using SF_6 as the tracer gas), is strongly associated with elevations in long time-scale ADC (1 second) in patients with asthma. This association was not observed in healthy subjects, and the elevations in long time-scale ADC could not be reproduced purely by inflation of the lungs. This suggest that a specific structural abnormality in the pulmonary acinus results in the elevations in long time-scale ADC values , for patients with asthma.

There has been a number of previous studies investigating the clinical significance of the acinar lesion in asthma. Farah *at al* found that S_{acin} improvements after initiation of ICS treatment were independently associated with improvements in five-point ACQ scores [28], and that the asthma control response to inhaled corticosteroid dose titration could be predicted by markers of ventilation heterogeneity [29]. Thompson *at al* found that asthma severity (as measured using the Global Initiative for Asthma treatment steps) correlated with S_{acin}, and that asthma exacerbations and increases in S_{acin} were associated [83]. It was observed in this study that elevated S_{acin} was present primarily in refractory asthma (approximately 75% of cases) and in severe asthma (GINA 4-5). Although this may reflect a higher prevalence of severe and refractory asthma in the study population, H-S_{acin} asthma group had significantly higher proportions of patients with refractory asthma than the L-S_{acin} group. No similar association was found with conductive ventilation heterogeneity marker S_{cond}. These observations may suggest that conventional pharmacotherapy will struggle with the acinar abnormalities highlighted by the SF_6 MBW parameter S_{acin} in patients

with asthma. This is hypothesis is supported by a recent interventional study, that showed no significant effect on S_{acin} in patients with asthma was observed when standard ICS treatment was swapped to small particle ICS treatment [42], although more large and appropriately powered intervention studies are required to confirm this hypothesis.

The diffusion of ^{3}He in an acinar airway is more restricted in the transverse direction than longitudinally, such that the shorter time-scale ADC measurements (such as at 13 ms) are more sensitive to the airway radius than to the airway branch length, and respectively longer time-scale ADC measurements are more sensitive to network properties of the acinar airways, with higher ADC values being associated with more inter- and intra-acinar connections. Using an anatomically realistic asymmetrically dichotomous model of the acinus, simulations have been performed that calculated long time-scale ADC values of the same order as those observed experimentally in healthy volunteers [88]. When intra-acinar collateral channels were added to the model, it produced significantly increased values of the simulated long time-scale ADC [89]. Long time-scale ADC can increase with both airway branch length, as it allows greater longitudinal displacement along the airway axes, and with alveolar sleeve width, due to this causing a increase in axial diffusion [87].

It is important to address whether the S_{acin} and long time-scale ADC correlation represents a true structural change in the pulmonary acinus, or if it is driven by the presence of expiratory air trapping and hyperinflation in asthma patients with high S_{acin}. ^{3}He MR lung morphometry was used by Hajari *et al* to assess the changes that occur in the acinar airways during lung inflation in healthy subjects [41], in which they concluded that lung inflation is primarily a result of alveolar recruitment, and only to a lesser extent by the expansion of the alveolar ducts. They also found that the alveolar sleeve depth actually decreased with increasing lung inflation. The expansion of alveolar ducts is expected to increase short to intermediate time-scale ADC, and has been shown that 13 ms ADC has a strong relationship with lung inflation [98]. In this study, we found only minor effects of lung inflation on long time-scale ADC. This suggests that the strong association between S_{acin} and long time-scale ADC cannot be accounted for by hyperinflation alone.

In this study strong correlations between the CT marker of expiratory air trapping (MLD E/I) and both the shorter and longer time-scale ADCs (13 ms and 1 s) were observed. This suggests that at the level of the acinar airways there may be common structural abnormalities, and that this may result in both expiratory air trapping and altered diffusion in the acinar airways. Micro-CT of surgical lung biopsies or resected lung specimens has been performed in patients with COPD [57], which provides a possible method of exploring the suggested structural abnormalities in asthma patients. No evidence of emphysema in patients with asthma and a raised S_{acin} was seen in this study, and neither P_{15} nor Kco was found to differ

between the L-S_{acin} and H-S_{acin} groups. Normal Kco values in patients with asthma was also observed in two previous studies [34,91], suggesting that the alveolar-capillary membrane remains intact in asthma patients with elevated S_{acin}.

5.6 Potential Limitations

This study has a few potential limitations. Firstly the majority of the asthma patients were drawn from a secondary care centre, meaning that the results may not match the general asthma population, such as a higher proportion of patients with refractory asthma, or taking long-term oral corticosteroids. The rationale for recruiting from the asthma centre included optimisation of other factors, such as rhino sinusitis, treatment non-adherence and psychological/behavioural issues, and as such were not specifically identified from a treatment refractory cohort.

Additionally, the mean age of the asthma patients in this study may be slightly older than the general asthma population, as may be the proportion of males and females across the groups. The proportion of males in the asthma group was 51.4%, which is much greater than the 36.9% proportion published in a previous large difficult asthma cohort [43].

A further potential limitation stems from the sensitivity of the pulmonary acinus to cigarette smoke that has been shown previously [90]. It was therefore necessary that current and/or heavy smokers were excluded from the recruitment for this study, despite that the general asthma population contains non-smokers and ex-smokers as well as current and heavy

smokers. If current and heavy ex-smokers had been included then the smoking associated acinar changes would have confounded the airway diffusion measurements. Despite this, it still remains possible that differences in low-grade cigarette smoke exposure may account for some of the proposed structural changes observed in this study.

Another limitation is seen in the results of the 13ms ADC values. The weighting affects the results of the asthma groups more than the control groups. This may be due to the weighting suppressing areas with low amounts of helium, which may correspond to areas of low ventilation (i.e areas of pathology). This should be investigated further before any conclusions can be drawn.

Finally, the MR pulse sequences used do not provide three-dimensional spatial information. Future studies incorporating more complex sequences that provide three-dimensional spatial encoding could provide further insights into the structural correlations of inert gas MBW parameters.

5.7 Conclusions

It was found that there appears to be an association between MBW parameter S_{acin} and a structural abnormality in the pulmonary acinus, which causes subtle alterations in diffusion within the acinar airways, in patients with asthma. Additionally, the proportion of cases with refractory asthma and a high S_{acin} was found to be significantly higher than the for asthma patients with normal S_{acin}. This suggests that the lesion may be clinically important, warranting further evaluation as this observation should only be

regarded as exploratory.

Further longitudinal studies are required before the long-term prognostic significance of acinar airway disease in asthma can be determined. Additionally further studies will help to determine whether the acinar airway disease will be responsive to fine-particle inhaled or systemic therapies. The affect of signal weighting on the short time-scale ADC values should also be investigated further, to understand whether this step is beneficiary in reducing the spread and error in the asthma groups, or whether it negatively affects the results by suppressing areas of pathology.

6 Leicester Royal Infirmary Cystic Fibrosis Study

6.1 Background

It is estimated that in the United Kingdom 1 in every 2,500 babies are born with cystic fibrosis, with more than 9,000 people living with the condition [64]. Cystic Fibrosis is known to affect the mucus in the upper airways, and leads to permanent infections. However, little is known whether the hyper-viscous mucus and the infections and inflammations affect the small airways.

There have been several studies that show the short time-scale ADC of ^{3}He or ^{129}Xe is elevated in patients with emphysema [32, 50, 75, 76, 93, 105, 107], and in animal models of emphysema [10, 15, 56, 70] when compared to healthy lungs. Additionally, the ADC was found to correlate with quantitative histological measures of emphysema in a number of the studies, such as mean linear intercept, mean alveolar internal area and mean chord length [10, 15, 56, 70, 93, 105].

6.2 Objectives

The aim of this study was to determine if there is any relationship between the measurements of spirometry and body plethysmography, and the measurements of the ^{3}He-MRI CPMG and gADC sequences.

6.3 Method

This was a collaborative study, with contributions from the following people:

- Dr. Erol Galliard - Helped design the study. Co-Principal Investigator.
- Prof. John Owers-Bradley - Helped design the study. Co-Principal Investigator. Assisted in performance of MRI scans.
- Dr. Caroline Beardsmore - Performed clinical lung function tests at LRI. Recruited and screened patients and volunteers.
- Noor Al-Khathlan - Performed clinical lung function tests at LRI. Performed statistical analysis of results.
- Ian Ball - Prepared ^{3}He polarised gas and performed MRI scans. Created gADC and CPMG MRI sequences.
- Dr. Niels Buhl - Provided theoretical input for formulation of the gADC sequence and its analysis using the Yablonskiy model.
- Steven Hardy - Prepared ^{3}He polarised gas and performed MRI scans. Performed MRI raw data analysis. Performed statistical analysis of results.

18 Cystic Fibrosis patients and 27 age matched healthy subjects were recruited. All participants gave their written informed consent, and the study was approved with alterations by the National Research and Ethics Committee (East Midlands, Leicester, Project code: 'UHL 09580' , REC: '04/Q2501/114').

Participants first visited Leicester Royal Infirmary, before being transferred to the University of Nottingham via taxi. At Leicester Royal Infirmary, after giving written informed consent, the participants underwent spirometry, body plethysmography, and nitrogen washout tests. Then at the School of Physics and Astronomy, University of Nottingham, the participants underwent ^{3}He magnetic resonance (^{3}He-MR) scans, performed using a 0.15T scanner. Upon arrival, the participant confirmed that they had filled and understood the MRI safety form. The participant was then placed into the scanner twice, in a supine position, the first time to undergo three CPMG scans, and the second to undergo two gADC scans. Between scan sets there was an approximately 30 minute wait. During each scan the patient was given a bag containing 500 ml of ^{3}He/He^4 mixture to breath in and hold until the scan was complete. The longest scan time was 5 seconds.

6.4 Results

Statistical analysis was performed on all data, with Student's t-test for group comparisons, Chi-squared test for proportions, and the use of Pearson's correlation coefficient for investigating relationships between continuous variables.

6.4.1 Example MRI Data

The following are a selection of the data collected from the MR scans, with an example from each study group (Control and Cystic Fibrosis).

Figure 66 shows the 1-dimensional Signal Profile collected from CPMG scans on a single volunteer from each group (this data is used for weighting). Figure 67 shows the 1-dimensional ADC Profile as calculated from the same scans. Figure 68 shows the final histogram data from each of the scans, which is used to get the weighted and un-weighted 13ms ADC values.

Figure 69 shows the raw Signal Intensity results from gADC scans performed on the same 2 volunteers. Figure 70 shows the signal corrected b-space plots for each gADC scan, along with the fitting used to calculate the R and h values.

6.4.2 Demographic, Physiological and Magnetic Resonance Data

Table 13 and Figure 71 shows a selection of the demographic and physiological data collected at Leicester Royal Infirmary, alongside the Magnetic Resonance data collected at the University of Nottingham. The two groups, Control and CF, have been well age-matched, and roughly equal in female/-male selection. It can be seen that there is very significant difference between the Control and CF groups in the FEV_1, FEV_1/FVC, RV/TLC and LCI values. The short time-scale ADC values are shown, alongside their weighted (W), Volume Corrected (VC) and weighted and volume corrected (VC W) values. It can be seen that correcting for volume greatly affects the means for each group (as expected), whereas signal weighting has little effect on

Figure 66: CPMG Signal Profiles

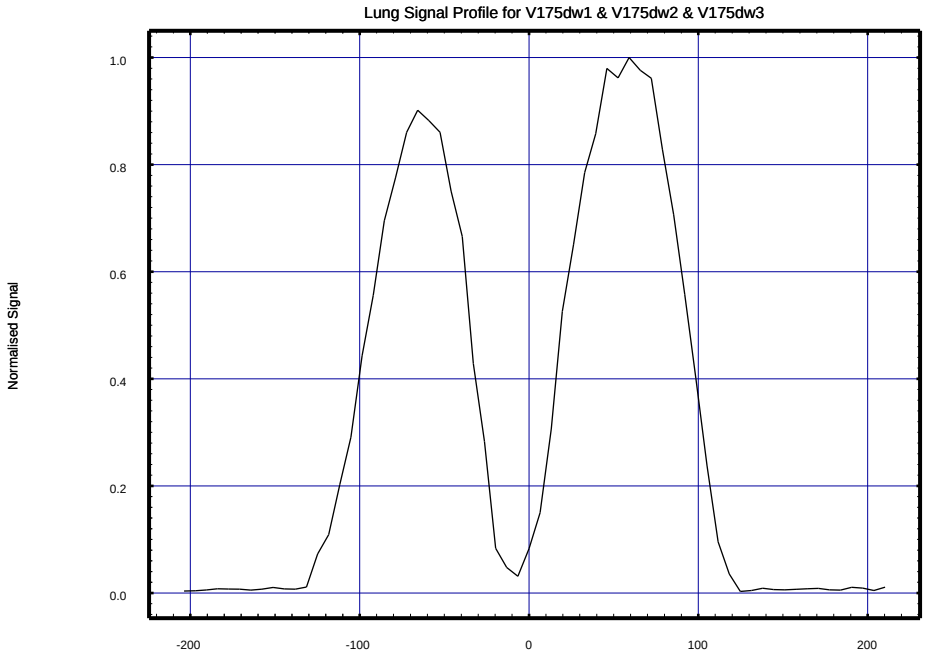

(a) Control Volunteer's Results

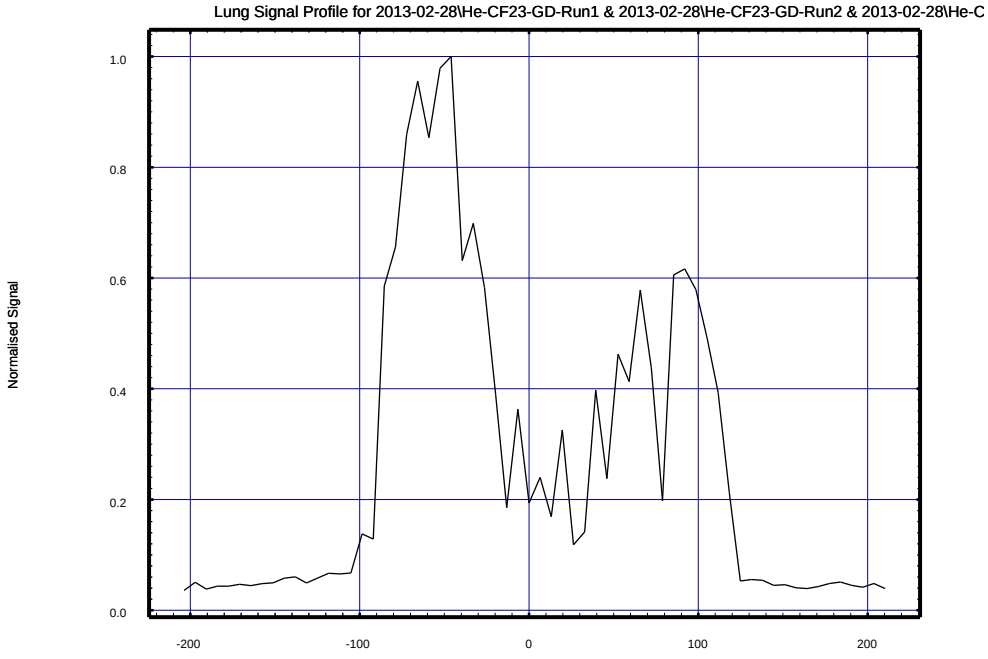

(b) Cystic Fibrosis Volunteer's Results

Figure 67: CPMG ADC Profiles

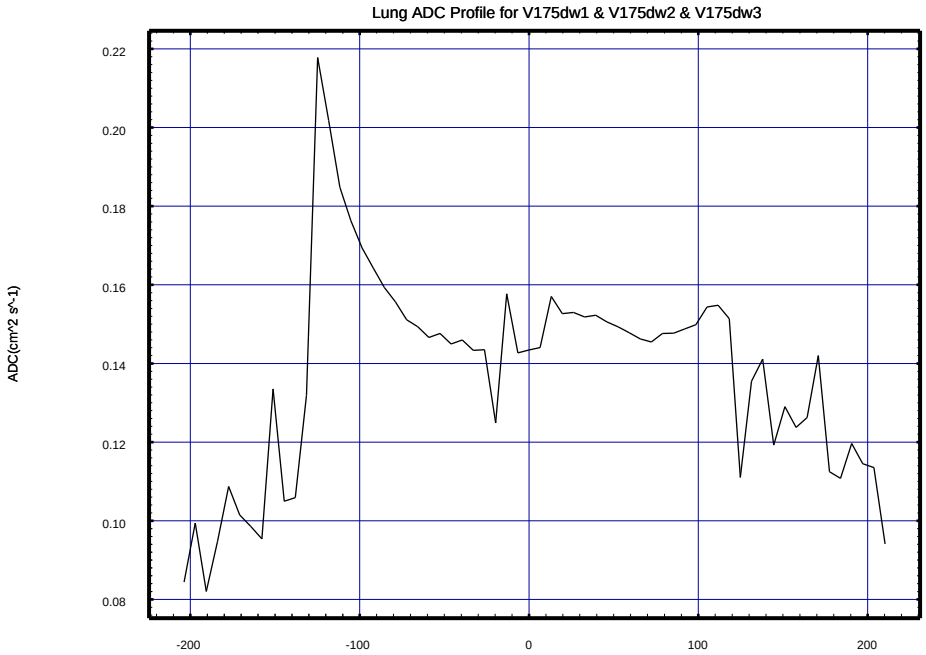

(a) Control Volunteer's Results

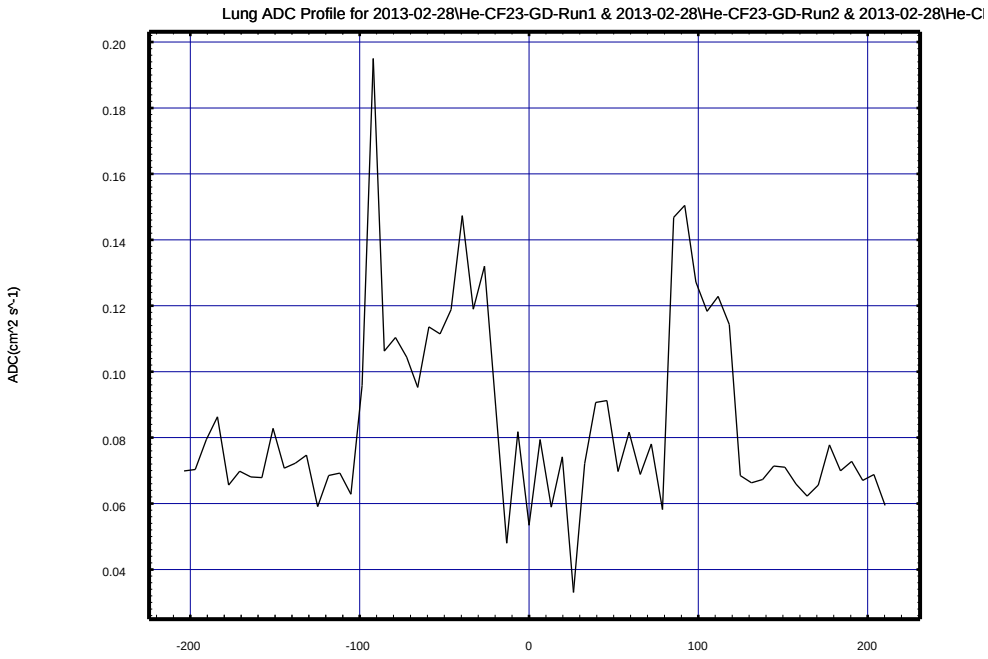

(b) Cystic Fibrosis Volunteer's Results

Figure 68: CPMG Histograms

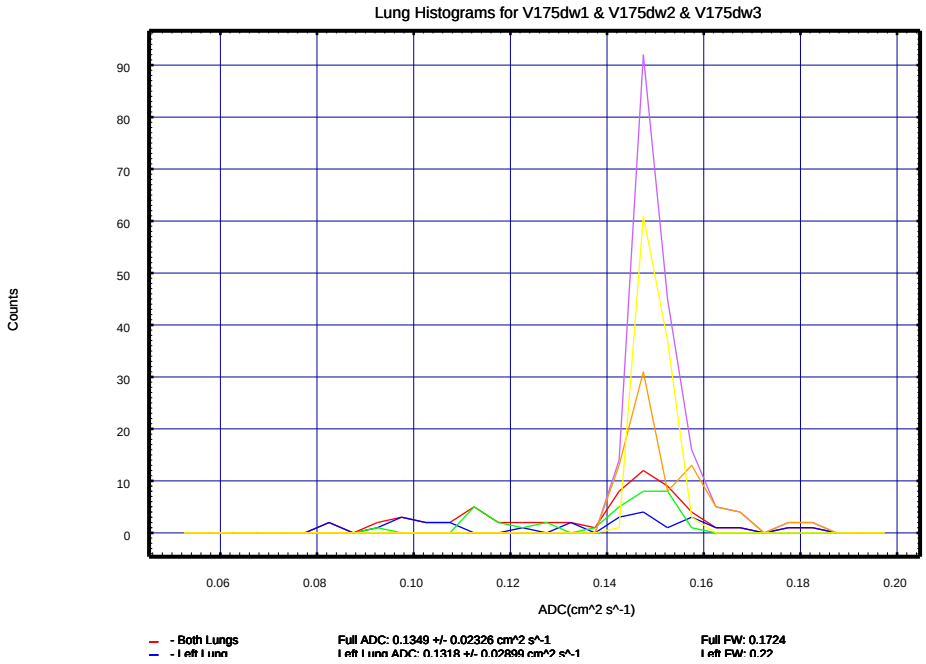

(a) Control Volunteer's Results

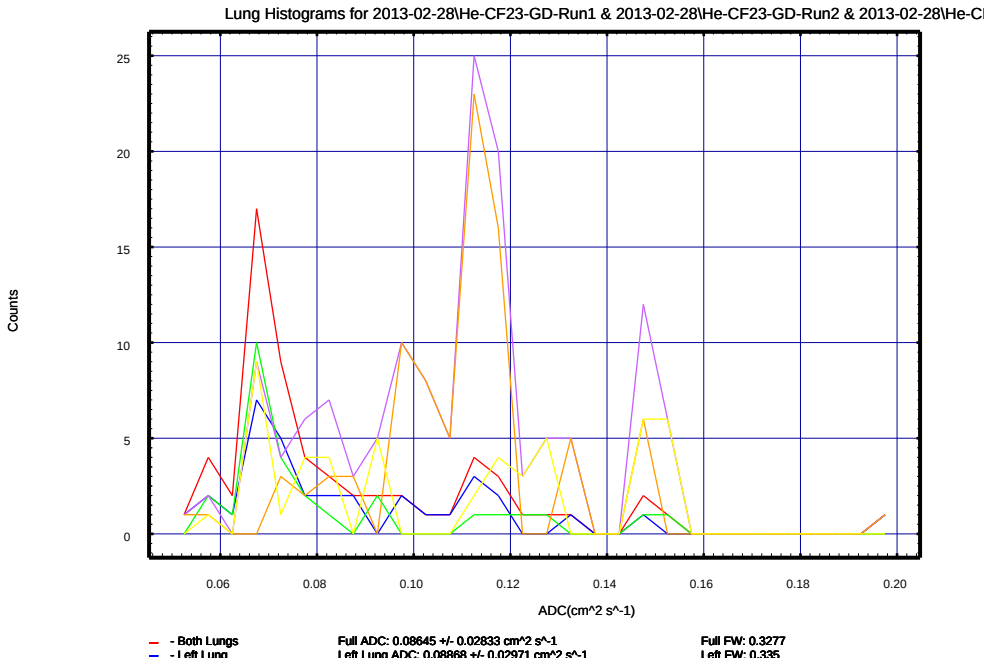

(b) Cystic Fibrosis Volunteer's Results

Figure 69: gADC Signal Attenuation Plots

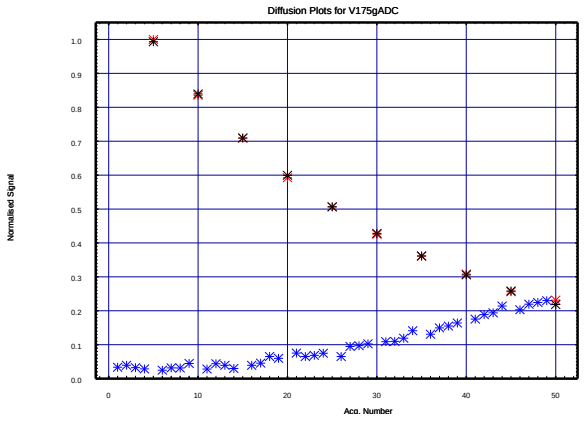

(a) Control Volunteer's Results

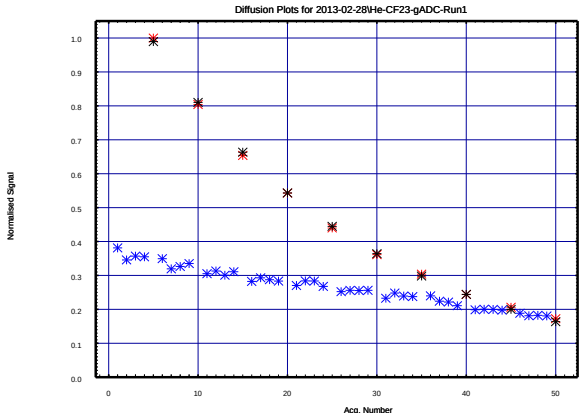

(b) Cystic Fibrosis Volunteer's Results

Figure 70: gADC B-Space Plots

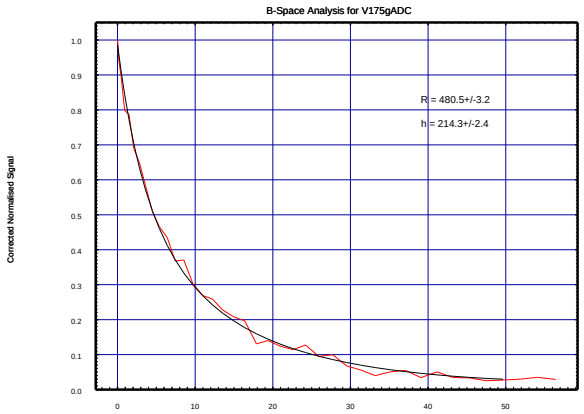

(a) Control Volunteer's Results

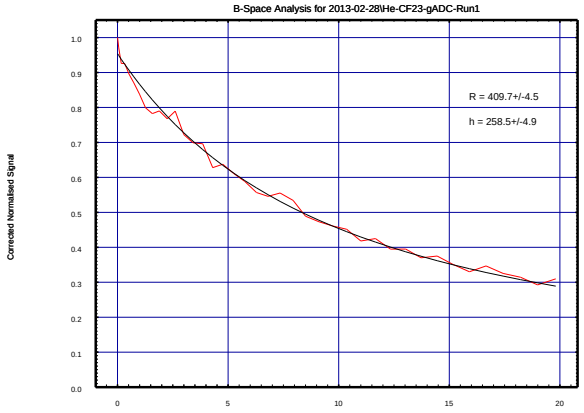

(b) Cystic Fibrosis Volunteer's Results

the control group, but only slightly affects the CF group. It can also be seen that there is a significant difference between the 13 ms ADC values of the healthy and control groups, even after Volume Correction. A slight significant difference in the Yablonskiy fitted R values, but no difference in the Yablonskiy fitted H values.

Table 13: Demographic, Physiological and Magnetic Resonance Data

Showing the mean (standard error) values for each group.

	Healthy Controls	Cystic Fibrosis
No. of Participants	30	18
Age (years)	14.6 (1.4)	14.7 (2.3)
Sex (% male)	50.0	44.4
Height (cm)	151.3 (3.5)	145.0 (5.1)
Weight (kg)	49.9 (3.9)	43.8 (4.6)
FEV_1 (L)	2.7 (0.22)$^{\#\#\#\#}$	1.8 (0.14)$^{\#\#\#\#}$
FEV_1 (% pred.)	101.7 (1.9)$^{\#\#\#\#}$	79.0 (5.2)$^{\#\#\#\#}$
FVC (L)	3.03 (0.27)$^{\#}$	2.35 (0.21)$^{\#}$
FEV_1/FVC	0.895 (0.029)$^{\#\#\#\#}$	0.762 (0.020)$^{\#\#\#\#}$
RV/TLC	28.2 (1.0)$^{\dagger\#\#\#\#}$	39.7 (2.8)$^{\#\#\#\#}$
LCI (L)	7.0 (0.23)$^{\#\#\#\#}$	11.4 (0.35)$^{*\#\#\#\#}$
S_{acin} (L^{-1})	-	0.169 (0.035)*
13 ms ADC (cm^2s^{-1})	0.133 (0.003)$^{\#\#\#}$	0.116 (0.005)$^{\#\#\#}$
13 ms ADC (W) (cm^2s^{-1})	0.133 (0.003)$^{\#\#\#}$	0.115 (0.005)$^{\#\#\#}$
13 ms ADC (VC) (cm^2s^{-1})	0.143 (0.004)$^{\#\#}$	0.129 (0.005)$^{\#\#}$
13 ms ADC (VC W) (cm^2s^{-1})	0.143 (0.004)$^{\#\#}$	0.127 (0.005)$^{\#\#}$
H (μm)	237 (6)	245 (7)‡
R (μm)	457 (9)$^{\#\#}$	431 (8)$^{\ddagger\#\#}$

† Only taken on 29 participants.
$*$ Only taken on 17 participants.
‡ Only collected on 14 participants.
Trends and significant differences between groups denoted:
$^{\#}(p < 0.1)$, $^{\#\#}(p < 0.05)$, $^{\#\#\#}(p < 0.01)$, $^{\#\#\#\#}(p < 0.001)$.

Figure 71: Box Plot of the 13 ms ADC and R-H Values for Control and Cystic Fibrosis Groups

(a) CPMG ADC Values at 13 ms.

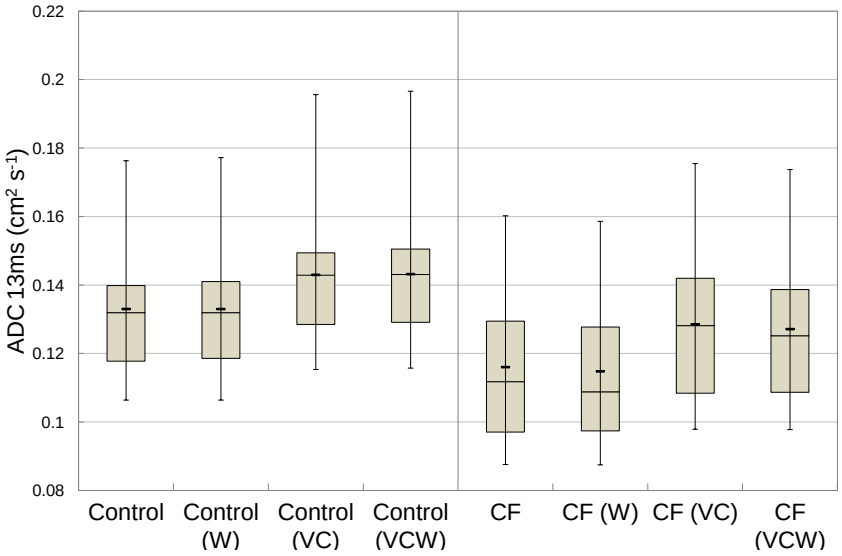

(b) gADC Yablonskiy fitted R and H values.

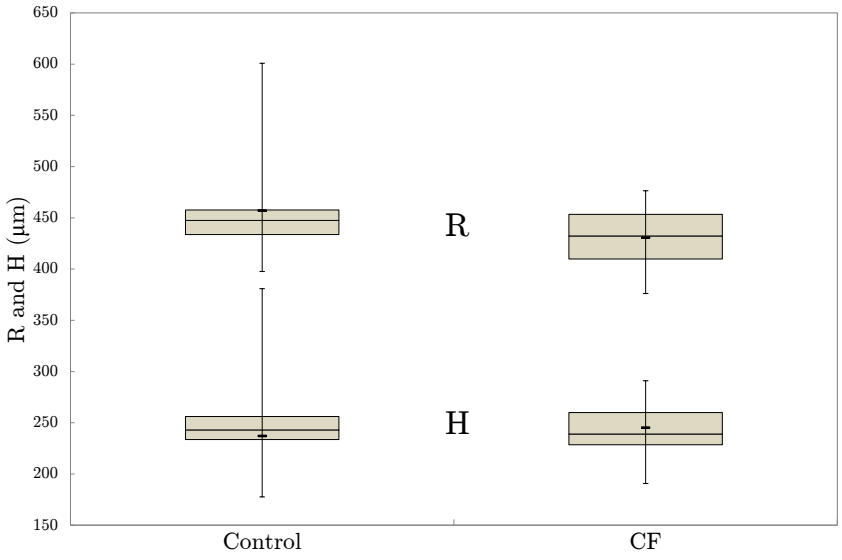

6.4.3 Comparison of Physiological and Magnetic Resonance Data

Table 14 and Figures 72 to 77 show that there is very little or no significant correlation between the ^{3}He-MRI results and the clinical physiological data. A slight correlation is seen between Age and the R/H values for the Control group, but that correlation is not seen in the CF group.

Table 14: Pearson Correlation Values and p-values

	13 ms ADC (VC W)		R‡		H‡	
against	Control	CF	Control	CF	Control	CF
LCI	r=0.17, p=0.39	r=-0.13, p=0.61	r=0.06, p=0.72	r=-0.15, p=0.61	r=-0.04, p=0.83	r=0.12, p=0.69
Age	r=-0.11, p=0.56	r=0.45, p=0.06	r=0.66, p=8x10^{-5}	r=0.31, p=0.27	r=-0.61, p=0.0003	r=-0.35, p=0.22
FEV_1	r=0.30, p=0.11	r=-0.39, p-0.11	r=-0.26, p=0.16	r=-0.44, p=0.08	r=0.21, p=0.25	r=0.52, p=0.06
13 ms ADC (VC W)	-	-	r=0.19, p=0.33	r=0.74, p=0.002	r=-0.23, p=0.24	r=-0.70, p=0.005

‡ Only collected on 14 of the 18 CF participants.

Figure 72: Scatter Graph of 13 ms ADC (VC W) against FEV_1.

CPMG "Global Volume-corrected and Weighted" ADC at 13 ms plotted against FEV_1 (% predicted) for both Control and Cystic Fibrosis subjects.

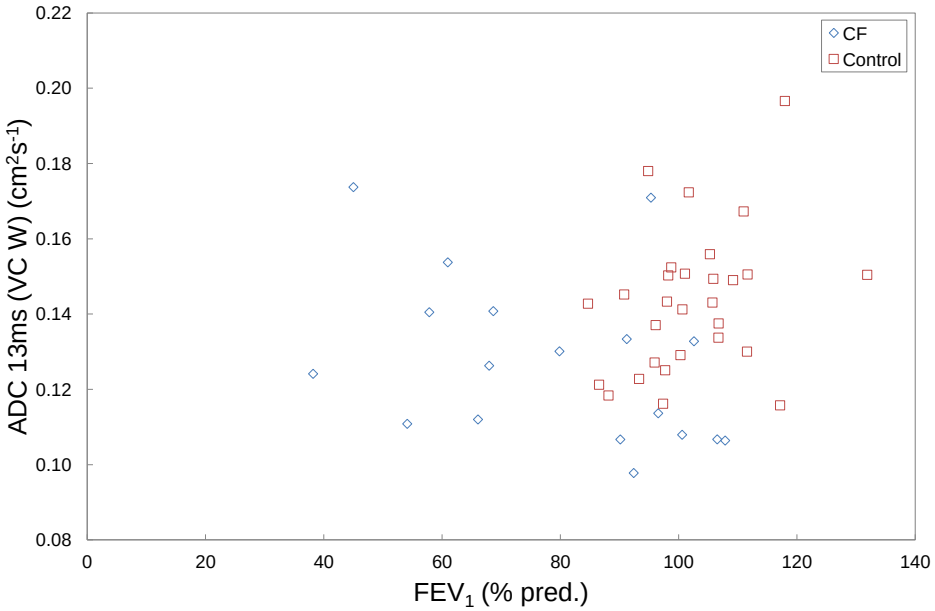

Figure 73: Scatter Graph of 13 ms ADC (VC W) against Age.

CPMG "Global Volume-corrected and Weighted" ADC at 13 ms plotted against Age for both Control and Cystic Fibrosis subjects.

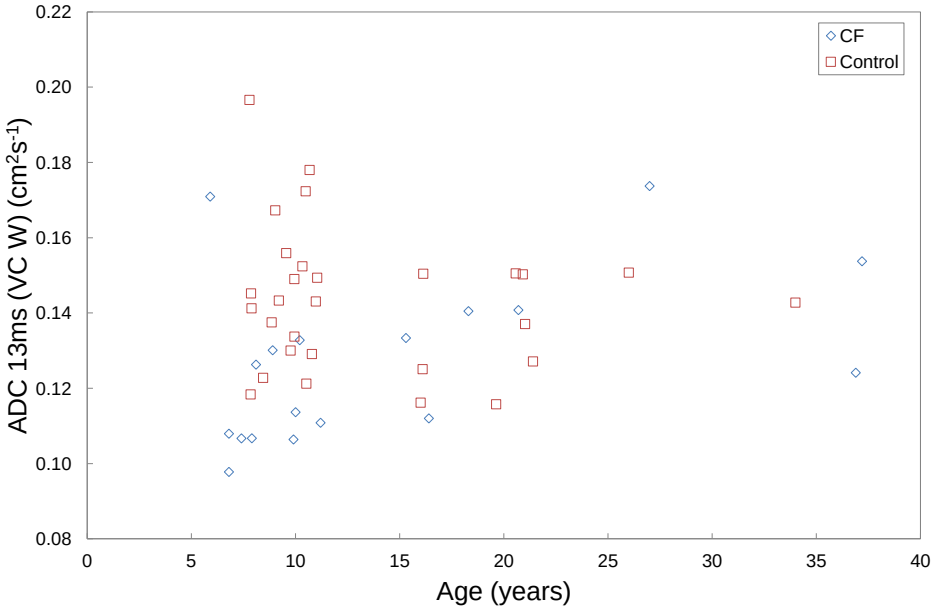

Figure 74: Scatter Graph of 13 ms ADC (VC W) against LCI.

CPMG "Global Volume-corrected and Weighted" ADC at 13 ms plotted against LCI for both Control and Cystic Fibrosis subjects.

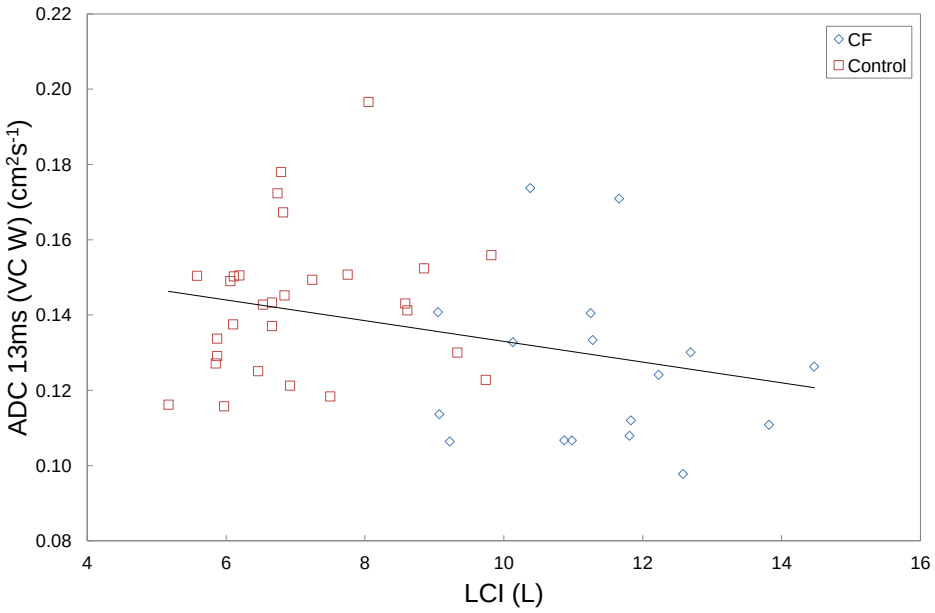

Figure 75: Scatter Graph of Calculated R and H against FEV_1.

Yablonskiy Calculated R and H plotted against FEV_1 (% predicted) for both Control and Cystic Fibrosis subjects.

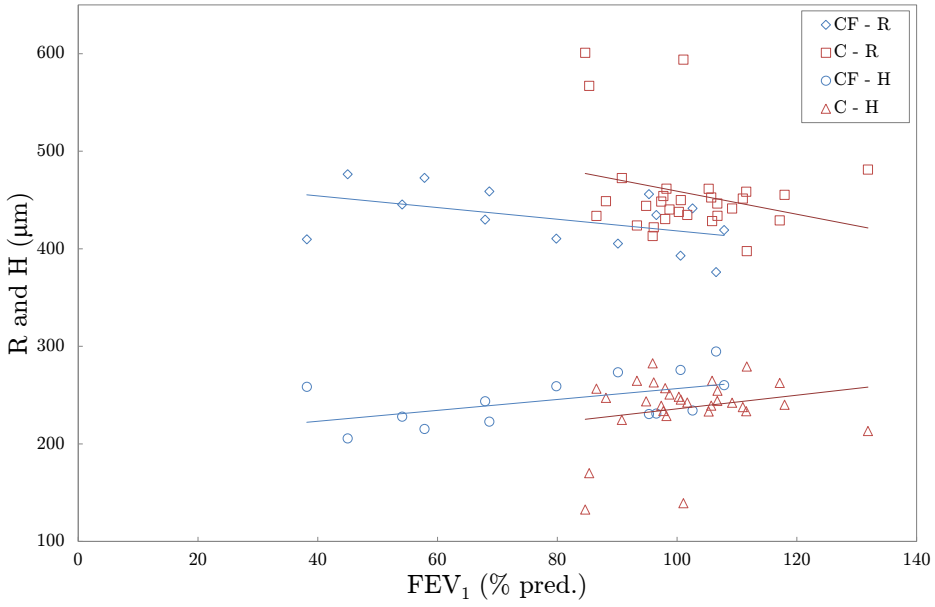

Figure 76: Scatter Graph of R and H against Age.

Yablonskiy Calculated R and H values plotted against Age for both Control and Cystic Fibrosis subjects.

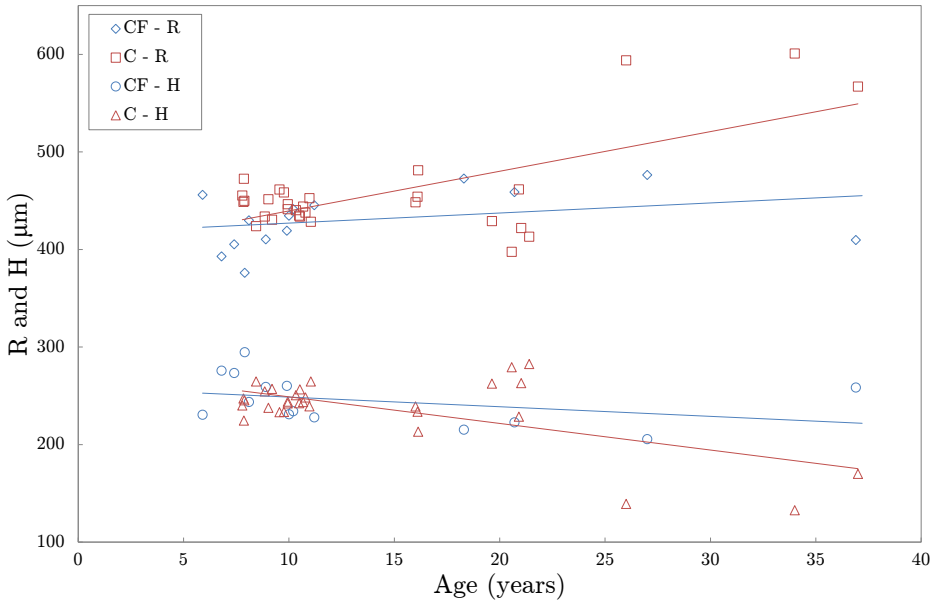

Figure 77: Scatter Graph of R and H against LCI.

Yablonskiy Calculated R and H plotted against LCI for both Control and Cystic Fibrosis subjects.

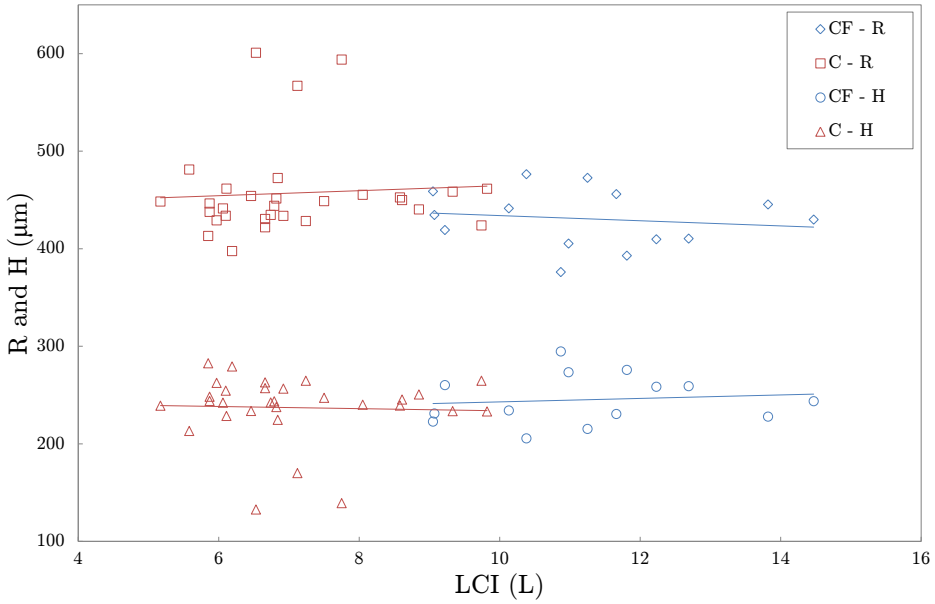

6.5 Discussion

Short time-scale ADC is mainly sensitive to changes in acinar airway radius. An increase in the acinar airway radius reduces the restriction to the transverse displacement of the ^{3}He and results in an elevated ADC. This study found a slight significant decrease in the short time-scale ADC in patients with Cystic Fibrosis, suggesting a decrease in the acinar airway radius, which is consistent with the concept of infection and inflammation occurring in the small airways [3]. However it is not enough to entirely distinguish between a healthy and Cystic Fibrosis volunteer.

The parameters R and H from the Yablonskiy model represent the acinar airway radius (R) and the alveoli width (H). This study found no significant difference in R or H between the patients with Cystic Fibrosis and the healthy controls. However it does show a significant association with a short time-scale ADC, as expected, but only in the CF patients. It also found a significant association between the Age of the healthy controls and the R and H parameters, which suggests a broadening of the acinar airway over time in adults. However, this pattern is not confirmed in the short time-scale ADC result, which does not show a significant increase of ADC with age.

6.6 Potential Limitations

Recently there has been some criticism over the timescales used with the Yablonskiy model [67]. It is suggested that the model is not valid for diffusion times greater than 2 ms, and these longer timescales may overestimate

airway dimensions with a bias that increases with the diffusion time.

Another limitation is seen in the results of the 13ms ADC values. The weighting affects the results of the asthma groups more than the control groups. This may be due to the weighting suppressing areas with low amounts of helium, which may correspond to areas of low ventilation (i.e areas of pathology). This should be investigated further before any conclusions can be drawn.

6.7 Conclusions

In conclusion, this study shows that short time-scale ADC decreases in patients with Cystic Fibrosis, although it cannot be used to distinguish between healthy volunteers and Cystic Fibrosis patients. Additionally, no strong correlations were found between the measurements taken via standard lung function tests (e.g. spirometry and body plethysmography) and the measurements taken via hyperpolarised ^{3}He diffusion MR.

The results also show that the R and H parameters are inconsistent, which suggests that the model may not have been implemented correctly. This concurs with the recent criticism of the model [67] when used with diffusion times greater than 2 ms, as was used in this study. Future studies are required, with various diffusion timescales both less than and greater than 2 ms, to determine if the model is valid.

The affect of signal weighting on the short time-scale ADC values should also be investigated further, to understand whether this step is beneficiary in reducing the spread and error in the CF group, or whether it negatively affects the results by suppressing areas of pathology.

7 ^{129}Xe Development

7.1 Background

For functional lung imaging using hyperpolarised gas MRI, the prime imaging agent of choice for most researchers has been ^{3}He rather than ^{129}Xe [68]. The predominant reason for this preference is due to the stronger signals attainable using ^{3}He, as it can achieve higher levels of polarization and has a higher gyromagnetic ratio. Other reasons include the lack of anaesthetic effects and the ease of access for researchers due to the availability of polarisers (USA) or ease of gas transport (Europe).

However the rise in cost of ^{3}He due to its limited supply coupled with the falling costs of ^{129}Xe and its unlimited natural supply has lead to many researchers agreeing that ^{129}Xe will ultimately emerge as the imaging agent of choice. This shift has already been reflected with recent implementation of new ^{129}Xe studies and polarisers [1, 25, 54, 103].

Alongside the cheaper cost of ^{129}Xe, it also has other benefits over ^{3}He. It is more robust once polarised, meaning the polarisation takes longer to decay. It also has a slower diffusion time, making diffusion weighted measurements easier to perform. Another benefit is that it is readily absorbed through the porous membranes of the lungs into the bloodstream. This allows for gas transfer studies, as well as dissolved-phase imaging of both the lungs and the brain. However ^{129}Xe is slightly toxic, having an anaesthetic effect on the human body, so more care must be taken when performing experiments involving human volunteers.

7.2 Objectives

The main aim of this pilot study is to develop the scan sequences, protocol and gas delivery in order to get MRI images of the human lungs that are of a high standard, ready for future Clinical studies. The main focus was on single ventilation images and dynamic ventilation images. A secondary stage of this study is to develop diffusion weighted imaging sequences, and dissolved-phase spectroscopy/imaging sequences.

7.3 Method

This was a collaborative study, with contributions from the following people:

This was a collaborative study, with contributions from the following people:

- Prof. Ian P Hall - Designed the study. Principal Investigator.
- Dr. Shahideh Safavi - Screened and volunteers. Performed clinical monitoring of patients during scan visits.
- Sarah Wolfe - Recruited and screened volunteers. Performed clinical monitoring of patients during scan visits.
- Dr Michael J Barlow - Qualified Manufacturer (QM). Produced $^{1}29$Xe polarised gas.
- Dr Brett Haywood - Qualified Assurer (QA) for $^{1}29$Xe polarised gas. Helped during performance of MRI scans.

- Dr Arthur Hill - Qualified Person (QP). Responsible of cerfying each batch of $^{1}29$Xe polarised gas.

- James Thorpe - Assisted in performance of MRI scans. Will be performing future MRI scans, as well as future raw data analysis and results analysis.

- Steven Hardy - Performed MRI scans. Created broad-banded sequences. Performed raw data analysis. Performed analysis on results.

MHRA approval was granted for the Hyper-polariser system (EudraCT: '2013-004336-30', CTA: '03057/0061/001-0001') and and ethical approval was granted for the pilot study by the NRES Committee (East Midlands, Nottingham 2 Research Ethics Committee, NRES Ref: '13/EM/0401'). Only healthy subjects were recruited for the initial pilot stage. Before the first scanning visit, each volunteer was subject to a screening visit, to determine their suitability for the study. This screening visit included Spirometry lung function tests.

For each MRI scan visit (up to 4 visits in total per participant), the participant underwent up to 4 scans, consisting of proton localiser and co-registration sequences, followed by a single hyper-polarised ^{129}Xe imaging sequence. Initially the hyperpolarised ^{129}Xe imaging scans were performed using the bb2dfast sequence, however a Software update on the MRI scanner required a new sequence to be designed (bbfgre) which was then used for the rest of the scans performed so far.

Tedlar bags of either 0.6 L or 1.0 L of hyperpolarised gas were produced for each scan using a GE 2000 Xe-Rb continuous flow polariser, with a gas mixture of 2% naturally abundant Xe / 10% N_2 / 80-87% ^{4}He. The hyperpolarised gas MRI was performed in a GE 1.5T Signa HDx MRI scanner, using a RAPID biomedical 8-channel ^{129}Xe chest coil. The typical polarisation levels measured in the delivered bag was in the region of 8-12%.

7.4 Sequence Development

7.4.1 Flip-Angle Calibration

Usually the testing and calculation of the transmit gain necessary to achieve the specific flip angles required by a scan is handled by the auto-prescan functionality of the GE scanner. However, the use of the auto pre-scan is undesirable for the Xenon scans. This is due to both the time constraint of a breath-hold imaging (the auto-prescan can often take up to a minute to complete), and the non-recoverable nature of the hyperpolarised gas (each rf pulse reduces the amount of signal available for the next rf pulse). Instead, the transmit gain / flip angle relationship must be calculated beforehand for each sequence.

To establish the transmit gain / flip angle relationship, the sequences were performed multiple times on many bags of hyperpolarised ^{129}Xe (alongside $\sim$20 kg of saline bags to load the coil). The sequences were performed with the gradients turned off, and for a minimum of 64 RF excitations with 1 s spacing applied. T_1 decay was assumed to be negligible for this short a

time interval, meaning the signal S decays by:

$$S = S_0 cos(\alpha)^{n-1}, \tag{57}$$

where S_0 is the initial signal, n is the excitation pulse index and α is the flip angle. Using a non-linear least squares best fit algorithm, the flip-angle can be calculated from the data (see Figure 78).

Figure 78: Flip Angle Measurement Examples

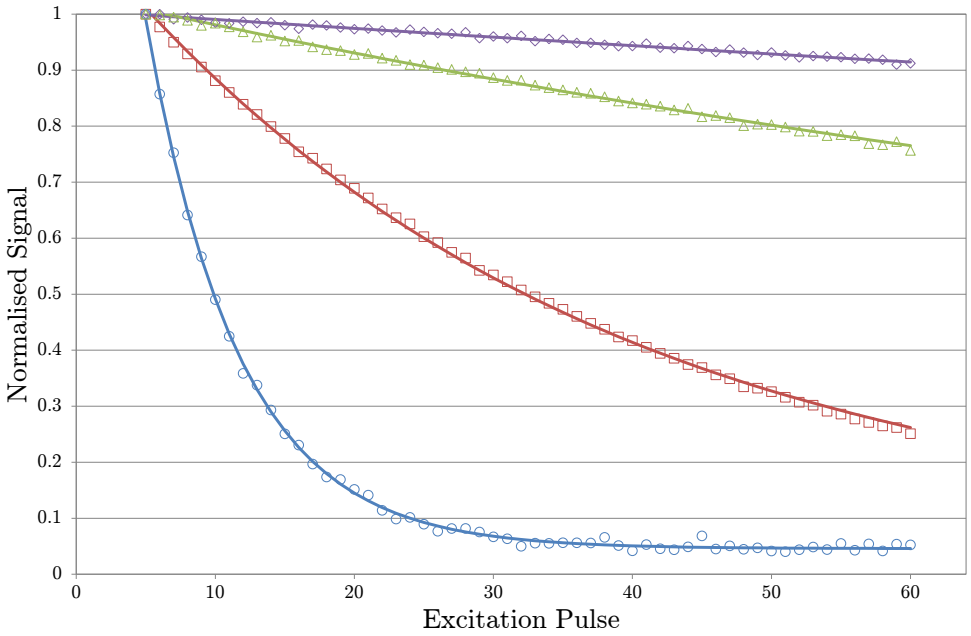

Example data collected for flip angle calibration, along with the calculated best fit lines. Starting from the top-most line, the calculated flip angles are: 4.0°, 7.3°, 13.6°, and 30.9°.

This process was repeated multiple times for each sequence, at varying transmit gain settings, to establish the relationship between transmit gain and flip angle. The results are shown in Figure 79. As can be seen each scan routine has a different flip angle / transmit gain relationship. This is due to the different sequences making use of various shapes and lengths of

rf pulses. Using these results, the appropriate transmit gain can be found for any desired flip angle for any of the sequences, allowing the sequence to be prepared without the use of the auto-prescan.

Figure 79: Measured Flip Angle against Transmit Gain.

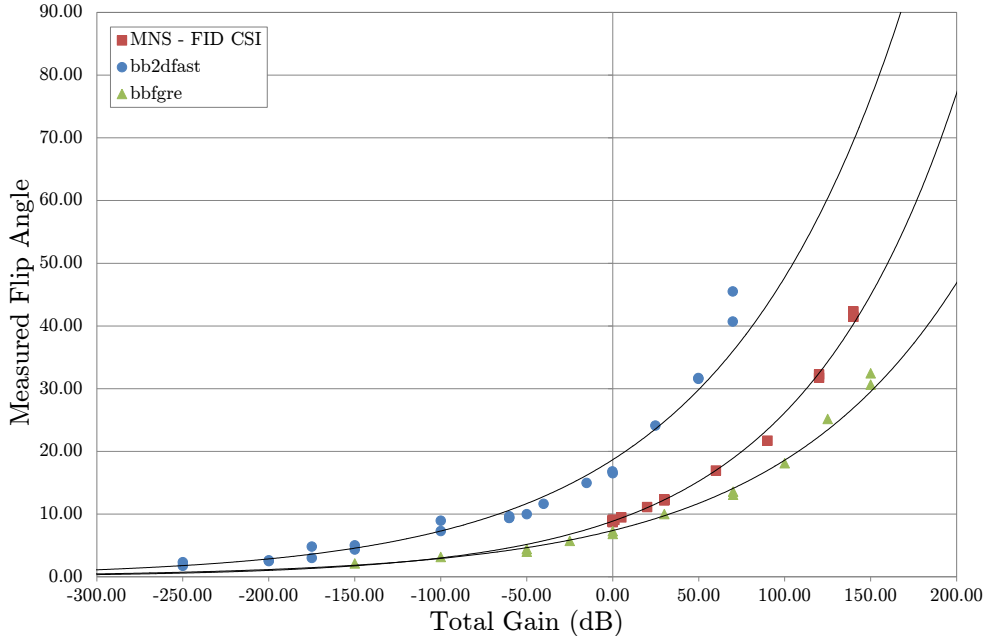

The flip angle for the greatest signal-to-noise is different for hyperpolarised MRI than it is for normal proton MRI. Due to the non-recoverable nature of hyperpolarised MRI, each subsequent excitation produces less signal than the previous. For the best signal-to-noise, a strong signal is required at the centre of k-space. If the sequence is taken centre-out (as for bbfgre), this is not a problem and much larger flip angles can be used. However if the sequence is taken sequentially (as for bb2dfast), a much smaller flip angle must be used, to preserve as much of the signal as possible for the centre of k-space. Figure 80 shows the theoretical maximum signal available for each excitation for various flip angles. From this a flip angle of 5.5° was chosen

for bb2dfast to give the most signal at the centre of k-space (64 acquisitions).

Figure 80: Normalised Signal against Excitation Number for Various Flip Angles

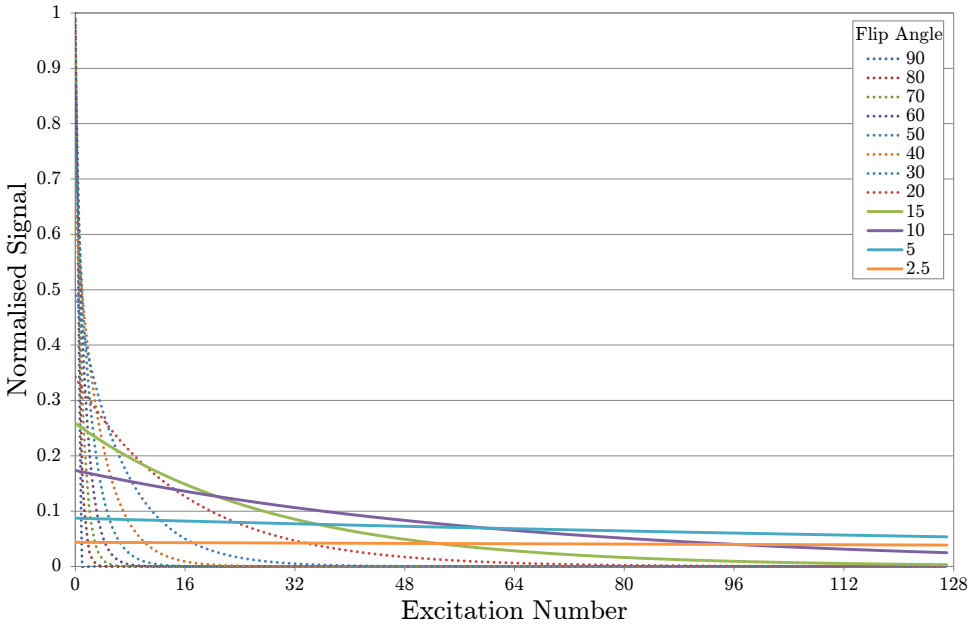

A graph showing the theoretical measurable signal against excitation number, for various Flip Angles. Assuming negligible T_1 and T_2 decays.

7.4.2 Measuring the Signal-to-Noise Ratio

One way to compare the relative quality of the MRI images is to compare the raw data's Signal-to-noise ratio (SNR). The signal to noise ratio can be calculated using the following equation:

$$SNR = \left(\frac{A_{signal}}{A_{noise}}\right)^2, \tag{58}$$

where A is the root mean square (RMS) amplitude over an area of interest, in this case the signal and noise areas. The RMS amplitude for an area of

interest can be calculated as:

$$A = \sqrt{\frac{1}{n}(\sum_{i=1}^{n} S_i^2)} \tag{59}$$

where n is the number of points in the area of interest, and S is the signal strength of each point. The area of interest for the signal of each set of raw data is the middle half of each of the acquisitions, with the area of interest for noise being the rest of the data. Figure 81 shows the areas of interest using an example acquisition.

Figure 81: Sample Acquisition, Highlighting Noise and Signal Areas

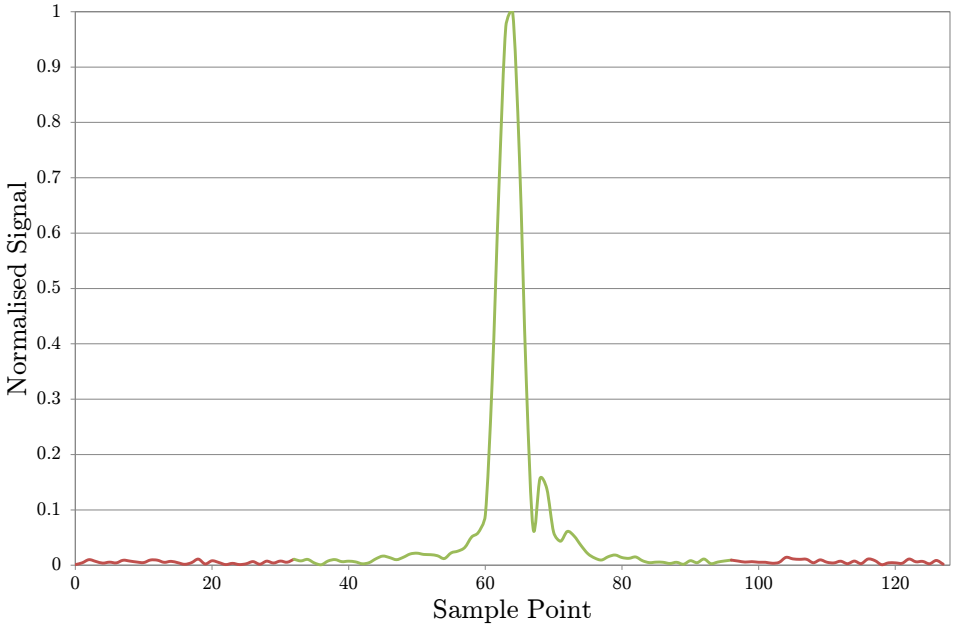

A graph showing a single example acquisition, with the area-of-interest for noise highlighted red, and the area-of-interest for signal highlighted green.

7.4.3 Initial Images

The first initial images were taken using the bb2dfast sequence, inherited from The University of Sheffield. During this stage, it was important to get the brightest image possible for proof-of-concept, and as such the majority of the scans were implemented with the slice gradient turned off, so that the whole of the lungs is excited with each rf pulse. The initial images were taken in both axial (Figure 82) and coronal planes (Figure 83).

Figure 82: Initial Axial Lung Images

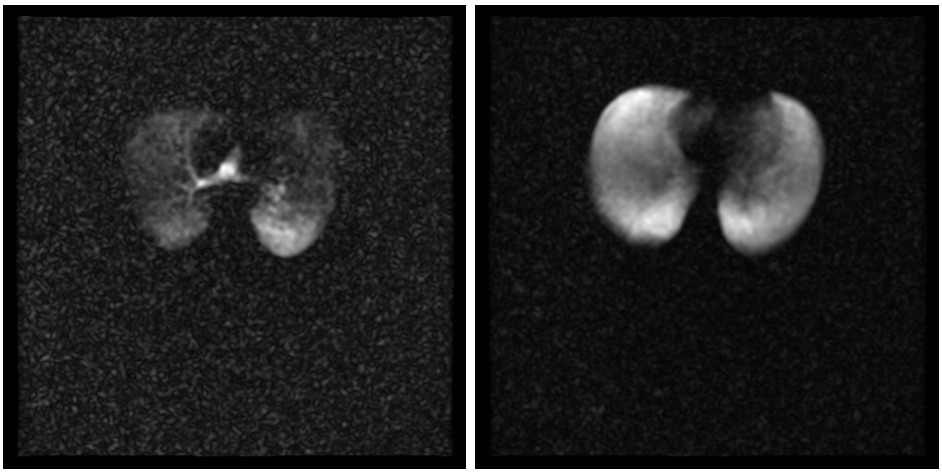

(a) Gas partially inhaled before scan start.

(b) Gas inhaled fully before scan start.

Axial In-Vivo images taken using the bb2dfast sequence, with the slice gradient switched off, on the same healthy volunteer, using a 0.6 L bag of ∼10% polarised ^{129}Xe gas. FOV = 48 cm, Res = 128x128, Te = 4.2 ms, Tr = 9 ms, Flip Angle = 5.5°. Raw SNR Left Image: 1.4, Right Image: 7.02

Figure 83: Initial Coronal Lung Image

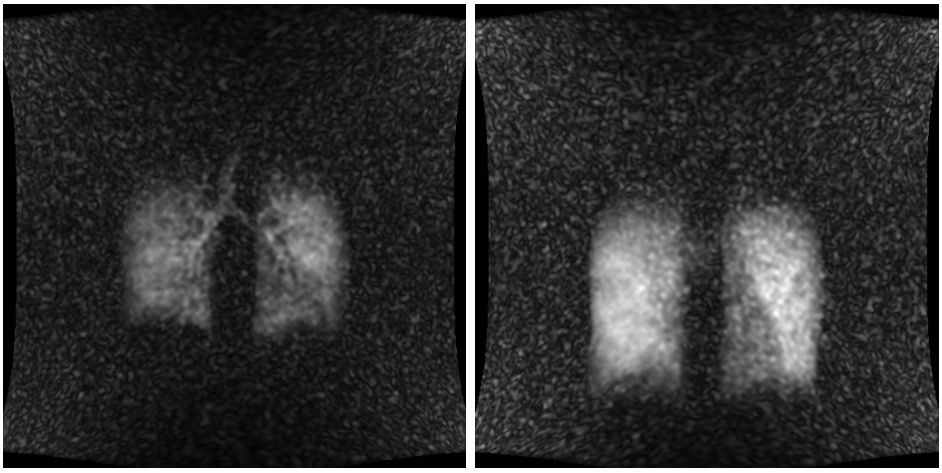

(a) Gas partially inhaled before scan start.

(b) Gas inhaled fully before scan start.

Coronal In-Vivo images taken using the bb2dfast sequence, with the slice gradient switched off, on a healthy volunteer, using a 0.6 L bag of ∼10% polarised ^{129}Xe gas. FOV = 48 cm, Res = 128x128, Te = 4.2 ms, Tr = 9 ms, Flip Angle = 5.5°. Raw SNR Left Image: 1.55, Right Image: 2.28

7.4.4 New Sequence Images

The new sequence bbfgre differs from the initial sequence bb2dfast in a few aspects, but the one of main importance is that it takes the k-space acquisitions from the centre-out. This allows use of much larger flip angles, and hence delivers a higher signal-to-noise ratio. Figure 84 shows a comparison of the two sequences.

Figure 84: Sequence Comparison Images

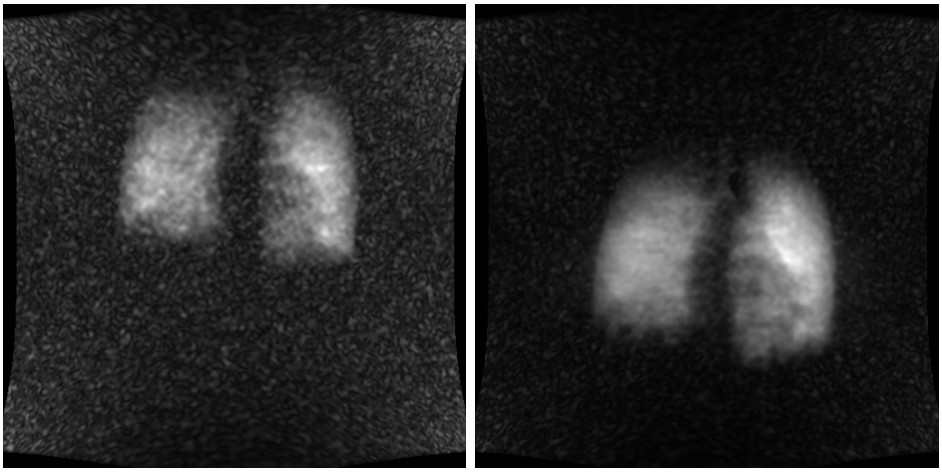

(a) bb2dfast Sequence (b) bbfgre Sequence

Coronal In-Vivo images taken using the bb2dfast and bbfgre sequences, with the slice gradient switched off, on the same healthy volunteer, using a 1 L bag of ∼5.6% and ∼5.9% polarised ^{129}Xe gas respectively. bb2dfast: FOV = 48 cm, Res = 128x128, Te = 4.2 ms, Tr = 9 ms, Flip Angle = 5.5°. bbfgre: FOV = 48cm, Res = 128x128, Te = 5 ms, Tr = 7.5 ms, Flip Angle = 20°. Raw SNR Left Image: 1.88, Right Image: 7.65

As can be seen in Figure 84, the new bbfgre sequence is considerably brighter than the original bb2dfast sequence. Analysis of the raw data found that the SNR of the bb2dfast image was 1.9, whereas the bbfgre image was 7.7, a 4-fold increase.

7.5 Ventilation Images

7.5.1 Repeatability

In a research setting, an experiment must be repeatable if its results are to be trusted. In a clinical setting, a test must be reliably consistent if it is to be used for diagnosis or exploration. It is therefore important to make sure the sequences could reliable and repeatably get the same results (for the same subjects).

Figure 85: Scan Repeatability (Volunteer 1)

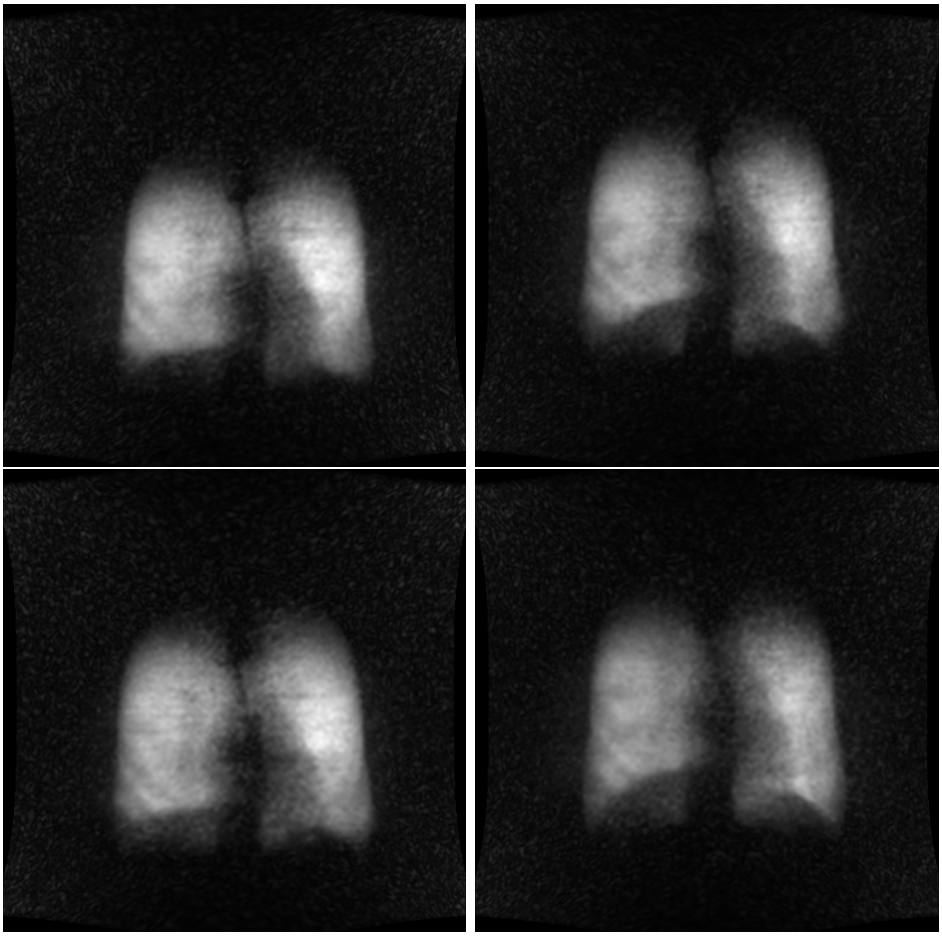

Coronal In-Vivo images taken using the bbfgre sequence, with the slice gradient switched off, on a healthy volunteer over three visits. Top Left scan was taken on the first visit, using 0.6 L of ∼9.0% polarised ^{129}Xe gas, the remaining scans were taken across the other 2 visits, using a 1 L bag of ∼9.6%, ∼9.3%, ∼9.5% polarised ^{129}Xe gas respectively. Scans were started after the volunteer had inhaled the bag and taken a second 'flushing' breath. FOV = 48 cm, Res = 128x128, Te = 5.0 ms, Tr = 7.6 ms, Flip Angle = 20°. Raw SNR Top Left Image: 15.30, Top Right Image: 17.03, Bottom Left Image: 16.67, Bottom Right Image: 13.99.

Figure 86: Scan Repeatability (Volunteer 2)

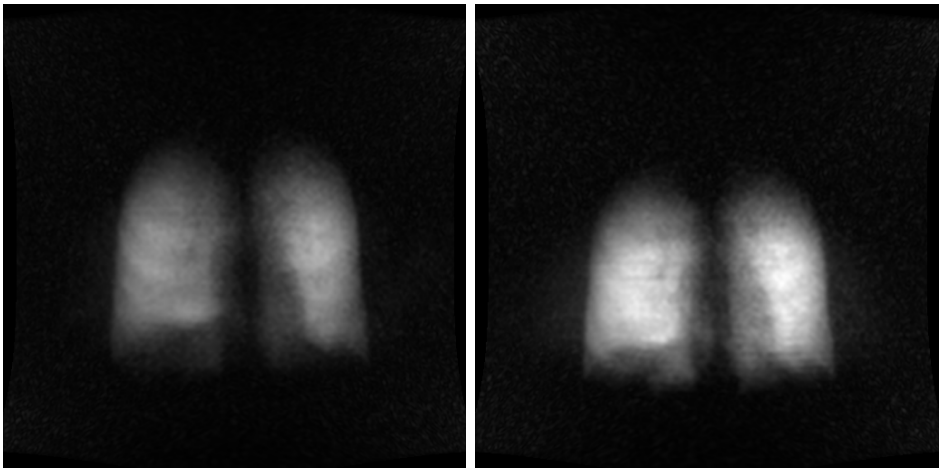

Coronal In-Vivo images taken using the bbfgre sequence, with the slice gradient switched off, on a healthy volunteer over two visits. Left scan was taken on the first visit, using 1 L of ∼7.45% polarised ^{129}Xe gas, the other scan was taken on the second visit, using a 1 L bag of ∼9.8% polarised ^{129}Xe gas. Scans were started after the volunteer had inhaled the bag and taken a second 'flushing' breath. FOV = 48 cm, Res = 128x128, Te = 5.0 ms, Tr = 7.6 ms, Flip Angle = 20°. Raw SNR Left Image: 20.97, Right Image: 34.84.

Figures 85 and 86 shows the results from two different volunteers, both attending multiple visits, undertaking an 'infinite slice' version of bbfgre (i.e. the slice gradient was turned off, so signal was seen from the full thickness of the target).

Four 'infinite slice' scans were taken over the three visits for the first volunteer (Figure 85). As can be seen the images are almost identical, with details such as the 2 shadow lines on the lower part of the patient's right lung (image left) visible in all 4 images. This shadow is likely to be due to the gaps between the different lobes of the lung. Similar SNR values were seen across all four images.

Two 'infinite slice' scans were taken over two visits for the second volunteer (Figure 86). Unlike with the previous volunteer, no matching details can be seen between the two images, other than the overall shape. This may be due to the mis-match in SNR (21.0 vs 34.8), which in turn is most likely a product of the varying ^{129}Xe polarization level between the scans ($\sim$7.45% vs $\sim$9.8%).

Overall there has been some evidence of repeatable image quality (particular in the first volunteers images), however two small a sample size has been collected so far to make any true conclusions.

7.5.2 Finding the Minimum Slice Thickness

The initial scans performed using bb2dfast and bbfgre were taken as 'infinite slice', i.e. the slice gradient was turned off to maximise the SNR. However, for greater information individual sliced images of the lungs are desired. This raises a problem, as the thinner the slice, the less signal there is available to create the image, lowering the SNR. Hence the minimum slice thickness, that still produces usable images, needs to be found.

Figure 87 shows the thickest of the sliced images performed. Each slice was 5.0 cm thick, with a 1.0 cm gap between each slice. The raw data SNR for each image was 13.3, 7.9 and 1.9 respectively. Some detail can be seen at this point (such as the Trachea and Bronchi in the upper right image), however some blur is still visible at the edges, due to the thick slice size. Overall the images are still bright enough to see clearly over the background noise.

Figure 87: Initial Sliced Images - 5 cm Slice Thickness

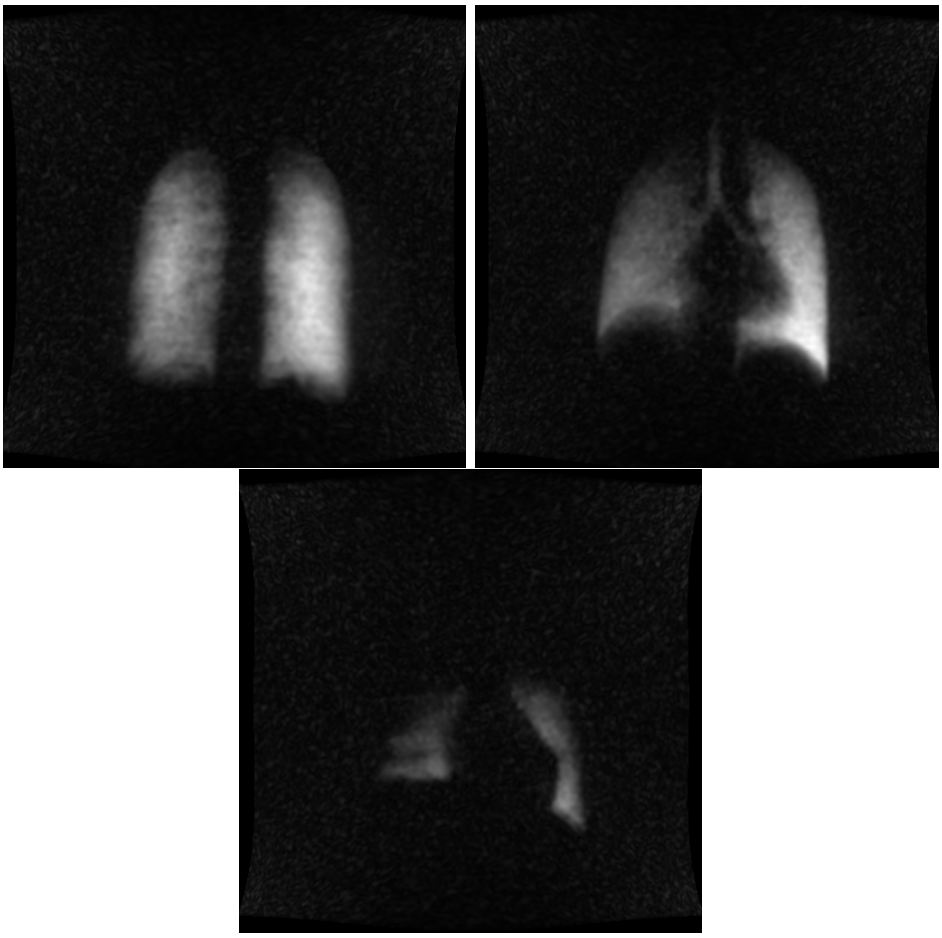

Coronal In-Vivo images taken using the bbfgre sequence, on a healthy volunteer, using a 1 L bag of ∼9.5% polarised ^{129}Xe gas. The scan was started after the volunteer had inhaled the bag. FOV = 48 cm, Slice Thickness/Spacing = 5.0/1.0 cm Res = 128x128, Te = 5.0 ms, Tr = 7.6 ms, Flip Angle = 20°. Raw SNR Top Left Image: 13.29, Top Right Image: 7.93, Bottom Image: 1.89

Figure 88: Initial Sliced Images - 2.5 cm Slice Thickness

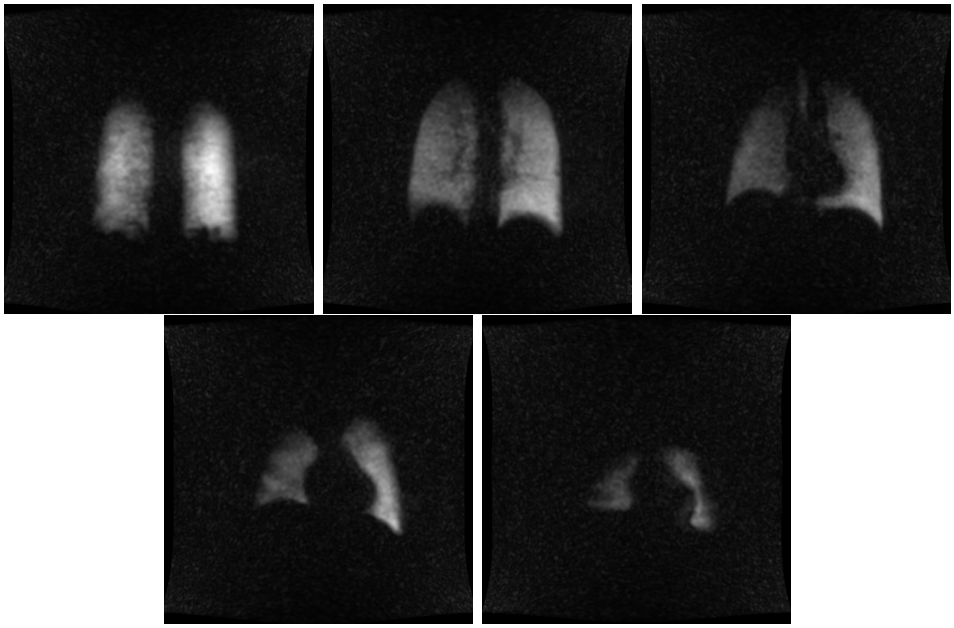

Coronal In-Vivo images taken using the bbfgre sequence, on a healthy volunteer, using a 1 L bag of ∼9.4% polarised ^{129}Xe gas. The scan was started after the volunteer had inhaled the bag. FOV = 48 cm, Slice Thickness/Spacing = 2.5/0.5 cm Res = 128x128, Te = 5.0 ms, Tr = 7.6 ms, Flip Angle = 30°. Raw SNR Top Left Image: 7.69, Top Middle Image: 5.26, Top Right Image: 3.09, Bottom Left Image: 2.63, Bottom Right Image: 1.50.

Figure 88 shows slices of 2.5 cm each, with a 0.5 cm gap between each slice. The raw data SNR for this set was 7.7, 5.3, 3.1, 2.6 and 1.5 respectively. There is a lot more detail seen in these images, such as the shadow due to the major blood vessels visible in the top middle image, the top of the trachea in the top right image, and the shadowing on the lung in the bottom right image (which was most likely due to the gaps between the lobes of the lung). The images are still reasonably bright and visible against the background noise.

Figure 89 shows the thinnest slice thickness performed so far. Each slice was 1.0 cm thick, with a 0.5 cm gap between each slice. The raw data SNR for each image was 2.10, 2.74, 2.14, 1.82, 1.71, 1.63, 1.68, 1.67 and 1.63 respectively (starting top left, left to right). Again detail is visible in these image, such as the upper airways (middle image), major blood vessels (middle left), and impressions from the rib cage (bottom middle and bottom left). The background noise is more prominent in these images, even though the flip angle was increased to 35°. This may be the minimum slice thickness achievable, that is still capable of producing clear enough images.

7.5.3 Proton Co-Registration

Proton co-registration scans were taken alongside some of the ^{129}Xe scans. These co-registration scans were taken just before the ^{129}Xe scans, and consist of the same slice thickness, and slice positions. The volunteers were asked to inhale, to the best of their knowledge, the same amount of room air that they would of ^{129}Xe gas.

Figure 89: Initial Sliced Images - 1.0 cm Slice Thickness

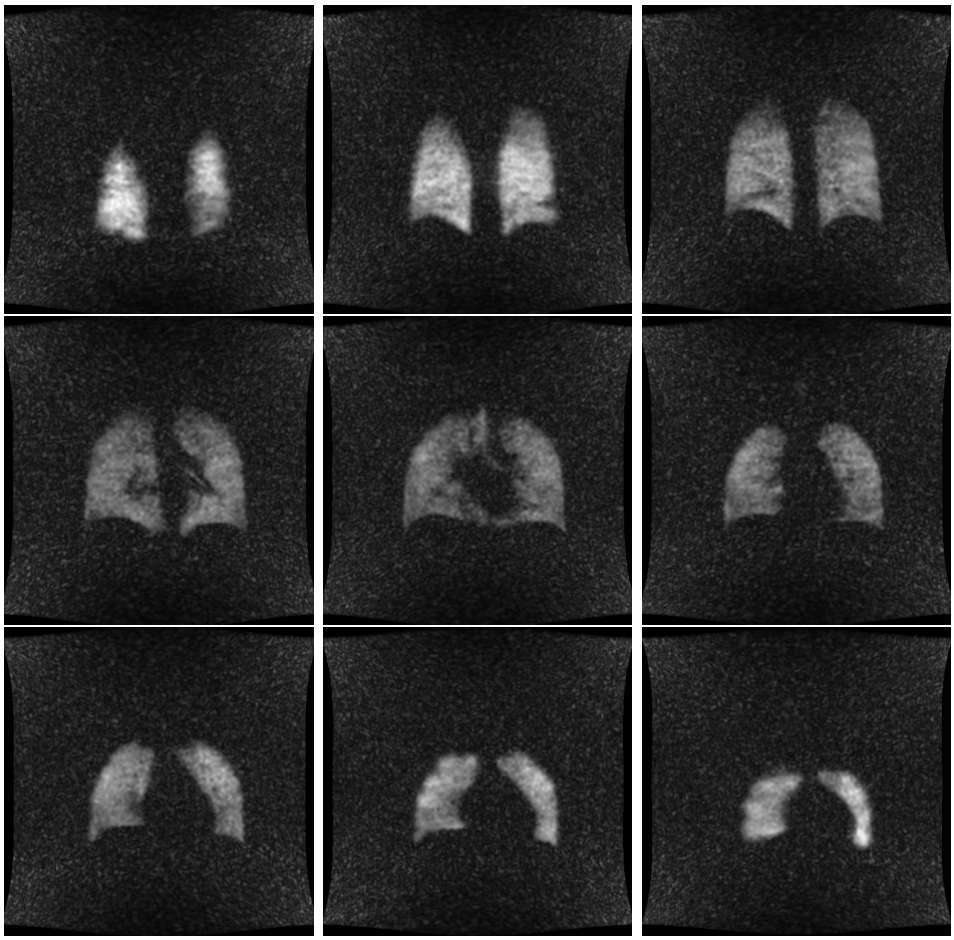

Coronal In-Vivo images taken using the bbfgre sequence, on a healthy volunteer, using a 1 L bag of ∼9.5% polarised ^{129}Xe gas. The scan was started after the volunteer had inhaled the bag. FOV = 48 cm, Slice Thickness/Spacing = 1.0/0.5 cm Res = 128x128, Te = 5.0 ms, Tr = 8.4 ms, Flip Angle = 35°. Raw SNR, Staring from Top Left, across then down: 2.10, 2.74, 2.14, 1.82, 1.71, 1.63, 1.68, 1.67, 1.63.

Figure 90: Xenon-Proton Overlay Images - 2.5 cm Slice Thickness

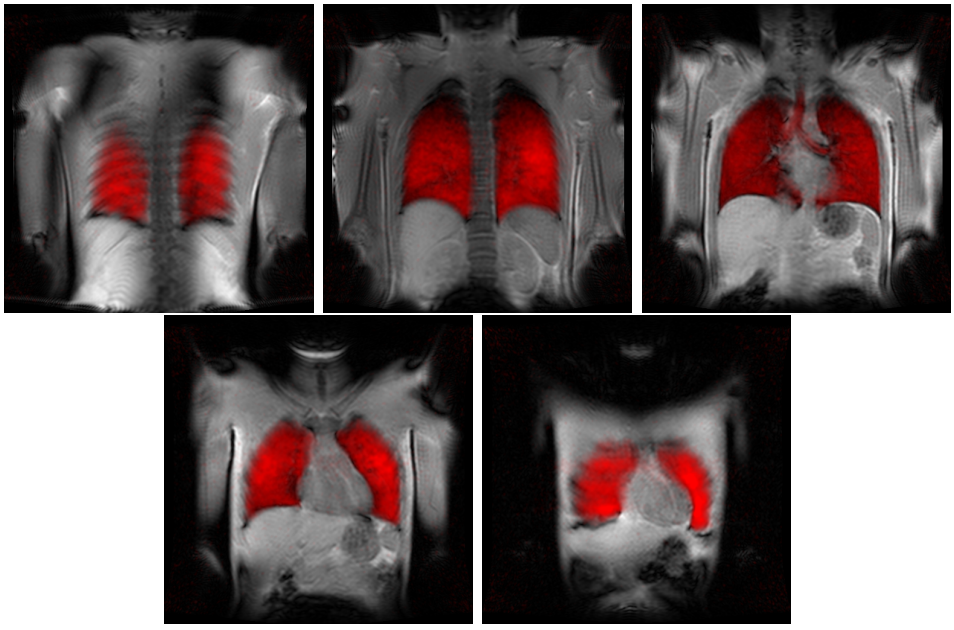

Coronal In-Vivo ^{129}Xe bbfgre scan (alpha-red) overlaid onto a corresponding Proton co-registration scan (black and white).Performed on a healthy volunteer, using a 1 L bag of ∼9.4% polarised ^{129}Xe gas. The ^{129}Xe scan was started after the volunteer had inhaled the bag. Proton Scan: FOV = 48 cm, Slice Thickness/Spacing = 2.5/0.5 cm Res = 128x128, Te = 5.0 ms, Tr = 7.6 ms, Flip Angle = 30°. ^{129}Xe Scan: FOV = 48 cm, Slice Thickness/Spacing = 2.5/0.5 cm Res = 128x128, Te = 5.0 ms, Tr = 60.0 ms, Flip Angle = 30°.

After taking both scans, the proton co-registration scan can then be compared to the ^{129}Xe scan, by overlaying the ^{129}Xe scan images onto the proton co-registration scan images, using a image manipulation programme (such as GIMP). Figures 90 and 91 are two such examples.

Figure 91: Xenon-Proton Overlay Images - 1.0 cm Slice Thickness

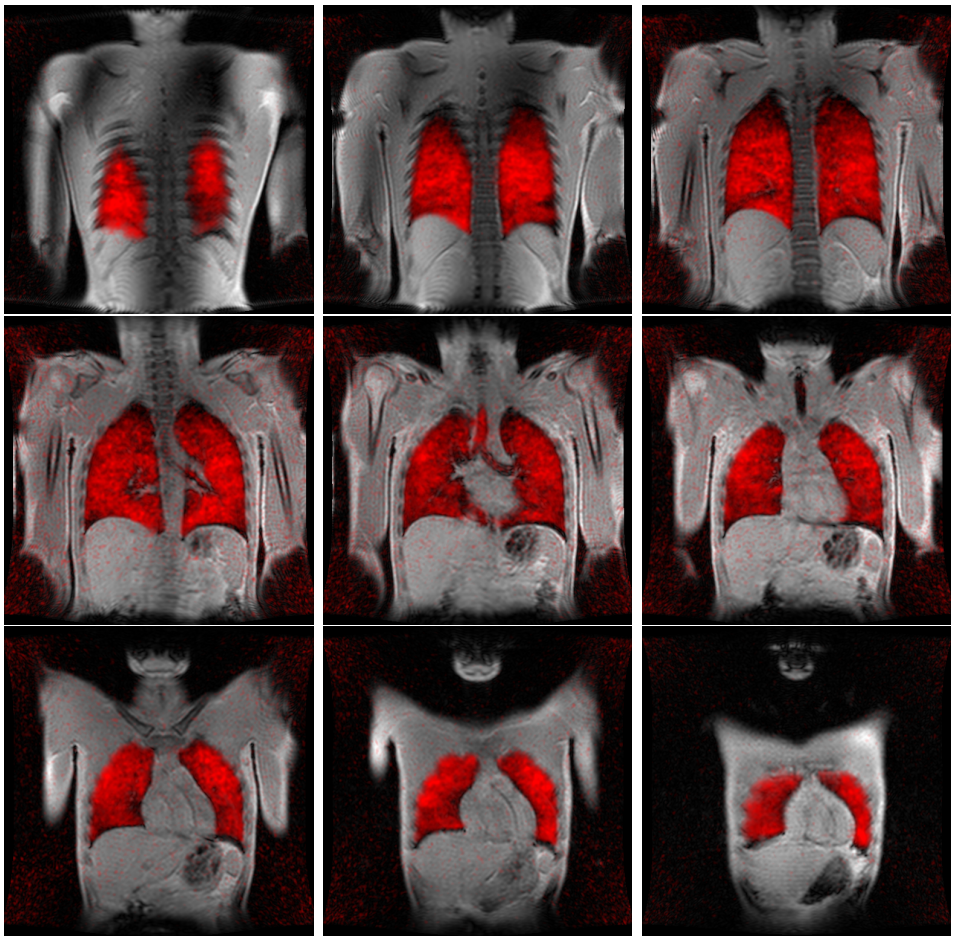

Coronal In-Vivo ^{129}Xe bbfgre scan (alpha-red) overlaid onto a corresponding Proton co-registration scan (black and white).Performed on a healthy volunteer, using a 1 L bag of ∼9.5% polarised ^{129}Xe gas. The ^{129}Xe scan was started after the volunteer had inhaled the bag. Proton Scan: FOV = 48 cm, Slice Thickness/Spacing = 1.0/0.5 cm Res = 128x128, Te = 5.0 ms, Tr = 70 ms, Flip Angle = 30°. ^{129}Xe Scan: FOV = 48 cm, Slice Thickness/Spacing = 1.0/0.5 cm Res = 128x128, Te = 5.0 ms, Tr = 8.4 ms, Flip Angle = 35°.

As can be seen in these two examples, the ^{129}Xe scan agrees with the proton co-registration scan, in that where there is signal in the proton scan, there is a reduction in signal from the Xe scan. Notable cases are in the top middle and right images of Figure 90 and the top right image and entire middle row of Figure 91, where signal from blood vessels can be seen in the proton images, with a corresponding decrease of signal in the Xenon images. This helps boost confidence in the reliability of the ^{129}Xe scans in their ability to highlight areas with decreased gas penetration.

One major drawback of this technique is that the proton co-registration images do not always match the ^{129}Xe images, due to the volunteer inhaling a different amount, or in a different manner. The best technique would be to perform both scans at the same time, such that the proton scan is taken in the same breath hold as the ^{129}Xe image. However with the current system available, this is not feasible. Another improvement would be to use a Tedlar bag filled with medical air, to the same volume as that of the ^{129}Xe bags, to better help the volunteer match the same inhalation volume. This is more feasible, but may require a slight adjustment to the currently approved study protocol.

7.5.4 Inhalation Methods

An important aspect of the scan protocol to develop during the pilot stage is the ^{129}Xe inhalation method. The main concern is that the ^{129}Xe gas may become 'trapped', and not reach the areas of interest (such as the furthest lung pathways). A second inhalation of room air following the ^{129}Xe inhalation (henceforth referred to as a 'flushing' breath) may help move the

^{129}Xe gas from the upper airways and trachea down into the lungs.

Several scans were performed, on multiple healthy volunteers, to help determine the effect of both the flushing breath and the original ^{129}Xe bolus size on the resulting images. Figure 92 shows pairs of images, each pair taken on the same volunteer on the same visit, using the same scan settings, one with and one without a flushing breath. As can be seen, where no flushing breath was used, the upper airways are often visible. Without the upper airways are not visible. This suggests that the flushing breath does indeed clear the upper airways of ^{129}Xe. It is also evident that the cross-sectional size of the lung is smaller in the non-flushing breath image, which may be the cause of the higher SNR in those images (as the ^{129}Xe is concentrated into a smaller region). The size of the lung also changes between images in a different manner for each volunteer (i.e getting longer rather than wider, vice versa, or a mix), perhaps suggesting that each volunteer inhales differently (e.g. primarily breathing via contraction of the diaphragm, or via the expansion of the rib cage, or both).

Figure 93 shows two images, taken on the same volunteer on two separate visits, using the same scan settings but with two different ^{129}Xe bolus sizes. A flushing breath was used for both images. There appear to be no obvious differences in the two scans, other than that the SNR for the images increased slightly (raw SNR was 15.3 and 16.7 respectively). This is most likely due to the flushing breath, that makes the total inhalation volume approximately the same, regardless of the initial bolus size.

Figure 92: Comparison of Flushing to no Flushing Breath

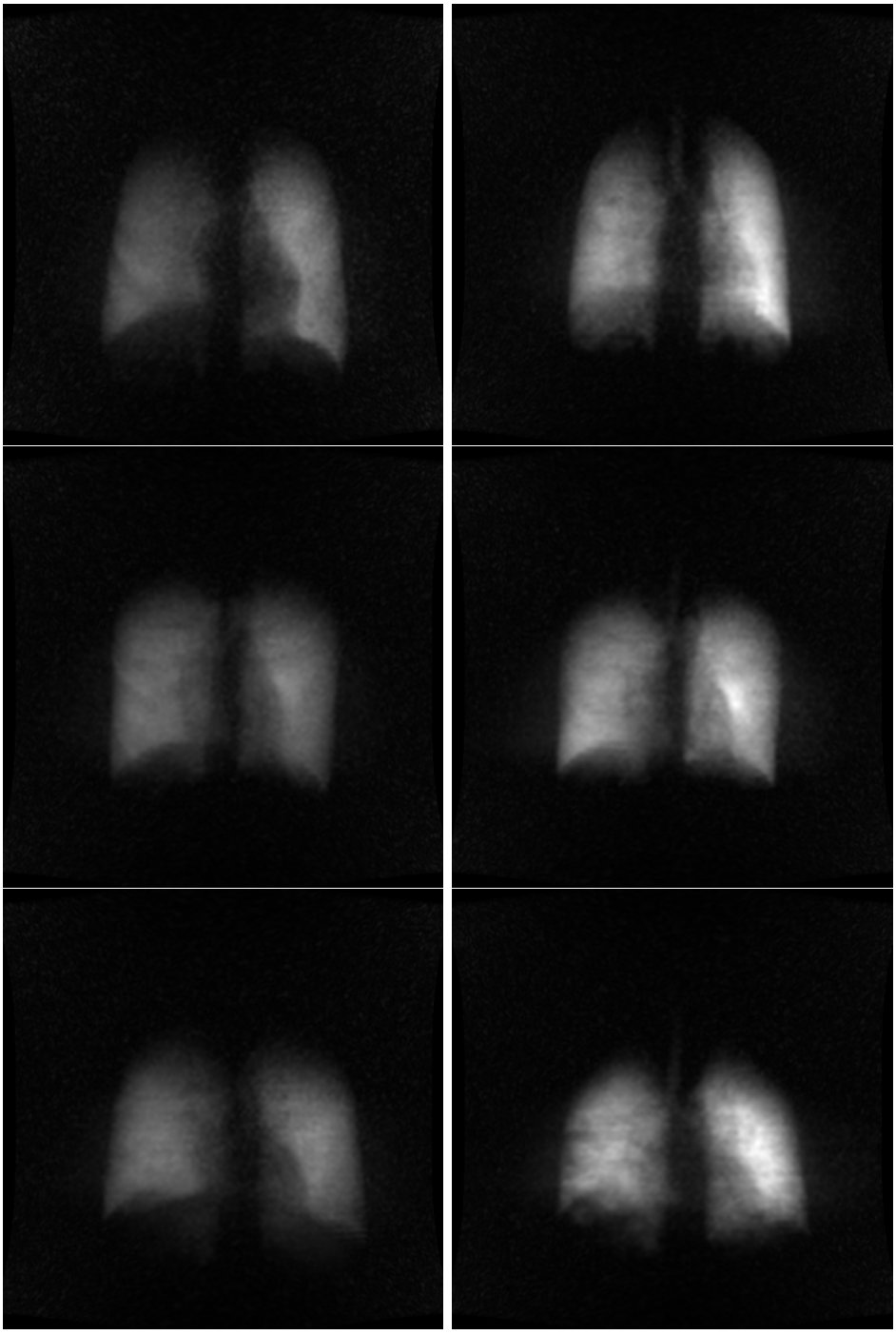

Coronal In-Vivo images taken using the bbfgre sequence, with the slice gradient switched off, using a 1 L bag of ∼9.1% polarised ^{129}Xe gas. Each pair of images was taken on the same volunteer. The left scans were started after the volunteer had inhaled the bag and taken a flushing breath, the right scans were started after the volunteer inhaled the bag. FOV = 48 cm, Res = 128x128, Te = 5.0 ms, Tr = 7.6 ms, Flip Angle = 20°. Raw SNR, starting top left, across then down: 12.10, 30.61, 18.37, 36.81, 20.64, 50.54.

Figure 93: Comparison of Different Bolus Sizes

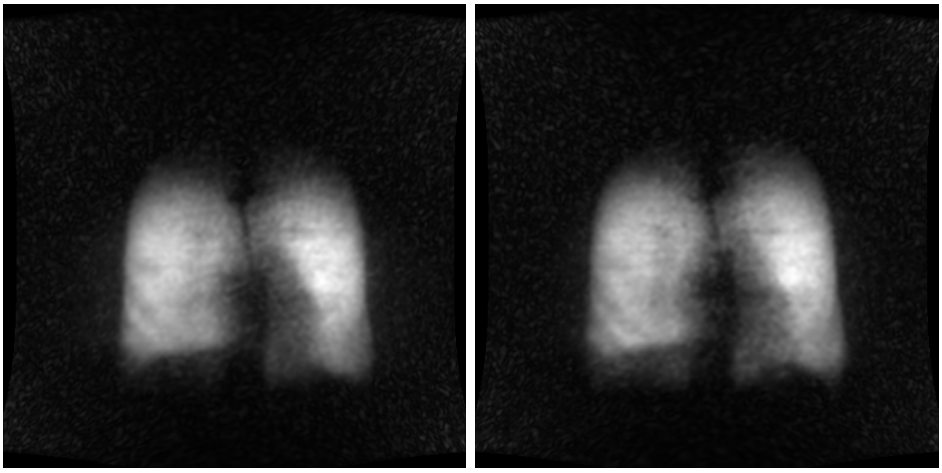

Coronal In-Vivo images taken using the bbfgre sequence, with the slice gradient switched off, on the same healthy volunteer. The left image was taken using a 0.6 L bag of ∼9.0% polarised ^{129}Xe gas, and the right image was taken using a 1 L bag of ∼9.3% polarised ^{129}Xe gas. The scan was started after the volunteer had inhaled the bag and a second 'flushing' breath. FOV = 48 cm, Res = 128x128, Te = 5.0 ms, Tr = 7.6 ms, Flip Angle = 20°. Raw SNR Left Image: 15.30, Right Image: 16.67.

7.5.5 Dynamic Ventilation Images

Of some interest to the medical field is the manner in which the gas flows into the lungs during inhalation. To view this, a dynamic ventilation scans can be performed, where successive ^{129}Xe scans are preformed during the inhalation of the gas. So far this method has been tested twice, once using the old scan sequence, with a low flip angle, and once with the new scan sequence, using a higher flip angle.

Figure 94 shows the dynamic ventilation images collected using the old bb2dfast scan sequence, with a small flip angle of 5.5°. As can be seen, at the start of the scan only the upper airways are seen, then the lungs become progressively brighter as more gas flows into them, before fading away as the polarisation decreases with each successive scan. Figure 95 shows the

Figure 94: bb2dfast Dynamic Lung Images

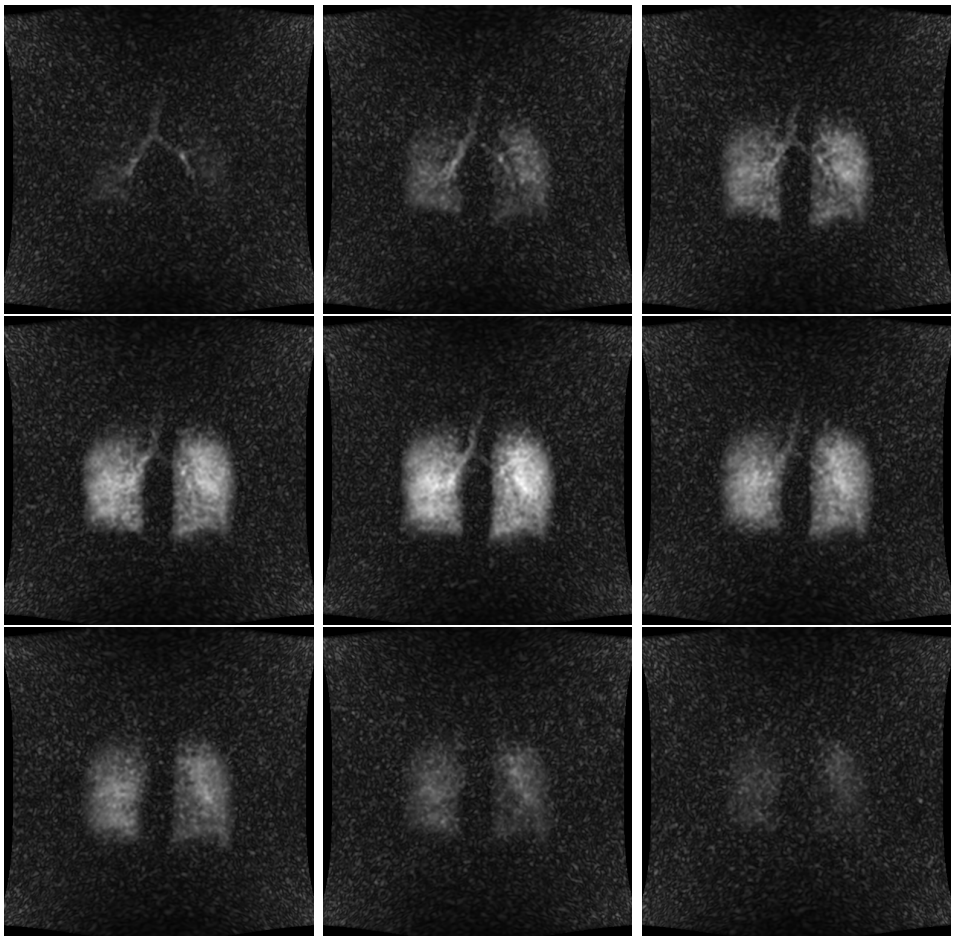

Coronal In-Vivo images taken using the bb2dfast sequence, with the slice gradient switched off, on a healthy volunteer, using a 1 L bag of ∼8.2% polarised ^{129}Xe gas. The scan was started, and then the volunteer slowly inhaled the bag. Each image was taken approximately 1.2 seconds apart. FOV = 48 cm, Res = 128x128, Te = 4.2 ms, Tr = 9 ms, Flip Angle = 5.5°. Raw SNR, Staring from Top Left, across then down: 1.04, 1.26, 1.55, 1.98, 2.38, 1.89, 1.44, 1.21, 1.13.

Figure 95: bbfgre Dynamic Lung Images

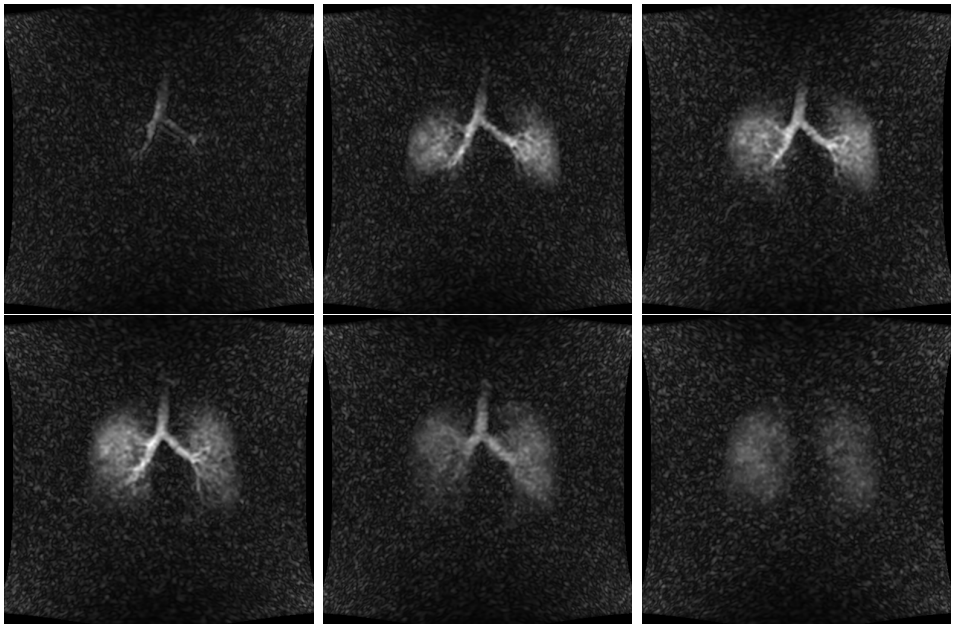

Coronal In-Vivo images taken using the bbfgre sequence, with the slice gradient switched off, on a healthy volunteer, using a 0.6 L bag of ∼9.4% polarised ^{129}Xe gas. The scan was started, and then the volunteer slowly inhaled the bag. Each image was taken approximately 1.0 seconds apart. FOV = 48 cm, Res = 128x128, Te = 5 ms, Tr = 7.5 ms, Flip Angle = 20°. Raw SNR, Staring from Top Left, across then down: 0.91, 1.39, 1.74, 1.80, 1.37, 1.37.

dynamic ventilation images collected using the new bbfgre scan sequence, with a larger flip angle of 20°. As can be seen, at the start the image only shows the upper airways. However, unlike the first set of images, the entirety of the lungs do not come into focus through the successive images. This is due to the higher flip angle, which reduces the polarisation of the previously excited gas significantly, so the majority of the signal only comes from the freshly inhaled gas, and such only the upper airways and upper lung are seen.

It is clear that more development is needed, to find the optimum flip angles to give the required balance of gas penetration and SNR to highlight ventilation to whichever the required areas of interest are within the lungs (such as upper or lower airways).

7.6 Dissolved-Phase Spectroscopy and Imaging

An attractive quality of ^{129}Xe is the possibility of dissolved-phase imaging, of the brain, lung or other regions, due to its solubility in blood and lipid-rich tissue [82]. The dissolved-phase resonance of Xenon has been measured to be shifted by approximately 200 ppm from the gas-phase resonance [60], which makes it feasible for both phases to be collected in a single acquisition. However, before more complex imaging and spectroscopy sequences can be developed and used to exploit this quality, it must first be confirmed that the system can detect the dissolved-phase signal, as there is much less signal available then there is for the gas-phase.

Figure 96: Initial Dissolved State ^{129}Xe Spectra

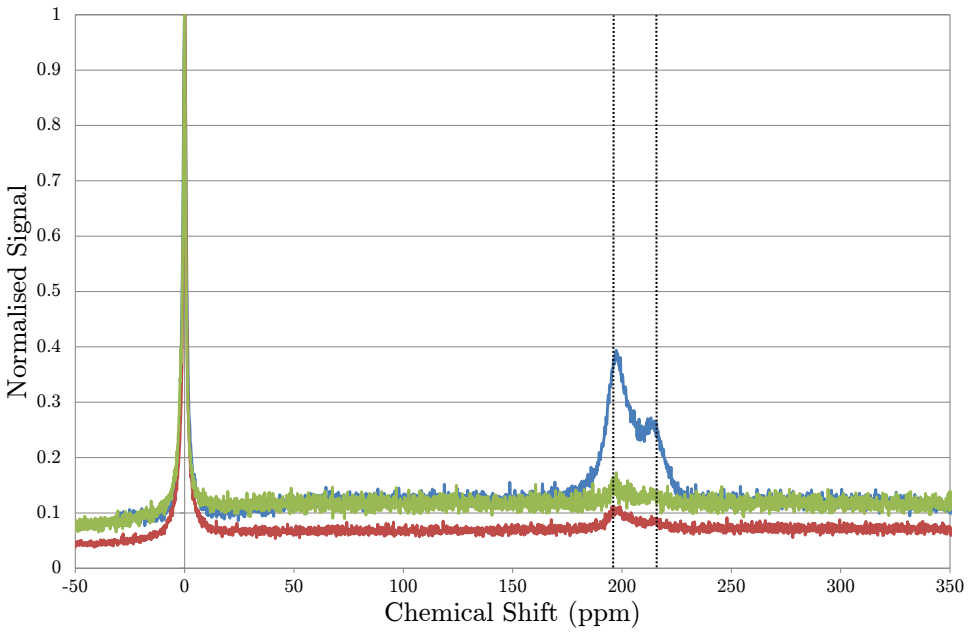

Results from three spectroscopy scans on two different volunteers, normalised to the gas signal. Scan parameters: No. of Samples = 4096, No. of Acquisitions = 25, Tr = 360 ms (blue) 528 ms (red/green), Spectral Width = 7042 Hz (blue), 8928 Hz (red/green). Two dotted lines have been placed to represent the expected dissolved state peaks, the left most line representing the expected ∼196 ppm lung parenchyma peak [62], and the right most line representing the expected ∼216 ppm red blood cell peak [62].

A simple pulse and acquire routine (with all gradients switched off), was used to provide FID spectra, with the pulse/acquire frequency targeted at 200 ppm above the gas-phase frequency. Figure 96 shows the results from two such scans, where the multiple acquisitions have been averaged together, and the x-scale adjusted to center on the gas-phase peak. As can be seen, the multiple peaks associated with dissolved-state Xenon (from Xenon in the lung parenchyma and the red blood cells) have been successfully detected, at the expected positions. The first two experiments performed (red and green lines), were done with a longer Tr time and wider spectral width, which may be the cause of the reduced signal strength for the dissolved peaks in those images. This will be investigated in future scans, in order to help maximise the signal strength of the dissolved peaks.

After the success of detecting the dissolved-phase signal, an image of the dissolved-phase ^{129}Xe in the lungs was attempted. The volunteer was instructed to breath in the ^{129}Xe gas, with a secondary flushing breath, as usual. Then the bbfgre sequence was used to produce 5 images (each taken approximately 2 seconds apart during the breath hold). Figure 97 shows the 5 images, alongside an image constructed from a simple average of the other 5. A higher level of Gaussian filtering then usual was used during image reconstruction, to increase the SNR of the images (at an expense to the resolution). As can be seen, there is a faint image of the lungs, in the majority of the images, that becomes more apparent in the last averaged image.

Figure 97: Initial Dissolved-Phase Images

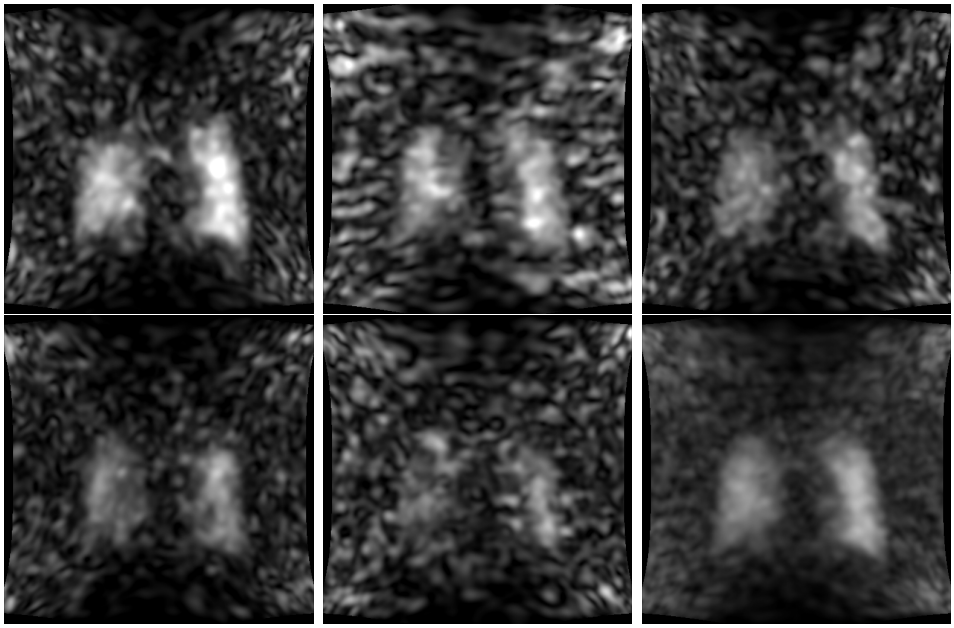

Coronal In-Vivo dissolved-phase images taken using the bbfgre sequence, with the slice gradient switched off, on a healthy volunteer, using a 1 L bag of ∼9.0% polarised ^{129}Xe gas. The scan was started immediately after the volunteer inhaled the bag and a second flushing breath. Each of the 5 image was taken approximately 2.0 seconds apart. FOV = 48 cm, Res = 64x64, Te = 1.5 ms, Tr = 15 ms, Flip Angle = 30°. The final bottom right image is a simple average of the other 5 images.

7.7 Conclusions and Future Work

As has been shown, good progress has been made to develop hyperpolarised ^{129}Xe MRI techniques at the University of Nottingham. Good lung images have been achieved, down to 2.5 cm thick slices. Initial images have been taken of both dynamic ventilation and dissolved-phase ^{129}Xe in the lungs.

However, more development is still required. The SNR of the dissolved-phase images and raw spectroscopy is very low, and needs to be improved upon. The settings for the dynamic ventilation images still need optimising for the required areas of interest (upper or lower airways). Proton co-registration protocol could be improved upon, to help ensure consistent and reliable matching between the proton images and corresponding ^{129}Xe images.

To help with SNR, an order for a new ^{129}Xe MRI chest coil has been placed. This new coil is of a 'life-jacket' style design, allowing the transmit and receive coils to be closer to the area of interest, a method that may provide higher SNR images. The new design also allows volunteers of larger sizes to participate, and increases volunteer comfort. A second generation of the ^{129}Xe polariser is also in construction, which once completed and its use approved, should be able to provide higher levels of polarisation for future work.

8 Conclusions

The work presented in this thesis has investigated both hyperpolarised gas MR spectroscopy and imaging, with both ^{3}He and ^{129}Xe gas. Hyperpolarised ^{3}He MRI was used to investigate and and provide information on both asthma and cystic fibrosis, alongside conventional lung function tests and quantitative CT. Hyperpolarised ^{129}Xe MRI techniques were developed within the department, in preparation for future human studies within the department, which included initial dissolved-state spectroscopy and imaging.

In the first study, the Chiesi study, the nature of the acinar airway involvement in asthma sufferers was investigated, using ^{3}He hyperpolarised diffusion MRI, alongside quantitative Computer Tomography densitometry and standard lung function tests. The hypothesis, that asthma patients with an elevated MBW S_{acin} parameter would manifest altered long-range diffusion, was tested by comparing the parameter with the short and long time-scale ADC values, as measured from the hyperpolarised MRI. An association was found, between S_{acin} and the long time-scale ADC (1 second) in patients with asthma, that was not observed in healthy patients, and failed to be reproduced purely by inflation of the lungs. This suggested that a specific structural abnormality may exist in the pulmonary acinus, that results in elevations of the long time-scale ADC values in asthmatics. However these observations where purely exploratory, and such further longitudinal studies are required before the significance of acinar airway disease in asthma can be determined. The results of this study was published in the Journal of

Allergy and Clinical Immunology.

In the second study, the Leicester Royal Infirmary Cystic Fibrosis study, the relationship between spirometry measurements and ^{3}He MRI short time-scale ADC values and Yablonskiy model R and h measurements were investigated in patients with Cystic Fibrosis. The short time-scale ADC values were found to decrease in patients with Cystic Fibrosis, although it was not significant enough to use a distinguishing parameter between healthy volunteers and Cystic Fibrosis patients. Inconsistencies were found in the R and h parameters, that may be explained by the recent criticism of the model for diffusion times greater than 2 ms. Future studies are required to determine if the model is valid, before the technique can be repeated as an investigative tool for exploring diseases such as Cystic Fibrosis.

In both of the above experiments, signal weighting was used on the calculation of the short time-scale ADC. However concerns have been raised, especially on the results of the LRI CF study, on whether this leads to a suppression of the areas of pathology. Further studies are required into this, as if the suppression is not an issue, the signal weighting has shown potential in reducing the statistical spread and error in the results for short time-scale ADC.

The final result section looked into the initial results of the pilot study to develop hyperpolarised ^{129}Xe MR imaging at the University of Nottingham. Although some good initial lung images have been acquired, including dissolved-state images, further study and development is required to achieve reliable and repeatable quality images, as required for both studies and

clinical work. The quality of the images collected at the University of Nottingham is expected to increase with the arrival of the new 'life-jacket' style ^{129}Xe MRI chest coil and the second generation ^{129}Xe polariser (capable of higher levels of polarisation), both of which are due to arrive within the upcoming year.

A Appendix

A.1 ^{1}H Scan Protocols

Protocol 1	
Pulse Sequence:	FSE-XL
PSD Name:	fse-xl
P Weight:	40
P Postition:	Supine
P Entry:	Head first
Coil:	BODY
Plane:	Axial
Mode:	2D
No. of Te:	1
Te:	Min Full (13.1)
Tr:	460
Echo train length:	32
Flip Angle:	90
Freq:	512
Phase:	512
NEX:	4
No. Slices:	42
Slice Thickness:	10
Spacing:	1.5
FOV:	48
Bandwidth:	31.25
Est. SAR:	1.4
Peak SAR:	2.8
Scan Time:	42:50

Protocol 2	
Pulse Sequence:	FSE-XL
PSD Name:	fse
P Weight:	40
P Postition:	Supine
P Entry:	Head first
Coil:	BODY
Plane:	Axial
Mode:	2D
No. of Te:	1
Te:	Min Full (21.3)
Tr:	720
Echo train length:	32
Flip Angle:	90
Freq:	512
Phase:	512
NEX:	3
No. Slices:	42
Slice Thickness:	10
Spacing:	1.5
FOV:	32
Bandwidth:	15.63
Est. SAR:	0.9
Peak SAR:	1.8
Scan Time:	49:40

Protocol 3	
Pulse Sequence:	FSE-XL
PSD Name:	fse-xl
P Weight:	60
P Postition:	Supine
P Entry:	Head first
Coil:	BODY
Plane:	Coronal
Mode:	2D
No. of Te:	1
Te:	Min Full (13.1)
Tr:	460
Echo train length:	32
Flip Angle:	90
Freq:	512
Phase:	512
NEX:	8
No. Slices:	42
Slice Thickness:	10
Spacing:	1.5
FOV:	48
Bandwidth:	31.25
Est. SAR:	1.7
Peak SAR:	3.4
Scan Time:	42:47

Protocol 4	
Pulse Sequence:	SPGR
PSD Name:	bb2dfast
P Weight:	60
P Postition:	Supine
P Entry:	Head first
Coil:	BODY
Plane:	Coronal
Mode:	2D
No. of Te:	1
Te:	Minimum (2.7)
Tr:	11.0
Flip Angle:	180
Freq:	128
Phase:	128
NEX:	40
No. Slices:	46
Slice Thickness:	10
Spacing:	1.5
FOV:	32
Bandwidth:	15.63
Nuclei:	1
Est. SAR:	1.7
Peak SAR:	3.4
Scan Time:	43:15

Protocol 5	
Pulse Sequence:	SPGR
PSD Name:	bb2dfast
P Weight:	60
P Postition:	Supine
P Entry:	Head first
Coil:	BODY
Plane:	Coronal
Mode:	2D
No. of Te:	1
Te:	Minimum (2.7)
Tr:	11.0
Flip Angle:	180
Freq:	128
Phase:	128
NEX:	40
No. Slices:	46
Slice Thickness:	10
Spacing:	0.5
FOV:	48
Bandwidth:	31.25
Est. SAR:	1.7
Peak SAR:	3.4
Scan Time:	43:15
cfxfull:	0
cfyfull:	0
cfzfull:	0

A.2 ^{129}Xe Scan Protocols

Protocol 1	
Pulse Sequence:	SPGR
PSD Name:	bb2dfast
P Weight:	60
P Postition:	Supine
P Entry:	Head first
Coil:	RAPID BOTH
Plane:	Axial
Mode:	2D
Imaging Options:	Fast
Nucleus:	129
Te:	Minimum (4.8)
Tr:	14.0
Flip Angle:	180
Freq:	512
Phase:	512
NEX:	8
No. Slices:	42
Slice Thickness:	20
Spacing:	1.5
FOV:	48
Phase FOV:	1
Bandwidth:	31.25
Est. SAR:	0.0
Peak SAR:	0.1
Scan Time:	40:11
xmtaddScan:	60.206
TG:	186
Effective Flip Angle:	45

Protocol 2	
Pulse Sequence:	SPGR
PSD Name:	bb2dfast
P Weight:	60
P Postition:	Supine
P Entry:	Head first
Coil:	RAPID BOTH
Plane:	Axial
Mode:	2D
Imaging Options:	Fast
Nucleus:	129
Te:	Minimum (4.8)
Tr:	14.0
Flip Angle:	180
Freq:	512
Phase:	512
NEX:	8
No. Slices:	42
Slice Thickness:	20
Spacing:	1.5
FOV:	48
Phase FOV:	1
Bandwidth:	31.25
Est. SAR:	0.1
Peak SAR:	0.2
Scan Time:	40:11
xmtaddScan:	60.206
TG:	186
Effective Flip Angle:	45
cfxfull:	0
cfyfull:	0
cfzfull:	0

Protocol 3	
Pulse Sequence:	GRE
PSD Name:	bbfgre
P Weight:	50
P Postition:	Supine
P Entry:	Head first
Coil:	RAPID BOTH
Plane:	Axial
Mode:	2D
Imaging Options:	Fast
Nucleus:	129
Te:	Minimum (2.8)
Tr:	5.7
Flip Angle:	90
Freq:	64
Phase:	64
NEX:	1
No. Slices:	90
Slice Thickness:	5
Spacing:	0.0
FOV:	48
Phase FOV:	1
Bandwidth:	31.25
Est. SAR:	0.03
Peak SAR:	0.07
Scan Time:	00:38
xmtaddScan:	0.0
TG:	150
Effective Flip Angle:	30

Protocol 4	
Pulse Sequence:	GRE
PSD Name:	bbfgre
P Weight:	50
P Postition:	Supine
P Entry:	Head first
Coil:	RAPID BOTH
Plane:	Axial
Mode:	2D
Imaging Options:	Fast
Nucleus:	129
Te:	Minimum (2.8)
Tr:	15.0
Flip Angle:	90
Freq:	64
Phase:	64
NEX:	1
No. Slices:	90
Slice Thickness:	5
Spacing:	0.0
FOV:	48
Phase FOV:	1
Bandwidth:	31.25
Est. SAR:	0.03
Peak SAR:	0.05
Scan Time:	00:50
xmtaddScan:	0.0
TG:	150
Effective Flip Angle:	30
cfxfull:	0
cfyfull:	0
cfzfull:	0

References

[1] M. Albert, G. Cates, B. Driehuys, W. Happer, B. Saam, C. J. Springer, and A. Wishnia. Biological magnetic resonance imaging using laser-polarized 129xe. *Nature*, 370:199–201, 1994.

[2] Marcus Alley. Gradient field modeling on signa. Provided via communications with Hayley Newton, December 2013, December 2005.

[3] David S Armstrong, Keith Grimwood, Rosemary Carzino, John B Carlin, Anthony Olinsky, and Peter D Phelan. Lower respiratory infection and inflammation in infants with newly diagnosed cystic fibrosis. *Bmj*, 310(6994):1571–1572, 1995.

[4] Iain Ball. *Functional Pulmonary MRI Using Hyperpolarised 3He*. PhD thesis, University of Nottingham, 2011.

[5] Phillip J Barry and Ronald N Goldman. A recursive evaluation algorithm for a class of catmull-rom splines. In *ACM SIGGRAPH Computer Graphics*, volume 22-4, pages 199–204. ACM, 1988.

[6] Marion Batz, P-J Nacher, and Genevieve Tastevin. Fundamentals of metastability exchange optical pumping in helium. In *Journal of Physics: Conference Series*, volume 294, page 012002. IOP Publishing, 2011.

[7] J Becker, J Bermuth, M Ebert, T Grossmann, W Heil, D Hofmann, H Humblot, M Leduc, EW Otten, D Rohe, et al. Interdisciplinary experiments with polarized 3 he. *Nuclear Instruments and Methods in Physics Research Section A: Accelerators, Spectrometers, Detectors and Associated Equipment*, 402(2):327–336, 1998.

[8] MA Bernstein, KF King, and XJ Zhou. *Handbook of MRI pulse sequences*. Elsevier Academic Press, 2004.

[9] M Ab Bouchiat, TR Carver, and CM Varnum. Nuclear polarization in 3He gas induced by optical pumping and dipolar exchange. *Phys. Rev. Letters*, 5, 1960.

[10] Mathieu Boudreau, Xiaojun Xu, and Giles E Santyr. Measurement of 129xe gas apparent diffusion coefficient anisotropy in an elastase-instilled rat model of emphysema. *Magnetic Resonance in Medicine*, 69(1):211–220, 2013.

[11] Jean Bousquet, Eva Mantzouranis, Alvaro A Cruz, Nadia Aït-Khaled, Carlos E Baena-Cagnani, Eugene R Bleecker, Chris E Brightling, Peter

Burney, Andrew Bush, William W Busse, et al. Uniform definition of asthma severity, control, and exacerbations: document presented for the world health organization consultation on severe asthma. *Journal of Allergy and Clinical Immunology*, 126(5):926–938, 2010.

[12] CE Brightling, S Gupta, S Gonem, and S Siddiqui. Lung damage and airway remodelling in severe asthma. *Clinical & Experimental Allergy*, 42(5):638–649, 2012.

[13] Jean Brossel and Alfred Kastler. La detection de la resonance magnetique des niveaux excites-leffect de depolarisation des radiations de resonance optique et de fluorescence. *Comptes Rendus Hebdomadaires Des Seances De L Academie Des Sciences*, 229(23):1213–1215, 1949.

[14] Benjamin Burrows, Ronald J Knudson, and Michael D Lebowitz. The relationship of childhood respiratory illness to adult obstructive airway disease 1–3. *American Review of Respiratory Disease*, 115(5):751–760, 1977.

[15] X Josette Chen, Laurence W Hedlund, Harald E Möller, Mark S Chawla, Robert R Maronpot, and G Allan Johnson. Detection of emphysema in rat lungs by using magnetic resonance measurements of 3he diffusion. *Proceedings of the National Academy of Sciences*, 97(21):11478–11481, 2000.

[16] H Chrystyn. Anatomy and physiology in delivery: can we define our targets? *Allergy*, 54(s49):82–87, 1999.

[17] FD Colegrove and PA Franken. Optical pumping of helium in the s 1 3 metastable state. *Physical Review*, 119(2):680, 1960.

[18] FD Colegrove, LD Schearer, and GK Walters. Polarization of he 3 gas by optical pumping. *Physical Review*, 132(6):2561, 1963.

[19] GINA Executive Committee et al. Global strategy for asthma management and prevention, global initiative for asthma (gina). Available from: http://www.ginasthma.org/, 2010. Accessed June 30, 2011.

[20] Bryan Corrin and Andrew G Nicholson. *Pathology of the Lungs: Expert Consult: Online and Print*. Elsevier Health Sciences, 3 edition, 2011.

[21] CP Criée, S Sorichter, HJ Smith, P Kardos, R Merget, D Heise, D Berdel, D Köhler, H Magnussen, W Marek, et al. Body plethysmography–its principles and clinical use. *Respiratory medicine*, 105(7):959–971, 2011.

[22] JJR Frausto Da Silva and Robert Joseph Paton Williams. *The biological chemistry of the elements: the inorganic chemistry of life*. Oxford University Press, 2001.

[23] HG Dehmelt. Slow spin relaxation of optically polarized sodium atoms. *Physical Review*, 105(5):1487, 1957.

[24] Asger Dirksen, Joop H Dijkman, Flemming Madsen, Berend Stoel, Duncan CS Hutchison, Charlotte S Ulrik, Lene T Skovgaard, Axel Kok-Jensen, Arjan Rudolphus, Niels Seersholm, Henri A Vrooman, Johan HC Reiber, Niels C Hansen, Thomas Heckscher, Kaj Viskum, and Jan Stolk. A randomized clinical trial of α1-antitrypsin augmentation therapy. *American journal of respiratory and critical care medicine*, 160(5):1468–1472, 1999.

[25] Bastiaan Driehuys, Jim Pollaro, and Gary P Cofer. In vivo mri using real-time production of hyperpolarized 129xe. *Magnetic resonance in medicine*, 60(1):14–20, 2008.

[26] Brigitte Dutrieue, Frederique Vanholsbeeck, Sylvia Verbanck, and Manuel Paiva. A human acinar structure for simulation of realistic alveolar plateau slopes. *Journal of Applied Physiology*, 89(5):1859–1867, 2000.

[27] G Eckert, W Heil, M Meyerhoff, EW Otten, R Surkau, M Werner, M Leduc, PJ Nacher, and LD Schearer. A dense polarized 3He target based on compression of optically pumped gas. *Nuclear Instruments and Methods in Physics Research Section A: Accelerators, Spectrometers, Detectors and Associated Equipment*, 320(1):53–65, 1992.

[28] Claude S Farah, Gregory G King, Nathan J Brown, Sue R Downie, Jessica A Kermode, Kate M Hardaker, Matthew J Peters, Norbert Berend, and Cheryl M Salome. The role of the small airways in the clinical expression of asthma in adults. *Journal of Allergy and Clinical Immunology*, 129(2):381–387, 2012.

[29] Claude S Farah, Gregory G King, Nathan J Brown, Matthew J Peters, Norbert Berend, and Cheryl M Salome. Ventilation heterogeneity predicts asthma control in adults following inhaled corticosteroid dose titration. *Journal of Allergy and Clinical Immunology*, 130(1):61–68, 2012.

[30] W Franzen and AG Emslie. Atomic orientation by optical pumping. *Physical Review*, 108(6):1453, 1957.

[31] Eiichi Fukushima and Stephen B.W. Roeder. *Experimental Pulse NMR: A Nuts and Bolts Approach*. Perseus Books, 1981.

[32] David S Gierada, Jason C Woods, Andrew J Bierhals, Seth T Bartel, Jon H Ritter, Cliff K Choong, Nitin A Das, Cheng Hong, Thomas K Pilgram, Yulin V Chang, et al. Effects of diffusion time on short-range hyperpolarized 3he diffusivity measurements in emphysema. *Journal of Magnetic Resonance Imaging*, 30(4):801–808, 2009.

[33] Sherif Gonem, Steven Hardy, Niels Buhl, Ruth Hartley, Marcia Soares, Richard Kay, Rino Costanza, Per Gustafsson, Christopher Brightling, John Owers-Bradley, and Salman Siddiqui. Characterization of acinar airspace involvement in asthmatic patients by using inert gas washout and hyperpolarized 3 helium magnetic resonance. *Journal of Allergy and Clinical Immunology*, 137(2):417–425, 2015.

[34] Sherif Gonem, Sushiladevi Natarajan, Dhananjay Desai, Steven Corkill, Amisha Singapuri, Peter Bradding, Per Gustafsson, Rino Costanza, Radhika Kajekar, Harsukh Parmar, et al. Clinical significance of small airway obstruction markers in patients with asthma. *Clinical & Experimental Allergy*, 44(4):499–507, 2014.

[35] H Gono, K Fujimoto, S Kawakami, and K Kubo. Evaluation of airway wall thickness and air trapping by hrct in asymptomatic asthma. *European Respiratory Journal*, 22(6):965–971, 2003.

[36] Boyd M Goodson. Nuclear magnetic resonance of laser-polarized noble gases in molecules, materials, and organisms. *Journal of Magnetic Resonance*, 155(2):157–216, 2002.

[37] GOV.UK. Gov uk: Patient dose information. `https://www.gov.uk/government/publications/medical-radiation-patient-doses/patient-dose-information-guidance`. Accessed: 2016-09-25.

[38] BC Grover. Noble-gas nmr detection through noble-gas-rubidium hyperfine contact interaction. *Physical Review Letters*, 40(6):391, 1978.

[39] Sumit Gupta, Ruth Hartley, Umair T Khan, Amisha Singapuri, Beverly Hargadon, William Monteiro, Ian D Pavord, Ana R Sousa, Richard P Marshall, Deepak Subramanian, David Parr, James J Entwisle, Salman Siddiqui, Vimal Raj, and Christopher E Brightling. Quantitative computed tomography–derived clusters: Redefining airway remodeling in asthmatic patients. *Journal of Allergy and Clinical Immunology*, 133(3):729–738, 2014.

[40] EM Haacke, ED Lindskogj, and W Lin. A fast, iterative, partial-fourier technique capable of local phase recovery. *Journal of Magnetic Resonance (1969)*, 92(1):126–145, 1991.

[41] Adam J Hajari, Dmitriy A Yablonskiy, Alexander L Sukstanskii, James D Quirk, Mark S Conradi, and Jason C Woods. Morphometric changes in the human pulmonary acinus during inflation. *Journal of Applied Physiology*, 112(6):937–943, 2012.

[42] Shane Hanon, Daniel Schuermans, Walter Vincken, and Sylvia Verbanck. Irreversible acinar airway abnormality in well controlled asthma. *Respiratory medicine*, 108(11):1601–1607, 2014.

[43] Liam G Heaney, Chris E Brightling, Andrew Menzies-Gow, Michael Stevenson, Rob M Niven, British Thoracic Society Difficult Asthma Network, et al. Refractory asthma in the UK: cross-sectional findings from a UK multicentre registry. *Thorax*, 65(9):787–794, 2010.

[44] Alex R Horsley, Per M Gustafsson, KA Macleod, Clare Saunders, Andrew P Greening, DJ Porteous, JC Davies, Steve Cunningham, EWFW Alton, and J Alastair Innes. Lung clearance index is a sensitive, repeatable and practical measure of airways disease in adults with cystic fibrosis. *Thorax*, 63(2):135–140, 2008.

[45] Richard E Jacob, Gernot Laicher, and Kevin R Minard. 3d mri of non-gaussian 3 he gas diffusion in the rat lung. *Journal of Magnetic Resonance*, 188(2):357–366, 2007.

[46] Ian DA Johnston, David P Strachan, and H Ross Anderson. Effect of pneumonia and whooping cough in childhood on adult lung function. *New England Journal of Medicine*, 338(9):581–587, 1998.

[47] Elizabeth F Juniper, A Sonia Buist, Fred M Cox, Penelope J Ferrie, and Derek R King. Validation of a standardized version of the asthma quality of life questionnaire. *CHEST Journal*, 115(5):1265–1270, 1999.

[48] Elizabeth F Juniper, Klas Svensson, Ann-Christin Mörk, and Elisabeth Ståhl. Measurement properties and interpretation of three shortened versions of the asthma control questionnaire. *Respiratory medicine*, 99(5):553–558, 2005.

[49] Alfred Kastler. Optical methods of atomic orientation and of magnetic resonance. *JOSA*, 47(6):460–465, 1957.

[50] S Sivaram Kaushik, Zackary I Cleveland, Gary P Cofer, Gregory Metz, Denise Beaver, John Nouls, Monica Kraft, William Auffermann, Jan

Wolber, H Page McAdams, et al. Diffusion-weighted hyperpolarized 129xe mri in healthy volunteers and subjects with chronic obstructive pulmonary disease. *Magnetic Resonance in Medicine*, 65(4):1154–1165, 2011.

[51] James Keeler. *Understanding NMR Spectroscopy*. WILEY, 2nd edition, 2010.

[52] Monica Kraft, Richard J Martin, Susan Wilson, Ratko Djukanovic, and Stephen T Holgate. Lymphocyte and eosinophil influx into alveolar tissue in nocturnal asthma. *American journal of respiratory and critical care medicine*, 159(1):228–234, 1999.

[53] Malcolm H. Levitt. *Spin Dynamics: Basics of Nuclear Magnetic Resonance*. WILEY, 2nd edition, 2008.

[54] David ML Lilburn, Theodore Hughes-Riley, Joseph S Six, Karl F Stupic, Dominick E Shaw, Galina E Pavlovskaya, and Thomas Meersmann. Validating excised rodent lungs for functional hyperpolarized xenon-129 mri. *PloS one*, 8(8):e73468, 2013.

[55] N Macintyre, RO Crapo, G Viegi, DC Johnson, CPM Van der Grinten, V Brusasco, F Burgos, R Casaburi, A Coates, P Enright, et al. Standardisation of the single-breath determination of carbon monoxide uptake in the lung. *European Respiratory Journal*, 26(4):720–735, 2005.

[56] Jaime F Mata, Talissa A Altes, Jing Cai, Kai Ruppert, Wayne Mitzner, Klaus D Hagspiel, Bina Patel, Michael Salerno, James R Brookeman, Eduard E de Lange, et al. Evaluation of emphysema severity and progression in a rabbit model: comparison of hyperpolarized 3he and 129xe diffusion mri with lung morphometry. *Journal of Applied Physiology*, 102(3):1273–1280, 2007.

[57] John E McDonough, Ren Yuan, Masaru Suzuki, Nazgol Seyednejad, W Mark Elliott, Pablo G Sanchez, Alexander C Wright, Warren B Gefter, Leslie Litzky, Harvey O Coxson, et al. Small-airway obstruction and emphysema in chronic obstructive pulmonary disease. *New England Journal of Medicine*, 365(17):1567–1575, 2011.

[58] Pippa McGowan, Angus Jeffries, and Andrew Turley. *Crash Course: Respiratory System*. Mosby, 2 edition, 2003.

[59] Donald W. McRobbie, Elizabeth A. Moore, Martin J. Graves, and Martin R. Prince. *MRI: From Picture to Proton*. Cambridge University Press, 2003.

[60] Keith W Miller, Nicholas V Reo, AJ Schoot Uiterkamp, Diane P Stengle, Thomas R Stengle, and Kenneth L Williamson. Xenon nmr: chemical shifts of a general anesthetic in common solvents, proteins, and membranes. *Proceedings of the National Academy of Sciences*, 78(8):4946–4949, 1981.

[61] Martin R Miller, JATS Hankinson, V Brusasco, F Burgos, R Casaburi, A Coates, R Crapo, P Enright, CP Van der Grinten, P Gustafsson, et al. Standardisation of spirometry. *Eur Respir J*, 26(2):319–38, 2005.

[62] John P Mugler, Bastiaan Driehuys, James R Brookeman, Gordon D Cates, Stuart S Berr, Robert G Bryant, Thomas M Daniel, Eduard E De Lange, J Hunter Downs, Christopher J Erickson, William Happer, Denise P Hinton, Neal F Kassel, Therese Maier, C Douglas Phillips, Brian T Saam, Karen L Sauer, and Mark E Wagshul. Mr imaging and spectroscopy using hyperpolarized 129xe gas: preliminary human results. *Magnetic Resonance in Medicine*, 37(6):809–815, 1997.

[63] Josephine H Naish, Geoffrey JM Parker, Paul C Beatty, Alan Jackson, Simon S Young, John C Waterton, and Chris J Taylor. Improved quantitative dynamic regional oxygen-enhanced pulmonary imaging using image registration. *Magnetic resonance in medicine*, 54(2):464–469, 2005.

[64] NHS. Cystic fibrosis - nhs choices. `http://www.nhs.uk`. Accessed: 2015-09-01.

[65] Emir Osmanagic, Alexander L Sukstanskii, James D Quirk, Jason C Woods, Richard A Pierce, Mark S Conradi, Ewald R Weibel, and Dmitriy A Yablonskiy. Quantitative assessment of lung microstructure in healthy mice using an mr-based 3he lung morphometry technique. *Journal of Applied Physiology*, 109(6):1592–1599, 2010.

[66] Albert W Overhauser. Polarization of nuclei in metals. *Physical Review*, 92(2):411, 1953.

[67] Juan Parra-Robles and Jim M Wild. On the use of 3he diffusion magnetic resonance as evidence of neo-alveolarization during childhood and adolescence. *American journal of respiratory and critical care medicine*, 189(4):501–502, 2014.

[68] Samuel Patz, F William Hersman, Iga Muradian, Mirko I Hrovat, Iulian C Ruset, Stephen Ketel, Francine Jacobson, George P Topulos, Hiroto Hatabu, and James P Butler. Hyperpolarized 129 xe mri: A viable functional lung imaging modality? *European journal of radiology*, 64(3):335–344, 2007.

[69] ID Pavord, MM Pizzichini, E Pizzichini, and FE Hargreave. The use of induced sputum to investigate airway inflammation. *Thorax*, 52(6):498–501, 1997.

[70] G Peces-Barba, J Ruiz-Cabello, Y Cremillieux, I Rodriguez, D Dupuich, V Callot, M Ortega, ML Rubio Arbo, M Cortijo, and N Gonzalez-Mangado. Helium-3 mri diffusion coefficient: correlation to morphometry in a model of mild emphysema. *European Respiratory Journal*, 22(1):14–19, 2003.

[71] Philip H Quanjer, Sanja Stanojevic, Tim J Cole, Xaver Baur, Graham L Hall, Bruce H Culver, Paul L Enright, John L Hankinson, Mary SM Ip, Jinping Zheng, et al. Standardized lung function testing. *European Respiratory Journal*, 6(Suppl 16):3–100, 1993.

[72] Philip H Quanjer, Sanja Stanojevic, Tim J Cole, Xaver Baur, Graham L Hall, Bruce H Culver, Paul L Enright, John L Hankinson, Mary SM Ip, Jinping Zheng, et al. Multi-ethnic reference values for spirometry for the 3–95-yr age range: the global lung function 2012 equations. *European Respiratory Journal*, 40(6):1324–1343, 2012.

[73] Paul Robinson, Philipp Latzin, Sylvia Verbanck, Graham L Hall, Alexander Horsley, Monika Gappa, Cindy Thamrin, Hubertus GM Arets, Paul Aurora, S Fuchs, et al. Consensus statement for inert gas washout measurement using multiple and single breath tests. *European Respiratory Journal*, 41(3):507–522, 2013.

[74] Paul D Robinson, Michael D Goldman, and Per M Gustafsson. Inert gas washout: theoretical background and clinical utility in respiratory disease. *Respiration*, 78(3):339–355, 2009.

[75] Brian T Saam, Dmitriy A Yablonskiy, Vikram D Kodibagkar, Jason C Leawoods, David S Gierada, Joel D Cooper, Stephen S Lefrak, and Mark S Conradi. Mr imaging of diffusion of 3he gas in healthy and diseased lungs. *Magnetic resonance in medicine*, 44(2):174–179, 2000.

[76] Michael Salerno, Eduard E de Lange, Talissa A Altes, Jonathon D Truwit, James R Brookeman, and John P Mugler. Emphysema: Hyperpolarized helium 3 diffusion mr imaging of the lungs compared with spirometric indexesinitial experience 1. *Radiology*, 222(1):252–260, 2002.

[77] S Shaheen and DJ Barker. Early lung growth and chronic airflow obstruction. *Thorax*, 49(6):533–536, 1994.

[78] American Thoracic Society et al. Proceedings of the ats workshop on refractory asthma: Current understanding, recommendations, and unanswered questions. ATS, 2000.

[79] British Thoracic Society and Scottish Intercollegiate Guidelines Network. British guideline on the management of asthma, 2008.

[80] E Stoltz, M Meyerhoff, N Bigelow, M Leduc, P-J Nacher, and G Tastevin. High nuclear polarization in3he and3he-4he gas mixtures by optical pumping with a laser diode. *Applied Physics B*, 63(6):629–633, 1996.

[81] AL Sukstanskii and DA Yablonskiy. In vivo lung morphometry with hyperpolarized 3 he diffusion mri: theoretical background. *Journal of Magnetic Resonance*, 190(2):200–210, 2008.

[82] Herbert Susskind, Kenneth J Ellis, Harold L Atkins, Stanton H Cohn, and Powell Richards. Studies of whole-body retention and clearance of inhaled noble gases. *Progress in nuclear medicine*, 5:13–34, 1977.

[83] Bruce R Thompson, Jo A Douglass, Matthew J Ellis, Vanessa J Kelly, Robyn E O'Hehir, Gregory G King, and Sylvia Verbanck. Peripheral lung function in patients with stable and unstable asthma. *Journal of Allergy and Clinical Immunology*, 131(5):1322–1328, 2013.

[84] William M Thurlbeck and G Elspeth Angus. Growth and aging of the normal human lung. *CHEST Journal*, 67(2_Supplement):3S–7S, 1975.

[85] OS Usmani. Treating the small airways. *Respiration*, 84(6):441–53, 2012.

[86] S Verbanck, D Schuermans, A Van Muylem, M Paiva, M Noppen, and W Vincken. Ventilation distribution during histamine provocation. *Journal of Applied Physiology*, 83(6):1907–1916, 1997.

[87] Sylvia Verbanck and Manuel Paiva. Effective axial diffusion in an expansile alveolar duct model. *Respiration physiology*, 73(2):273–278, 1988.

[88] Sylvia Verbanck and Manuel Paiva. Simulation of the apparent diffusion of helium-3 in the human acinus. *Journal of applied physiology*, 103(1):249–254, 2007.

[89] Sylvia Verbanck and Manuel Paiva. Acinar determinants of the apparent diffusion coefficient for helium-3. *Journal of applied physiology*, 108(4):793–799, 2010.

[90] Sylvia Verbanck, Daniël Schuermans, Marc Meysman, Manuel Paiva, and Walter Vincken. Noninvasive assessment of airway alterations in smokers: the small airways revisited. *American journal of respiratory and critical care medicine*, 170(4):414–419, 2004.

[91] Sylvia Verbanck, Daniel Schuermans, Marc Noppen, ALAIN VAN MUYLEM, Manuel Paiva, and Walter Vincken. Evidence of acinar airway involvement in asthma. *American journal of respiratory and critical care medicine*, 159(5):1545–1550, 1999.

[92] Carolina Walker, Sumit Gupta, Ruth Hartley, and Christopher E Brightling. Computerized tomography scans in severe asthma: Utility and clinical implications. *Current opinion in pulmonary medicine*, 18(1):42, 2012.

[93] Chengbo Wang, Talissa A Altes, John P Mugler, G Wilson Miller, Kai Ruppert, Jaime F Mata, Gordon D Cates, Larry Borish, and Eduard E de Lange. Assessment of the lung microstructure in patients with asthma using hyperpolarized 3he diffusion mri at two time scales: comparison with healthy subjects and patients with copd. *Journal of Magnetic Resonance Imaging*, 28(1):80–88, 2008.

[94] Chengbo Wang, G Wilson Miller, Talissa A Altes, Eduard E de Lange, Gordon D Cates Jr, and John P Mugler. Time dependence of 3he diffusion in the human lung: Measurement in the long-time regime using stimulated echoes. *Magnetic resonance in medicine*, 56(2):296–309, 2006.

[95] Wei Wang, Nguyet M Nguyen, Dmitriy A Yablonskiy, Alexander L Sukstanskii, Emir Osmanagic, Jeffrey J Atkinson, Mark S Conradi, and Jason C Woods. Imaging lung microstructure in mice with hyperpolarized 3he diffusion mri. *Magnetic resonance in medicine*, 65(3):620–626, 2011.

[96] J Wanger, JL Clausen, A Coates, OF Pedersen, V Brusasco, F Burgos, R Casaburi, R Crapo, P Enright, CPM Van Der Grinten, et al. Standardisation of the measurement of lung volumes. *European Respiratory Journal*, 26(3):511, 2005.

[97] Barnaby Waters. *Imaging The Lungs Using Hyperpolarised Helium-3*. PhD thesis, University of Nottingham, 2006.

[98] Barnaby Waters, John Owers-Bradley, and Mike Silverman. Acinar structure in symptom-free adults by helium-3 magnetic resonance. *American journal of respiratory and critical care medicine*, 173(8):847–851, 2006.

[99] RC Weast. *CRC Handbook of Chemistry and Physics*. Elsevier Academic Press, 63rd edition, 1982.

[100] Ewald R Weibel. What makes a good lung. *Swiss Med Wkly*, 139(27-28):375–386, 2009.

[101] John Burnard West. *Pulmonary physiology and pathophysiology: an integrated, case-based approach*. Lippincott Williams & Wilkins, 2007.

[102] ER Wiebel. *Morphometry of the Human Lung*. Springer Berlin Heidelberg, 1963.

[103] Jim M Wild, Helen Marshall, Xiaoxun Xu, Graham Norquay, Steven R Parnell, Matthew Clemence, Paul D Griffiths, and Juan Parra-Robles. Simultaneous imaging of lung structure and function with triple-nuclear hybrid mr imaging. *Radiology*, 267(1):251–255, 2013.

[104] Mark Winter. Webelements periodic table. `http://www.webelements.com`. Accessed: 2015-06-08.

[105] Jason C Woods, Cliff K Choong, Dmitriy A Yablonskiy, John Bentley, Jonathan Wong, John A Pierce, Joel D Cooper, Peter T Macklem, Mark S Conradi, and James C Hogg. Hyperpolarized 3he diffusion mri and histology in pulmonary emphysema. *Magnetic resonance in medicine*, 56(6):1293–1300, 2006.

[106] Xiaojun Xu, Mathieu Boudreau, Alexei Ouriadov, and Giles E Santyr. Mapping of 3he apparent diffusion coefficient anisotropy at submillisecond diffusion times in an elastase-instilled rat model of emphysema. *Magnetic resonance in medicine*, 67(4):1146–1153, 2012.

[107] Dmitriy A Yablonskiy, Alexander L Sukstanskii, Jason C Leawoods, David S Gierada, G Larry Bretthorst, Stephen S Lefrak, Joel D Cooper, and Mark S Conradi. Quantitative in vivo assessment of lung microstructure at the alveolar level with hyperpolarized 3he diffusion mri. *Proceedings of the National Academy of Sciences*, 99(5):3111–3116, 2002.

[108] Dmitriy A Yablonskiy, Alexander L Sukstanskii, James D Quirk, Jason C Woods, and Mark S Conradi. Probing lung microstructure with hyperpolarized noble gas diffusion mri: theoretical models and experimental results. *Magnetic Resonance in Medicine*, 71(2):486–505, 2014.

[109] Dmitriy A Yablonskiy, Alexander L Sukstanskii, Jason C Woods, David S Gierada, James D Quirk, James C Hogg, Joel D Cooper, and

Mark S Conradi. Quantification of lung microstructure with hyperpolarized 3he diffusion mri. *Journal of Applied Physiology*, 107(4):1258–1265, 2009.